Characterization of urban aerosols pollution during the COVID-19 crisis by particle induced X-ray emission spectroscopy

Thesis for the Degree of Doctor of Philosophy (PhD)

Shafa Aljboor

Supervisor:

Dr. Zsófia Kertész

UNIVERSITY OF DEBRECEN
Doctoral Council of Natural Sciences and Information Technology
Doctoral School of Physics

Debrecen, 2024

Hereby I declare that I prepared this thesis within the Doctoral Council of Natural Sciences and Information Technology, Doctoral School of Physics, University of Debrecen in order to obtain a PhD Degree in Natural Sciences at Debrecen University.
The results published in the thesis are not reported in any other PhD theses.

Debrecen, 2024……. Shafa Aljboor
Candidate

Hereby I confirm that Shafa Aljboor candidate conducted her studies with my supervision within the Physical Methods in Interdisciplinary Researches Doctoral Program of the Doctoral School of Physics between 2018 and 2024. The independent studies and research work of the candidate significantly contributed to the results published in the thesis.
I also declare that the results published in the thesis are not reported in any other theses.
I support the acceptance of the thesis.

Debrecen, 2024……. Dr. Zsófia Kertész

Supervisor

Characterization of urban aerosols pollution during the COVID crisis by Particle Induced X-ray Emission spectroscopy

Dissertation submitted in partial fulfilment of the requirements for the **doctoral** (PhD) degree in physics

Written by Shafa Aljboor certified physicist

Prepared in the framework of the Doctoral School of Physics of the
University of Debrecen
Physical Methods in Interdisciplinary Researches programme

Dissertation advisor: Dr. Zsófia Kertész

The official opponents of the dissertation:

Dr. ....

Dr. ....

The evaluation committee:

Chairperson: Dr. ……. ……

Members: Dr. ……. ……

Dr. ……. …….

Dr. ……. …….

Dr. ……. …….

The date of the dissertation defense.....……

Acknowledgements

All praise and gratitude be given to Allah the Almighty for giving me such great strength, patience, courage, and ability to complete this thesis. Although any learning activity is personal work, it requires the help, support, and encouragement of others to be successful. Just as an eagle could not soar without the invisible strength of the wind, I could not have arrived at this place without all the invisible hands that provided me that strength. I would like to present my humble appreciation and gratefulness to all the people who made this journey possible. I am in debt to those who knowingly and unknowingly were so helpful and important in the difficult moments. Firstly, my deepest appreciation goes to Dr. Zsófia Kertész who has provided expertise, knowledge, support and coaching during my work.

Secondly, I would like to thank my family, especially my husband and my mother for supporting me spiritually throughout my life. Thanks to all my friends in Debrecen, who have always been with me during my stay in Hungary.

A big thank you to whom I forgot to mention!

Shafa Aljboor, 2023….

Contents

List of Abbreviations

AQGs	Air Quality Guidelines
ATOMKI	Institute for Nuclear Research (Hungarian Academy of Sciences)
BC	Black Carbon
BC_{bb}	Black carbon from Biomass Burning
BC_{ff}	Black carbon from Fossil Fuel combustion
CCN	Cloud Condensation Nuclei
DMS	Dimethyl Sulfide
EU	European Union
EPA	United States Environmental Protection Agency
EAD	Aerodynamic Diameter
HVEE	High Voltage Engineering Europa
IAEA	The International Atomic Energy Agency
IN	Ice Nuclei
IBA	Ion Beam Applications
LOD	The Limit Of Detection
MDL	Method Detection Limit
MABI	Multi-Wavelength Absorption Black Carbon Instrument
NAAQS	National Ambient Air Quality Standards
PC	Polycarbonate Filters
PM_{10}	Particulate Matter with diameters that are generally 10 micrometers and smaller.

$PM_{2.5}$	Particulate Matter with diameters that are generally 2.5 micrometers and smaller.
PIXE	Particle-Induced X-ray Emission or Proton-Induced X-ray Emission
ppm	Parts Per Million
PMF	Positive Matrix Factorization
PTFE	Poly Tetra Fluoro Ethylene membrane filters
PBAs	Primary Biogenic Aerosols
S/N	Signal / Noise ratio
SFU	Stacked Filter Unit
SRIM	The Stopping and Range of Ions in Matter Software
SDD	Silicon Drift Detectors
SOAs	Secondary Organic Aerosols
USEPA	United States Environmental Protection Agency
UTW	Ultra-Thin Window
VOCs	Volatile Organic Compounds
VdG	Van de Graff
WHO	World Health Organization

Introduction

Atmospheric aerosols have significant effects on many aspects of our life. They affect the Earth's climate as strong as greenhouse gases, and they influence the weather, as well. Aerosols also may reduce visibility, which in many places of the world results in haze. Aerosols have considerable impact on the biosphere, the natural and built environment, too.

Air pollution, especially particulate matter (PM) pollution causes the premature death of over 4 million people each year [1] .The importance and hazard of these particles originate from their tiny size, which means that they can penetrate deep into our lungs and pass into our bloodstream and could cause several health problems like lung cancer, heart disease, and stroke [2].

Therefore, characterization of aerosols pollution and identification of sources of particulate matter is an important issue for the societies, too.

COVID-19 pandemic caused by coronavirus (SARS-CoV-2) emerged at the end of 2019, and became a world pandemic in early 2020. COVID-19 pandemic has reached almost every country in the world. The outbreak of the pandemic forced the majority of governments to establish strict regulations in their countries in an effort to stop the virus's spread. To establish social distance, a nationwide lockdown was imposed in Hungary on March 12, 2020. Schools and institutions were closed, non-essential business and industrial activities were restricted, and leaving one's home was strictly prohibited. The restrictions were maintained until 4th May. Since then, different levels of restrictions have been in force depending on the actual evolution of the pandemic. Shutdowns around the world have given a precious window for researchers to study the changes of aerosol pollution under unique conditions.

We also took advantages from this opportunity to study urban particulate matter pollution during the COVID crisis in Debrecen, Hungary.

The objective of my work was to characterize urban aerosols pollution during the COVID crisis and to compare it with the data from the previous two years.

During my work I determined the concentration, elemental composition and sources of fine ($PM_{2.5}$) and coarse (PM_{10}-$PM_{2.5}$) particulate matter pollution in Debrecen, between March 2018 and Feb 2022. I studied the changes induced by the different levels of COVID shutdowns. The elemental concentrations of the aerosols samples were determined by accelerator-based Particle Induced X-ray Emission (PIXE) method. I took part in the

installation and characterization of the new in-air millibeam PIXE setup at the Tandetron Accelerator of the Institute for Nuclear Research (ATOMKI).

The first part of my thesis provides an overview of the literature background of the research (Chapters 1). The applied sampling, analytical and statistical methods are presented in Chapter 2. The newly developed PIXE measurement setup and its analytical performance presented in the first part of the result and discussion (Chapter 3.1). In the second part of Chapter 3, results achieved on the characterization of urban aerosol pollution in Debrecen before and during the COVID pandemic are described. The summary and references are the last parts of the thesis.

1 Atmospheric aerosols - literature review

Atmospheric aerosols (known as particulate matter, PM), which are either solid or liquid particles (such as pollen spores, fractal soot agglomerates, small salt crystals, etc.) floating in the ambient air that are generally stable (Figure **1.1**). These arise from a number of anthropogenic sources, including industrial activity, power generation, road traffic, man-made biomass burning, agriculture, and homes, as well as from natural sources such as sea salt, soil dust, vegetation, volcanoes, and natural biomass burning. They can be discharged directly into the atmosphere (primary particles) or formed through gas-to-particle conversion in presence of precursor gases (secondary particles). As a result, atmospheric aerosols are complicated mixtures of many chemical species. Their presence is sometimes easily visible by the human eye, such as haze in industrial areas and locations where biomass is burned extensively. On the other hand, there are particles with such small sizes that can't be seen through optical microscopes [3]. Aerosols particles in the atmosphere can have diameters ranging from 1 nanometer (nm) to 100 micrometers (μm). The majority of their mass is in the (0.1 to 10) μm size range.

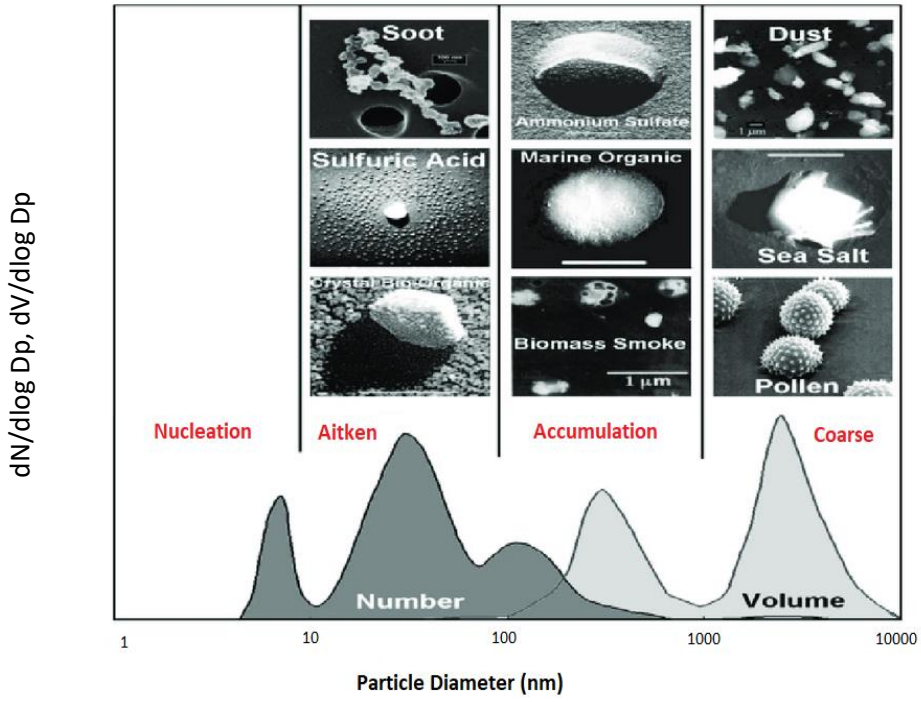

Figure 1.1. Schematic figure of aerosol size distribution by number and volume, showing the various size classes ('modes') as well as example pictures of some archetypical aerosol particles. [4]

1.1. Characterization of Atmospheric Aerosols

1.1.1. Size Distributions

The most significant determinant of particle properties is size, which can be between a few nm and tens of μm in diameter [5] [6]. Particle size has effects on life time of particulate matter, particle creation, transportation, physical and chemical characteristics, transformation, and removal from the environment [7]. Particle size also has a significant impact on the deposition within the human respiratory system.

The aerosol size distribution can be described mathematically in a number of different ways, but it is commonly expressed in three forms:

Frequency distribution

$$\frac{1}{N}\frac{dN}{dr} = f(r).\int_0^{\infty} f(r)dr = 1 \tag{1.1}$$

Number distribution

$$\frac{dN}{dr} = N.f(r).\int_0^{r}\frac{dN}{dr}dr = N \tag{1.2}$$

Logarithm scales

$$\int_0^{r}\frac{dN}{d\log r}\,d\log r = \int_0^{r}\frac{dN}{dr}\,dr = N \tag{1.3}$$

dN being the number of particles in the size range dr and N the total number, more details in [8].

Particles are mostly classified in four major modes according to their size, they are "**Nucleation mode**" (particles with diameter less than 0.01 μm), "**Aitken mode**" (particles diameter range

between 0.01 and 0.1 μm), "**Accumulation mode**" (0.1 – 2.5 μm), and **coarse particle**-mode (particles with diameter more than 2.5 μm) [9].

Nucleation mode is formed by the nucleation of super-saturated vapors. The consecutive primary and secondary particles are found close to their emission sources. Examples of these primary pollutants are carbonaceous compounds and sulfuric acid (H_2SO_4) [10]. The **Aitken mode** originates from condensation on and self-coagulation of nucleation mode particles, as well as from primary emissions during high-temperature combustion. Third stage of aerosols formations is known as accumulation, resulting particles in the **accumulation mode** (0.1-2.5 μm). In this stage particles are formed through coagulation and condensation. Accumulation-mode particles can stay in the atmosphere for a long time (about one to two weeks) before being eliminated by wet deposition. **The nucleation and Aitken modes** contain the largest number of particles, but not much of the total mass burden.

The particles in the **coarse mode** have a different forming process than the other modes, as described earlier. Mainly formed by mechanical processes including surface abrasion, crushing, and grinding, such as the earth's surface being eroded by wind. Examples of coarse mode aerosols are coal, cement, agricultural dust, soil dust and sea salt particles, or particles from volcanic eruptions. Bioaerosols, such as spores, pollen, bacteria, and small fragments of plants and animals, are also in this size range. The coarse mode particles usually settle out within a few hours or days from the atmosphere depending on their size, the prevailing meteorological conditions, and altitude [11].

Although the coarse mode particles quickly settle out of the air due to their mass and precipitation processes [12], together with the accumulation mode, they make up the majority of the mass of the atmospheric aerosols. Even though primary particles predominate in the coarse mode, secondary particles of crustal or marine origin may also be present [13] due to the chemical reaction of primary particles with gases.

Summary of aerosols formation and size distribution is shown on Figure **1.2**.

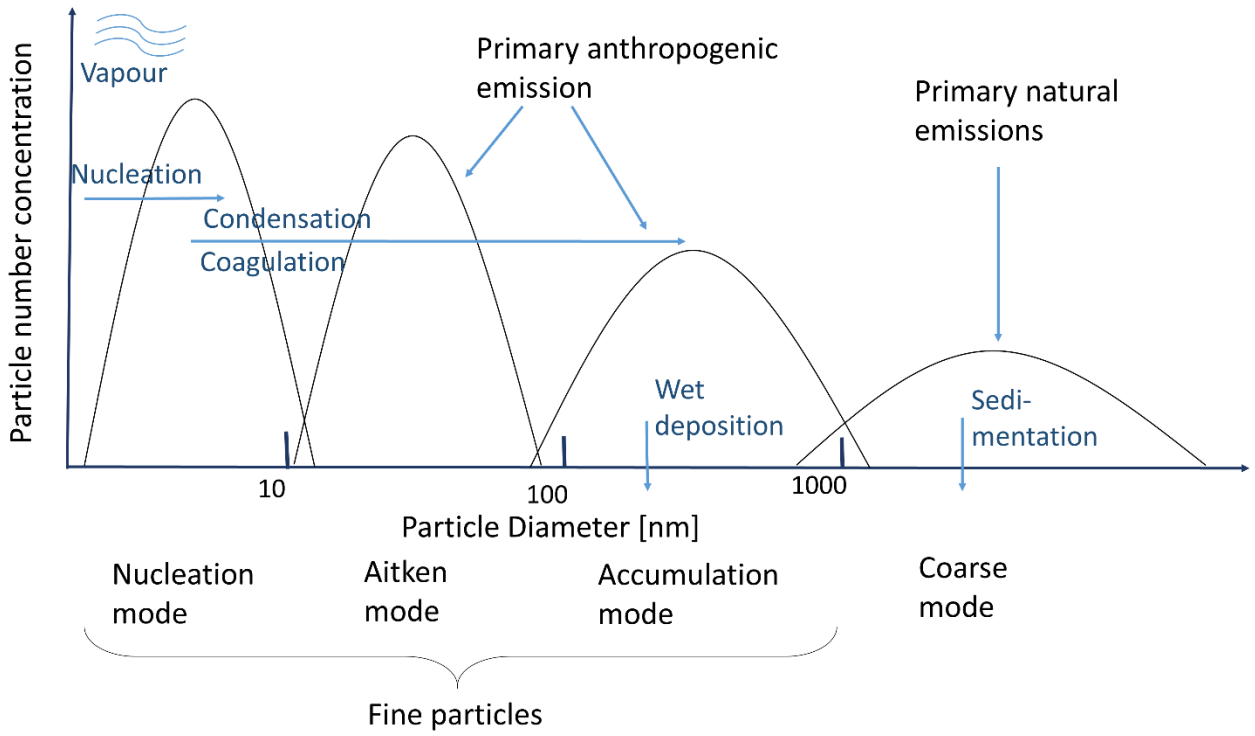

Figure 1.2. Idealized schematic figure of atmospheric aerosols particle number size distribution, including the aerosols modes with typical formation and removal processes. Adapted from [14].

1.1.2. Formation process

Aerosol particles in the atmosphere can be categorized into two categories based on their primary mechanisms of formation. These categories are primary and secondary particles**.** According to the mass size distribution, they can be sorted into two main groups: **coarse** (PM_{10}-$PM_{2.5}$) and **fine** ($PM_{2.5}$) size fraction. Primary particles are predominantly found in the coarse size fraction while secondary particles compose mostly the fine size fraction [15].

1.1.2.1. Primary particles

Primary particulate matter is emitted immediately into the atmosphere via mechanical processes. Their typical source is volcanic emissions, sea-spray, suspension of bulk material (soil, road dust, mineral dust, biological material) driven by the wind. Typically, they are particles with diameter larger than 1 µm. For such emission processes, the particle number concentration rises non-linearly

with increasing wind speed [16]. Primary particles do not coagulate with one another due to their low concentrations and large sizes, but they can mix with other species through mass exchange with the gas phase. Soot particles, which are generated during combustion, are a special and significant sort of primary particles. Initially, they arise with a size of (5-20) nm diameter at high concentrations during the combustion process. They coagulate quickly, forming fractal-like aggregates that, due to capillary forces of condensing vapors, compress to more compact structures of many tens of nanometers.

Primary particles include the following:

Soil dust: The most common source of coarse aerosols particles is soil dust which is mainly produced by erosion in arid and semi-arid areas. The strength and location of emissions are influenced by natural or human-caused climate changes that alter wind velocity and precipitation. Soil PMs play a significant role in chemical processes in the troposphere. Soil particles interact with sulfuric acid [17] and nitric acid [18] through heterogeneous chemical reactions, influencing particle acidity and gas phase composition.

The size distribution is mostly bimodal, with maxima observed at (1-10) μm and 50μm, respectively. More than 90% of the bulk has a diameter bigger than 1 μm. Large particles with a diameter of more than 30 μm settle near the source regions, but smaller particles have a lifespan of several days to weeks and can travel thousands of kilometers. The crustal fingerprints of silicon, aluminum, iron, sodium, potassium, calcium, and magnesium distinguish soil dust from other sources. The actual makeup may differ from one location to another. However, silicon, aluminum, iron and calcium are typically used as key indicators of soil-derived materials.

Sea salt: is created by the bursting of air bubbles at the ocean's surface. Because sea salt aerosols are mostly sodium chloride, they are very hygroscopic and change size rapidly in response to changes in ambient relative humidity. The fresh and aged sea-salt particles have a significant impact on world climate. When sea salt reacts with acidic gases, sodium sulfate and sodium nitrate are formed, and chloride is released into the gas phase [19].

Sea salt is the most common aerosols mass component in remote sea surface air, and it may even be found in substantial quantities over continents. The status of the sea surface, which is a result of climatic variables, particularly wind speed, has a substantial influence on sea salt concentrations in coastal regions. The so-called "chloride depletion" in urban particulates occurs when chloride is

lost in sea salt particles as a result of interactions between sea salt particles and acidic components such as sulfuric and nitric acids. This phenomenon has been observed in many studies. [20-22]

Biogenic particles: Biogenic aerosols are found throughout the Earth's atmosphere, influencing atmospheric chemistry and physics, as well as the biosphere, climate, and public health. Primary and secondary sources of biogenic aerosols exist. Primary biogenic aerosols PBAs are directly released into the atmosphere by the biosphere. Pollens, bacteria, spores, virus, algae, protozoa, fungus, leaf fragments, and insect pieces are among the items found in them [23]. PBA particles range in size from millimeters to tens of nanometers. The secondary sources are particles generated through gas-to-particle conversion of gaseous organic materials emitted from the biosphere. The size of these particles is frequently sub-micrometer.

Forests are a major natural source of aerosols across the world [24]. Biogenic volatile organic compounds (VOCs) account for more than 90% of all VOCs released into the atmosphere. Marine-derived biogenic aerosols also contribute to global biogenic aerosols loading. Biogenic organic matter concentrated in the sea surface layer was reported to be transmitted to the atmosphere through a bubble-bursting mechanism [25].

Combustion particles: Combustion processes result in generation of large number of particles and gaseous products. Combustion sources can be classified into stationary (industrial plants, power plants, households etc.) and mobile sources (mainly motor vehicles). Carbonaceous and fly ash particles are the most common primary particles released directly from combustion operations.

The size distribution of combustion PMs is multimodal. Gas-to-particle transformations yield the finest aerosol particles, which are known as nuclei or nanoparticles. The inorganic substance in the fuel produces the larger super micron particles. The composition of the fuels, the combustion conditions, and the efficacy of cleaning systems all influence emissions [26]. Diesel exhaust generally contains particles with a diameter of (5 to 50) nm [5] [27].

This mode contains volatile organic and sulfur chemicals formed during exhaust dilution and cooling, as well as solid carbon and metal components.

Fly ash mainly comes from coal burning. It is made up of inorganic, non-combustible materials in the coal that has been fused into a glassy, amorphous form during burning. It's largely made up of oxygen, silicon, aluminum, calcium, iron, carbon, potassium, magnesium, sulfur, and a few other minor and trace elements. Secondary aerosols precursors (SO_2, NO_x, and hydrocarbons) are also produced by combustion processes (the results are sulfate, nitrate, and organic aerosols).

Depending on the partitioning of sulfur between SO_2 and SO_3 (sulfur trioxide), as well as the temperature and humidity, coal burning can also create acid aerosols such as H_2SO_4.

1.1.2.2. Secondary particles

Formed mainly from gas-to-particle transformation, whereby gases such as Sulphur dioxide (SO_2), nitric oxide (NO) and nitrogen dioxide (NO_2), and VOCs are oxidized and condensed to the liquid or solid phase. This occurs when the concentration of the compound in the gas phase exceeds its equilibrium vapor pressure above the aerosols surface. These PMs includes the following:

Sulfate (SO_4^{2-}): Sulfate in the ambient air is mostly produced by the oxidation of Sulfur-containing precursors such as SO_2, hydrogen sulfide H_2S, carbon disulfide CS_2, carbonyl sulfide COS and dimethyl sulfide DMS C_2H_6S, with SO_2 accounting for the majority of the sulfate [28]. SO_2 can be oxidized to H_2SO_4 through gaseous, aqueous, or multiphase reactions with OH^-, H_2O_2, and O_3, then condensation or nucleation of H_2SO_4 onto pre-existing particles and into new particles with partial or complete neutralization by NH_3.

Sulfate is a well-known example of a long-distance transported component with identical concentrations across wide distances [29]. In the atmosphere, sulfate is frequently found in the fine size fraction (<1 μm) [30]. Fine size fraction sulfate has an atmospheric life of around 5 days [31], during which time it reacts with ambient NH_3. It's partly neutralized as NH_4HSO_4, then neutralized again as $(NH_4)_2SO_4$. In coarse size fraction (>1 μm), when it is present in soil and/or sea-salt particles, a tiny proportion of sulfate can be observed [32].

Nitrate (NO_3^-): is generated by the homogeneous gas-phase oxidation of nitrogen oxides to gaseous nitric acid, which is then reacted with gaseous ammonia to form extremely volatile NH_4NO_3 [33].The most important precursor for nitrate aerosols is nitrogen oxide emissions from transportation. Nitrate, like sulfate, is generally disseminated in a fine size fraction called ammonium nitrate. However, in sites where ammonium nitrate production is inhibited, such as areas with high SO_2 to NH_3 emission ratios across land and sea, nitrate is found mostly in coarse size fraction (>1 μm), in combination with soil and/or sea-salt particles [34].

Ammonium (NH_4^+): As a result of atmospheric neutralization, ammonium is frequently accompanied by sulfate and nitrate. Sulfate and nitrate are competitors for ammonia NH_3, striving to generate equivalent salts. Only when virtually all of the sulfate has been consumed does ammonium nitrate appear [35].Ammonium sulfate is the most stable of the inorganic secondary

aerosols. Ammonia emissions vary seasonally based on farming practices and climate conditions. Agriculture accounts for (80-95) percent of ammonium in Europe [36]. It sits in the fine size fraction-with the accompanying pairs when paired with sulfate and nitrate. It could also exist in coarse size fraction, but the process isn't the same as it is in fine size fraction. According to [37], coarse aerosol particles ammonium is the result of interactions between ammonia gas and pre-existing sulfuric or nitric acid on coarse aerosol particles.

Secondary organic aerosols SOAs: SOAs are generated in the ambient atmosphere by the oxidation of volatile organic compounds and the subsequent partitioning of certain oxidation products into the aerosols phase. Gas-phase oxidation, in which VOCs are oxidized by species such as OH^-, O_3, and NO_3^- [36], and/or aqueous-phase oxidation, in which SOAs are generated in cloud and fog droplets, are two possible mechanisms for SOAs generation [38].

1.1.3. Atmospheric Trace Metals

More than 90 elements are found in the crust of the earth, of which only nine (Al, Fe, Ca, Mg, O, Si, Na, K, and Ti) account for nearly 99% of the total weight. The remaining 81 elements, which account for less than 1% of the total weight, are referred to as "trace elements." Despite their limited availability in nature, these elements play an important role in toxicological and environmental effects. V, Cu, and Pt are trace metals that can stimulate the formation of reactive oxygen species, which have been linked to direct molecular damage [39]. Secondary aerosols production can also be catalyzed by trace metals. Trace metals are released into the atmosphere during the burning of fossil fuels and wood, as well as high-temperature industrial activities and trash incineration. Natural emissions originate from a variety of processes such as volcanic activity, erosion, and surface winds, as well as forest fires and the sea [40].

Combustion of fossil fuels is the main source of Be, Co, Hg, Mo, Ni, Sb, Se, Sn, and V, and has a significant contribution of As, Cr, Cu, Mn, and Zn, whereas industrial metallurgical operations create the most As, Cd, Cu, Ni, and Zn emissions [41]. The type of emissions to the atmosphere controls the concentration and size distributions of trace elements, which are found in practically all aerosols size fractions [42]. Trace metals from combustion and industrial sources are found predominantly in the fine and ultrafine fractions, whereas re-suspended dust and mechanical wear appears mainly in the coarse mode [39].

Many industrial and urban locations have elevated trace element concentrations [43]. When it comes to identifying natural and anthropogenic sources, the enrichment factor (EF), or the twofold ratio between a specific trace element and a typical crustal element (such as Ti or Al) between the aerosols and the earth crust, is frequently relevant. Anthropogenic sources may be indicated by elements having EF values considerably higher than unity. For several common fuel types, certain elements are utilized as tracers. V and Ni are frequently attributed to residual oil combustion. As and Se are fingerprints of coal combustion [44].

1.1.4 Carbonaceous aerosols

Aerosols that include a carbon atom are known as carbonaceous aerosols. Organic carbon aerosols (OC) are the portion of carbonaceous aerosols that include organic carbon compounds, whereas black carbon (BC) is the absorbing component of aerosols. Carbonaceous aerosols can come from either primary or secondary sources. Primary sources are released as particles, whereas secondary sources are emitted as gases. Both types of sources undergo photochemical transformations in the atmosphere before creating low-volatility compounds that can condense to create an aerosols.

In the majority of studies which published carbonaceous aerosols concentrations, aerosol samples were collected on filters and the analysis applied thermal volatilization and combustion techniques. Total carbon, elemental carbon, and organic carbon mass concentrations are determined using these methods of analysis.

1.2. The importance of studying aerosol particles as an atmospheric pollution

The study of atmospheric aerosol particle pollutants has risen over the years due to the understanding of its negative health impacts [45], and because it became clear that aerosols in the atmosphere have a significant influence in climate change [46]. Atmospheric aerosol particles also affect various atmospheric processes, such as cloud formation, precipitation and hence the global hydrological cycle, and solar irradiance, and have a crucial impact in cloud, rain, and fog acidification [29].

Aerosols have an essential role in atmospheric chemistry, contribute to contamination and corrosion of buildings and structures, and have negative effects on vegetation and ecosystems [47]. The physical and chemical characteristics of the aerosols, such as aerosols size, concentration, and chemical composition, are responsible for the majority of the impacts.

1.2.1 Human Health Effect

Several epidemiological studies published in the last decade have found a positive and statistically significant link between particulate matter pollution and cardiopulmonary diseases, mortality, and morbidity [48]. Through respiration, airborne particles (<10 μm), which are filled with potentially harmful trace metals, may accumulate in the human body, causing chronic and acute health concerns [49] [50]. The health effects of inhaled particles are dependent on their size distribution, concentration, and chemical structure, as well as the place in the respiratory system where they deposit [51]. Despite the fact that coarse PM has been shown to have a high potential for inducing inflammatory mediators, fine particles may still be responsible for the majority of PM_{10} effects due to their large number or surface area [52], as well as the fact that they contain more toxic elements and species. Trace elements in fine particles, such as lead, zinc, copper, cadmium, and others, are of major concern due to their toxicity. Researchers believe that trace metals may stimulate the development of oxidants in the lungs, leading to tissue damage. Concentration of trace elements have increased significantly in the atmosphere as a result of traffic emissions, combustion processes, and industrial operations such as metal refining (Figure **1.3**) [53].

Because dust particles are made up of minerals like quartz, feldspar, and palygorskite, and they can adsorb harmful chemical species, mineral dust episodes can cause major respiratory issues in humans [54]. Furthermore, significant dosages or long-term exposure to volcanic ash can induce lung fibrosis [55], whereas occupational exposure to quartz and asbestos has been linked to chronic inflammation, fibrosis, and cancer [56].

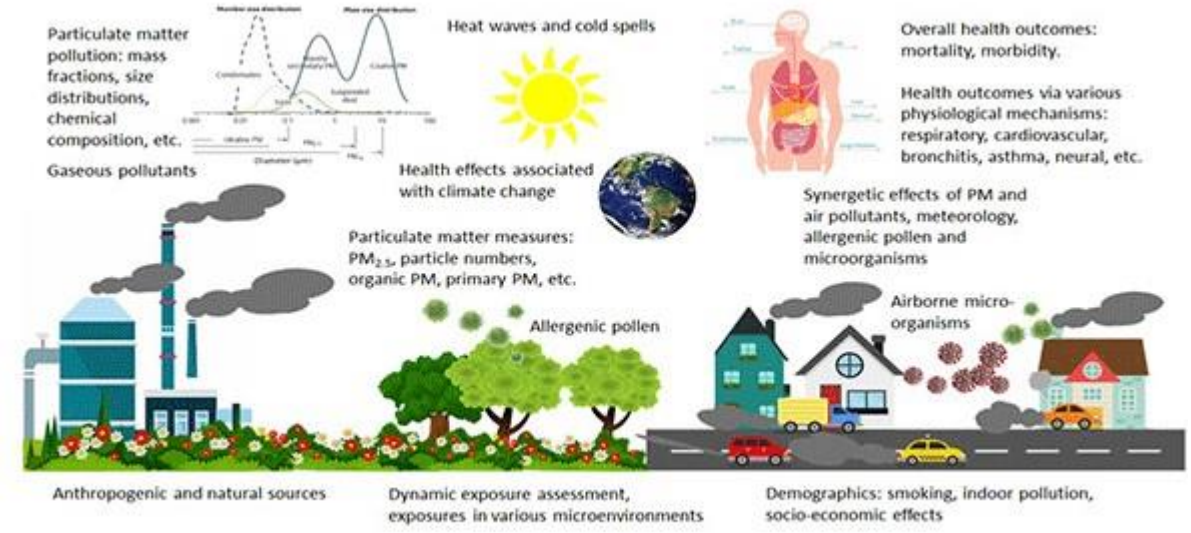

Figure 1.3 A schematic diagram, which illustrates some of the main factors in the evaluation of the health exposure and health impacts of particulate matter. [57].

1.2.2 Climate Effect

The influence of atmospheric aerosol particles on the Earth's climate system is one of the key concerns around the world. Climate change can be caused by processes that disrupt the Earth's overall radiation balance [9]. Aerosol particles in the atmosphere have two effects on the Earth's radiation budget. First, direct radiative forcing by scattered and absorbed incoming solar radiation (short-wave radiation) and outgoing terrestrial infrared radiation (long-wave radiation). Second, indirect radiative forcing affects the characteristics and formation processes of clouds (ability to serve as cloud condensation nuclei (CCN), and ice nuclei (IN)) [58].

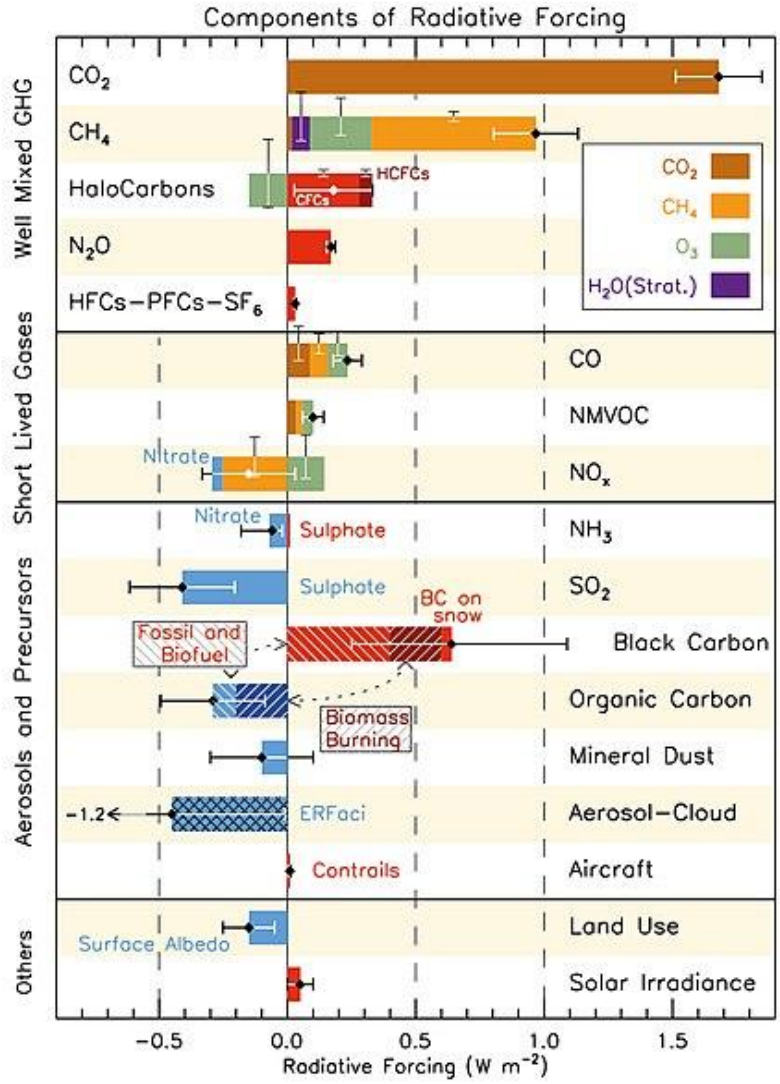

Figure 1. 4 Summary of the principal components of the radiative forcing of climate between 1750 and 2011 [59].

Aerosols can influence the concentration and size distribution of cloud droplets in this way. As a result, they can modify cloud radiative characteristics, cloud lifespan, rain cloud type, and allocation, interfering with the hydrological cycle [60]. In recent decades, both direct and indirect radiative forcing have been acknowledged as critical to interpreting observed climate change. Figure **1.4** depicts the contributions to radiative forcing from some of the components impacted by human activity.

1.2.2.1. Direct radiative forcing

The aerosols' direct radiative forcing is predicted to be –0.50 ± 0.40 W m^{-2}. [46]. Atmospheric aerosols' radiative effects are determined by their chemical composition and particle size distribution. According to the majority of early studies, sulfate aerosols are effective in scattering incoming short-wave radiation back to space. However, due to their small size, they have minimal impact on outgoing long-wave radiation. The net direct impact of these tiny particles is cooling since they reduce the quantity of incoming solar radiation. Organic aerosols, which are often found in the fine particle size range, also decrease the quantity of solar energy absorbed. Organic aerosols characteristics alter as a result of chemical interactions with gaseous oxidants (aging). An organic coating on an absorbing core (e.g. soot) enhances the particle's absorption, whereas an organic coating on a hygroscopic core (e.g. sulfate) reduces the particle's rate of water uptake. In many places, the weakening of the sulfate aerosol's radiative forcing related to reduced emissions would be partially balanced by increases in the nitrate aerosol's radiative forcing, while the anticipated value for organic carbon has stayed relatively constant. Black (elemental) carbon, on the other hand, is a good absorber of solar energy and hence generates positive forcing (warming) [46]. Mineral dust may change the Earth's radiation budget by warming or cooling (dust particles re-emit infrared radiation back toward the Earth's surface and reflect sunlight back into space) depending on its concentration, vertical distribution in the atmosphere, particle size and mineralogy, as well as the albedo and temperature of the underlying surface [61].

1.2.2.2 Indirect radiative forcing

Aerosols in the atmosphere have an additional indirect effect on the radiation budget because they serve as cloud condensation nuclei CCN. Changes in CCN concentration and size, both anthropogenic and natural, have been postulated to affect cloud characteristics [60]. Increases in the quantity of CCN with the same cloud water content result in smaller cloud droplets, increasing the solar reflectivity of the cloud (first indirect effect or cloud albedo effect) and causing a negative radiative forcing. The smaller droplet radius may reduce the cloud's capacity to precipitate, resulting in a longer cloud lifespan and further negative forcing. (Second indirect effect or cloud lifetime effect). Because these cloud processes impact the rates at which particles are removed, the aerosol load may be changed as well. Solar radiation absorption (for example, by soot particles) has a cooling impact at the surface (negative forcing), but a heating effect in the troposphere, which

might trigger cloud evaporation (positive forcing). Although the cooling effect is likely to be greater, heating the air has an indirect effect on the vertical distribution of temperature (semi-direct effect) and hence has an impact on the global hydrological cycle [62]. Sulfate aerosols appear to be a primary source of CCN. Other aerosols types, including biomass burning and nitrate, mineral dust particles, have been postulated to have a role in indirect forcing in addition to sulfate [63].

1.3 PM regulations

Outdoor air pollution is a cross-border issue that has direct detrimental consequences for the environment, climate, and health, particularly for those who live in cities. It also has indirect but palpable negative consequences for businesses and communities as a whole. Despite the fact that air quality has improved in the previous decade, [64] air pollution is still a serious problem for a number of areas across the world.

Reference criteria issued by the World Health Organization (WHO), the European Union (EU), and the United States Environmental Protection Agency (USEPA) are the most often used ones for ambient particulate matter concentrations. These limit values were set by considering epidemiological, clinical, and toxicological evidences. First, a concentration with the least observed adverse effects were determined implicitly accepting the idea that there is a lower threshold below which no adverse effect on human health can be detected. Then it was adjusted by an arbitrary safety factor to take account of the uncertainties of extrapolation from animals to humans and from small groups of humans to larger populations.

1.3.1. WHO guidelines

The first version of the WHO air quality guidelines (AQGs) for Europe was published in 1987 and included only sulfur dioxide and black smoke. In the 1990s, a number of studies were published that permitted direct evaluation of the health impact of inhalable particles [65, 66]. Furthermore, studies that allowed the evaluation of the health consequences of only PM_{10} exposure alone were available, either because information on exposure to other pollutants was limited or appropriate adjustment was not achievable.

The WHO's European Centre for Environment and Health completed its evaluation of health data in 2000, and the European AQGs were published [67]. The WHO established precise limits for all

pollutants except PM in these guidelines; the apparent lack of a threshold for PM impacts prompted the WHO to propose a concentration-response curve for PM. In its PM chapter, the WHO stated ‘‘…The available information does not allow a judgment to be made of concentrations below which no effects would be expected. Effects on mortality, respiratory and cardiovascular hospital admissions as well as other health variables have been observed at levels well below 100 μg/m³, expressed as a daily average PM_{10} concentration. For this reason, no guideline value for short-term average concentrations is recommended either. Risk managers are referred to the risk estimates provided in the tables for guidance in decision-making regarding standards to be set for particulate matter…” In 2006, the WHO released a new version of the AQGs [68]. The annual mean PM_{10} and $PM_{2.5}$ concentrations should be (20 and 10) μg/m³, respectively; the 24-hour PM_{10} and $PM_{2.5}$ concentrations should be (50 and 25) μg/m³, respectively.

In 2021 the WHO updated its recommendations. The ambitious new WHO AQGs for air quality (2021) reflect the significant negative effects that air pollution has on global health. They suggest aiming for yearly mean $PM_{2.5}$ concentrations of no more than 5 μg/m³, annual mean NO_2 concentrations of no more than 10 μg/m³, and peak season mean 8-hour ozone concentrations of no more than 60 μg /m³. By comparison, the 2005 WHO guidelines for $PM_{2.5}$ and NO^2 were 10 μg/m³ and 40 μg/m³, respectively, with no guidelines recommended for long-term ozone concentrations [69].

1.3.2. EU policy on air quality – legal framework

Because of the substantial cross-border feature of air pollution, improving air quality has been on the EU agenda for decades. The 2013 clean air program for Europe is currently the most important EU strategy document with a special focus on air quality [70]. Its major goal is to reduce the number of premature deaths due by exposure to ground-level ozone and fine particulate matter ($PM_{2.5}$) by half by 2030 compared to 2005 levels. Recently, the European Green Deal called for the development of a zero-pollution action plan, which is likely to include improved air quality across the EU as one of its main goals.

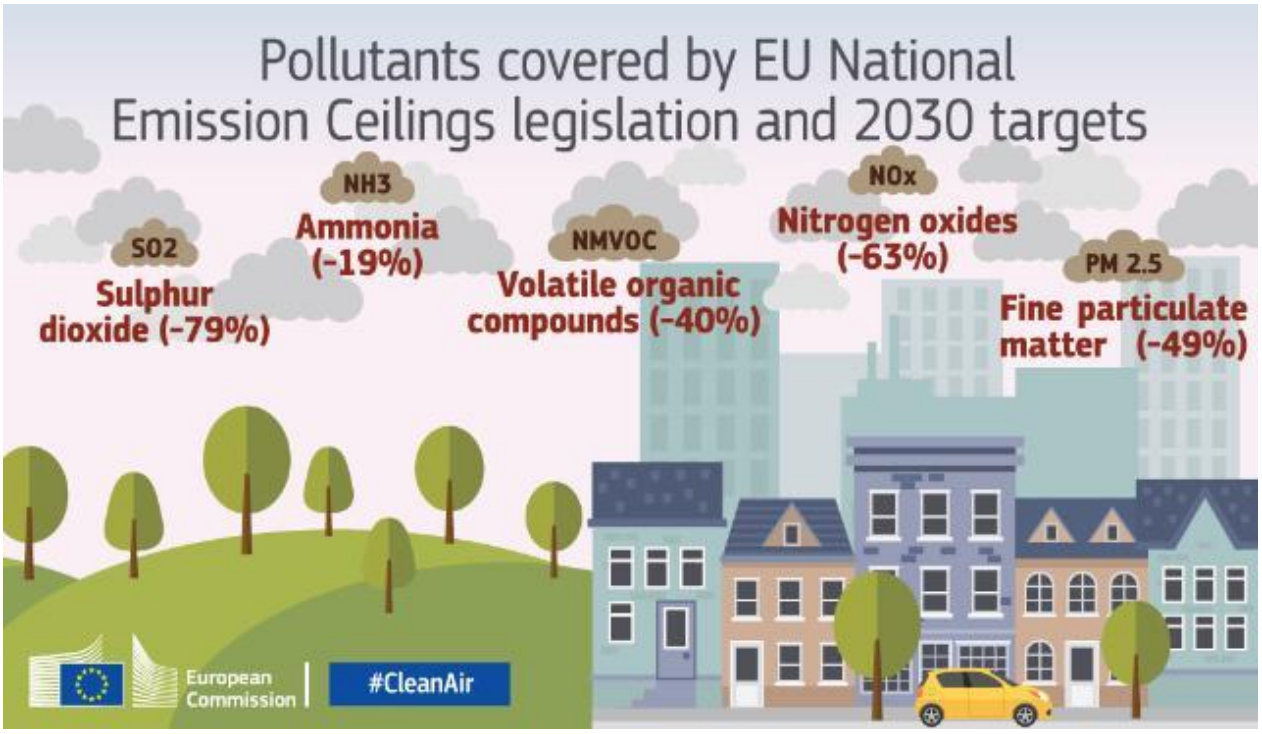

Figure 1.5 Pollutants covered by EU National Emission Ceiling legislation and 2030 targets [71].

The EU and its Member States employ legal regulation as an important policy tool to achieve the aforementioned objectives at the operational level, and particular action is performed within the framework of three policy pillars.

The first pillar consists of the two Ambient Air Quality Directives [72], which establish standards for a variety of air pollutants, harmonised criteria for air pollution monitoring and assessment across Member States, and an obligation to take measures to avoid, prevent, or reduce pollution.

The second pillar relies on the National Emissions Control Directive [73] which established national emission reduction commitments for major pollutants such as SO_2, NO_x, VOCs, NH_3, and $PM_{2.5}$ (see Figure **1.5**). It transposes the EU's commitments under the amended Gothenburg Protocol into EU legislation [74]. The Protocol was originally signed in 1999 and amended in 2012. Among others, the revised protocol introduced national emission reduction commitments to be achieved by 2020.

The third pillar contains several EU legislative acts that regulate air pollution from specific sources in sectors such as industry [75], the 2015 Medium Combustion Plants Directive [76], the

2009 Eco-design Directive [77], and transportation (the environmental performance aspects of EU type-approval legislation, etc.). Table **1.1** shows conclusion of the EU standards for a number of pollutants present in the air.

Table1.1. EU standards for a number of pollutants present in the air. Source: European Commission

pollutant	Concentration	Averaging period
$PM_{2.5}$	25µg/m^3	1year
PM_{10}	50µg/m^3	24 hours
	40 µg/m^3	1year
SO_2	350 µg/m^3	1 hour
	125 µg/m^3	24 hours
NO_2	200 µg/m^3	1 hour
	40 µg/m^3	1 year
Pb	0.5 µg/m^3	1 year
CO	10 µg/m^3	Maximum daily 8 hour mean
O_3	120 µg/m^3	Maximum daily 8 hour mean

The Hungarian legislation on air pollution is fully in line with the EU requirements, the European Air Quality Directive was transposed into national law in 2011, and therefore the EU AQ standards are in force.

Hungary's air quality is considered by the World Health Organization as being just moderately unsafe. The most recent data show that the country's annual mean $PM_{2.5}$ concentration is 16 µg/m^3, well below the EU guideline of 25 µg/m^3 but above the suggested maximum of 5 µg/m^3.

1.3.3. USA standards

The first National Ambient Air Quality Standards (NAAQS) were established in 1970 [78]. This legislation empowers the newly formed United States Environmental Protection Agency (EPA) to study the evidence of air pollution on public health and establish NAAQS that "protect the public health with an adequate margin of safety". The EPA issued the first NAAQS for PM in 1971, using total suspended particles TSP as the criterion. The EPA set a 24-hour average standard of 260 $\mu g/m^3$, with one yearly exceedance allowed, and a 75 $\mu g/m^3$ annual average standard.

In 1987, EPA issued the first PM_{10} rules, setting the 24-hour average standard at 150 $\mu g/m^3$ with one yearly exceedance permitted, and the annual average standard at 50 $\mu g/m^3$ [79]. After a contentious review the EPA established a new set of NAAQS for fine particles, measured as $PM_{2.5}$ in July 1997. These values were: 15 $\mu g/m^3$ a year-average, and 65 $\mu g/m^3$ a 24-hour average with 7 exceedances per year [80].

The EPA updated the 1997 criteria in September 2006 [81].The updated 2006 regulations cover two types of particle pollution: fine particles ($PM_{2.5}$) with a diameter of 2.5 μm or less, and inhalable coarse particles (PM_{10}) with a diameter of less than 10 μm. The 24-hour fine particle limit was tightened from (65 to 35) $\mu g/m^3$ in 2006, but the yearly fine particle standard remained at 15 $\mu g/m^3$. The existing 24-hour PM_{10} threshold of 150 $\mu g/m^3$ has been retained by the EPA.

2 Methods

2.1 Particle Induced X-ray Emission PIXE

In 1895, Roentgen first invented X-rays during his measurement with cathode rays [82]. In 1901, he was awarded the first Nobel Prize for his great discovery. X-rays are a kind of electromagnetic radiation having an extremely small wavelength. X-rays were widely used in the early stages of medical science, but their application is now becoming very broad. The characteristics of X-ray creation have attracted the interest of atomic physicists. In 1912, Chadwick [83] used heavy ions to study X-ray emission from radioactive sources for the first time (alpha-particles). Chadwick discovered low-intensity X-ray emission, which was unsuitable for analytical applications. Until the invention of accelerators for nuclear physics research, this procedure was not very beneficial.

In 1950, Castaing discovered X-ray emission spectrometry at the University of Paris [84], and it was a milestone in nuclear physics research. He demonstrated that the X-rays generated in the specimen in an electron microscope can be used for multi-element analysis.

Before the development of accelerators, electron beams with an energy of several keV were mostly utilized to generate X-rays. Though the X-ray production cross-sections for proton and helium ions with MeV energy are similar to those for electron beams with several keV energies, the background contribution from proton bremsstrahlung is significantly lower for heavy ions than for electrons. Since the X-ray production cross-section as a function of particle energy and atomic number was known, scientists became interested in the possibility of using heavy charged particles for analytical purposes in the 1960s. During the 1960s, certain attempts were made to use proton generated X-ray emission for elemental analysis [85] attempted to use low-energy protons to assess the thickness of thin coatings. The development of solid-state surface barrier detectors for charged particles made significant progress in nuclear physics after that.

Johansson established that Particle Induced X-ray Emission (PIXE) is a reasonably high sensitivity, multi elemental, and non-destructive analysis technique using MeV proton beams and high resolution Si(Li) detectors at the Lund Institute of Technology in 1970 [86]. They've shown that their technology is capable of analyzing trace components with good sensitivity. Although for trace element analysis, a variety of analytical methods have been utilized, the sample preparation was

often difficult and took a long time in those cases. Because the sample preparation processes are typically easy and it takes a short measurement time, PIXE and complementary IBA techniques are one of the most effective techniques for material analysis.

With the development of energy dispersive detector this powerful technology can readily analyze numerous elements in the parts per million (ppm) range with atomic numbers as low as 6. The PIXE analysis technique is divided into two parts. At first, the energies of the characteristic peaks in the X-ray emission spectrum are used to identify components in the target. Second, the intensity of a given element's characteristic X-ray peak in the emission spectra is used to calculate the quantity of that element in the target.

2.1.1 The Basic Principle of PIXE

The target atoms can be excited using a powerful incoming ion beam of protons or alpha particles to create X-rays, as shown in Figure **2.1**.

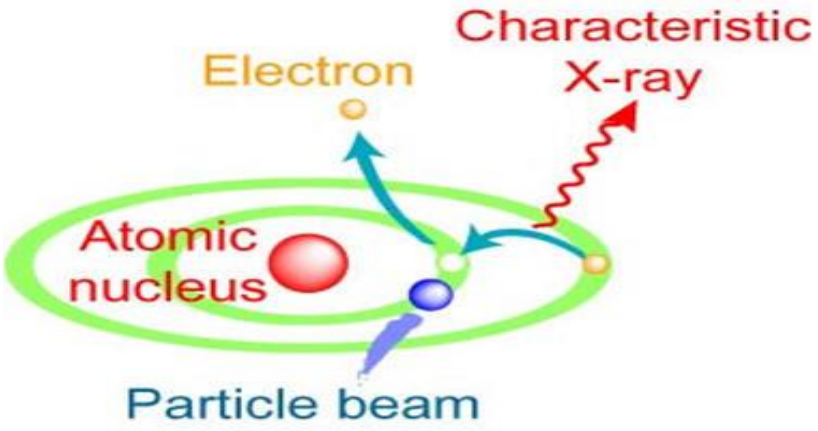

Figure 2.1 Basic principle of PIXE. [87]

When high-energy protons or alpha particles collide with target atoms, electrons are ejected from the atom's innermost shell. As a result, a vacancy in the innermost shell is generated. An excited atom's natural tendency is to try to return to a stable energy state. As a result, an electron from an

outer shell fills the produced vacancy, and electromagnetic radiation in the form of distinctive X-ray is released. The emission of an electron, the so-called Auger electron (Figure **2.2** (c)), may also be released during the de-excitation of the system. Figure **2.2** shows k-shell ionization, X-ray emission, and Auger electron emission. For heavy elements, the probability of emitting an X-ray quantum (fluorescence yield) is near to one, but just a few percent for light elements.

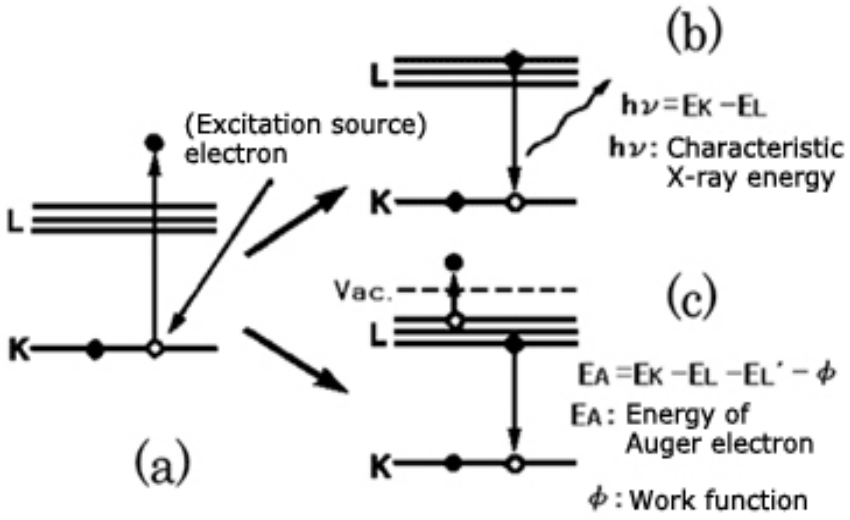

Figure 2.2. Ionization process: **(a)** k-shell ionization, **(b)** X-ray emission, and **(c)** Auger electron. [88]

The energy levels of the electrons in the atom simply determine the X-ray spectrum. Figure **2.3** shows the energy level diagram of a medium-heavy element with X-ray transitions. K X-rays are used to represent transitions to the K shell. When an electron fills the vacancy and comes from the L shell, the transition is designated as K_{α}, and when it arrives from the M shell, it is marked as K_{β}. Similarly, L X-rays are used to identify transitions to the L shell, and they contain certain components. Generally, the light and medium-heavy elements are often recognized by their K X-rays and the heavy elements by their L X-rays due to the accurate detection of the K X-rays which can be acquired in the range $20<Z<50$ and of the L X-rays for $Z>50$.

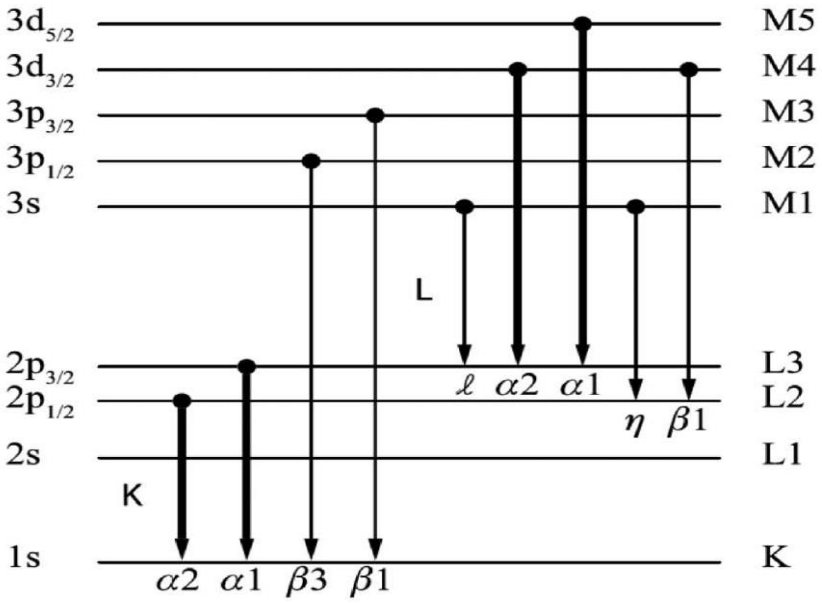

Figure 2.3 Energy levels and X-ray transitions in medium-heavy element. [89]

2.1.2 An Outline of the PIXE Technique

Accelerators employed for PIXE analysis are reasonably sized machines that provide a beam of protons, helium, or even heavier ions with few MeV energy. Figure **2.4** shows the schematic view of a typical in-vacuum PIXE arrangement. During the development of PIXE, most frequently Van de Graff (VdG) accelerators provided the particle beam. This accelerator maintains a terminal voltage of typically 2-3 MV using a continuous moving belt in a high-pressure tank. As a result, the accelerator can create protons with an energy of 2-3 MeV and He^{2+} ions with energies of double that. These machines are able to generate beam currents with many tens of microamperes. For PIXE analysis, which typically uses a few tens of nano amperes, such currents are extremely high.

In ion beam analysis, including PIXE, a new generation of small tandem accelerators has recently been used. Because it applies half the voltage required by a traditional machine, the tandem machine has become a favorite choice for IBA laboratories. The negatively charged ions accumulate energy in this accelerator owing to a very high positive voltage at the geometric center of the pressure vessel. Some electrons are removed from the ion as it reaches the high voltage terminal in the center. The ion then turns positive, and the strong positive voltage accelerates it

again. The charged particles are first pulled and then pushed by the accelerator in two steps. A common choice is a tandem machine with a terminal voltage of 1-3 MV. A 1.5 MV machine generates protons with a 3 MeV energy, which is sufficient for PIXE analysis.

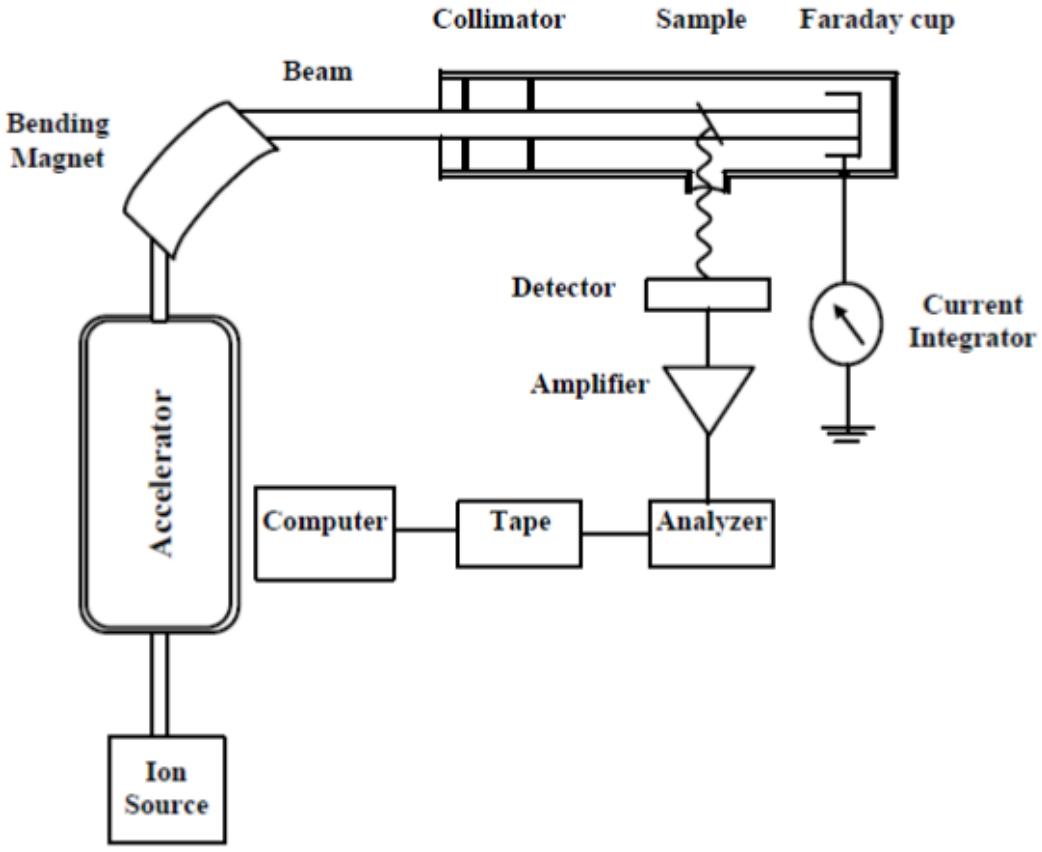

Figure 2.4. Typical arrangement for PIXE technique [90]

The beam from the accelerator goes via a bending magnet first. By sending the beam through a slit, it is stabilized. Any tiny energy changes within the accelerator can influence the deflection of the magnet. As a result, an imbalance in the currents is trapped by the slit's left and right edges. These currents provide a differential signal, which is amplified and used in a feedback loop to adjust the accelerator's principal working voltage. Electrostatic and magnetic steering devices are used to direct the energy-analyzed beam axially along the beam-line. The beam then moves into the target chamber through a beam-transport system.

The pressure in the chamber is around 10^{-6} torr. In order to eliminate the necessity for frequent opening and re-evacuation, a higher number of samples are usually placed in the target chamber. A number of auxiliary equipment are required in the chamber. Among the primary gadgets are an X-ray detector and a Faraday cup. X-rays emitted by the target are collected by the X-ray detector, and the incident beam current on the target is monitored by the Faraday cup. Thin targets allow the beam to pass through with only a little amount of energy loss, which is measured using a Faraday cup. Thick targets, on the other hand, completely block the beam and need a different setup. One solution is to isolate the whole chamber from the beamline, and then the chamber itself functions as a Faraday cup. This was the solution in the PIXE measurement chamber at the ATOMKI VdG5 accelerator [91]. In case of not isolating samples it is possible to measure the beam on the target itself.

Characteristic X-rays emitted by the target are recorded by an X-ray detector. The most common types of X-ray detectors used to detect X-rays are:

Gas-filled detectors work on the principle that X-ray photons have the ability to ionize inert gas atoms like argon or xenon into an electron (e^-) and an ion (for example, Ar^+) pair. One X-ray photon can produce several hundred ion pairs because the ionization energy needed to release an outer electron is low (10-20) eV in comparison to the energy of the X-ray photon (8 keV). A disadvantage of gas-filled detectors is their loss of linearity at high count rates

Scintillation detectors work by converting X-ray photons in a two-step process into an electrical signal. The coating of a sodium iodide crystal with thallium doping is formed when the X-ray photon collides with a phosphor screen, also known as a scintillator. The latter generates photons in the visible spectrum's blue region. Then, a photo-multiplier tube positioned directly behind the scintillator transforms these into voltage pulses. The number of visible photons that impact the photocathode and the energy of the initial X-ray photon are both proportional to the number of electrons that are ejected by the photocathode. Regarding a lot of losses, the energy resolution of the detector is poor, which prevents it from being utilized to resolve X-ray photons due to K_α and K_β radiation.

Semiconductor Detectors, A substance that can act as both an insulator and a conductor is known as a semiconductor. Semiconductor detectors have a (p-i-n) diode structure in which the intrinsic

(i) region is formed by the depletion of charge carriers when a reverse bias is placed across the diode. Charge carriers (holes and electrons) are released and swept to their respective collecting electrodes by the electric field as a result of photon interactions in the depletion region. A charge-sensitive preamplifier transforms the resultant charge into a voltage pulse with an amplitude proportional to the initial photon energy. Due to the development of semiconductor detector technology, energy dispersive X-ray spectrometry became superior in many fields of application and for all types of X-ray excitation (electrons, ions, or photons).

Data from the detector is sent into the computer through the processing unit, amplifier, ADC, and MCA. The data is then represented using computer software as a spectrum. Figure **2.5** shows a PIXE spectrum of urban dust sample. It has a number of characteristic X-ray peaks.

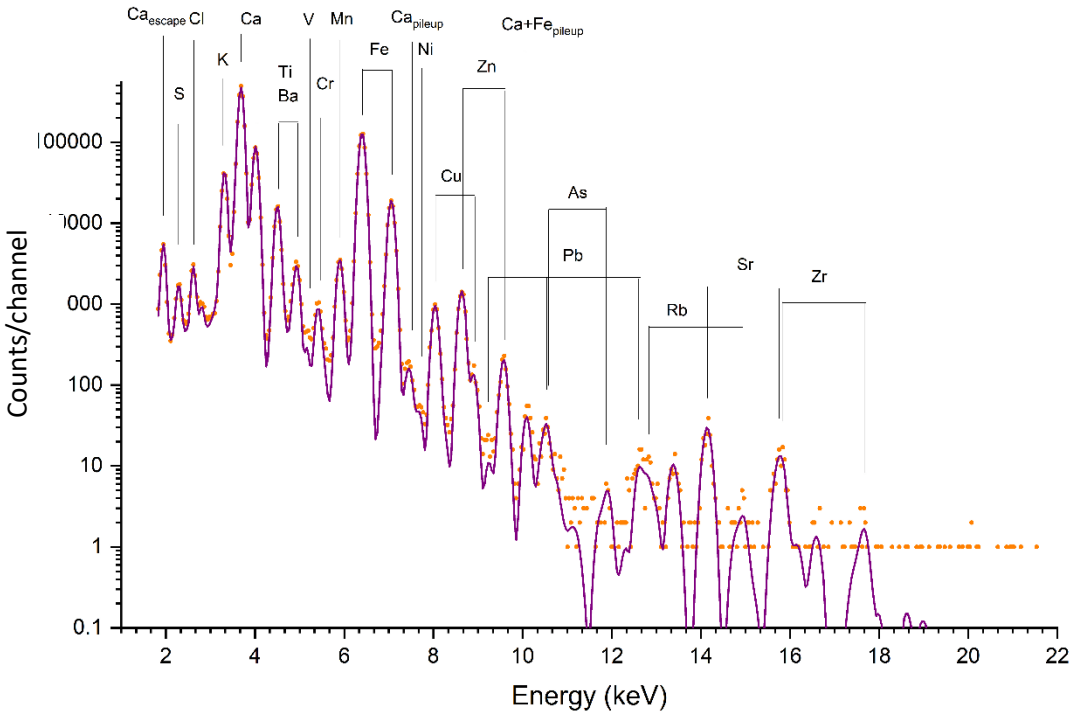

Figure 2.5. PIXE spectrum of urban dust sample

Due to a variety of atomic bremsstrahlung events, as well as Compton scattering of gamma rays from nuclear reactions caused by the beam, the spectrum is imposed on a background. There are several physical reasons for the presence of the continuous background in the PIXE spectra. In the

lower-energy part, the continuous spectrum is higher and arises mainly from Bremsstrahlung radiation. While in the higher-energy part of the PIXE spectrum the continuous background originates mainly from the Compton interactions of gamma radiation in the detector. The typical energy range of a PIXE spectrum (1 keV – 25 keV) covers K lines of light and medium heavy elements (Na-Zr) and L-lines of heavy elements (Z > 50, for example, Ba, Pb). The figure shows a significant number of X-ray peaks corresponding to trace components of dust indicating PIXE's good sensitivity. The area of the associated peak is proportional to the element's concentration in the material.

Due to the large number of overlaps and the extremely energy-dependent background, manual spectrum analysis is difficult and unfeasible. The foundation of a quantitative PIXE analysis is the extraction of X-ray peak regions from the PIXE spectrum and their correlation to the concentration of a certain element. There are several different PIXE software programs available today, and the majority of them can calculate both the X-ray peak regions (intensities) and corresponding elemental concentrations.

The first step in the quantification process is to extract the X-ray intensities from the PIXE spectra. Almost all the programs are based on fitting the model spectrum to the experimental one using the least square method. The main difference between them comes from the different approaches in background and peak shape treatments.

In the early days of PIXE empirical calibration curves were used to determine the relationship between X-ray intensities and elemental concentrations. These were only applicable to specific sample type such as thin samples, or thick samples with specific matrix compositions. This approach greatly limited the applications of PIXE at that time. Improvements in the accuracy of the data base describing all physical processes involved in X-ray detection, enabled computer modelling of the whole PIXE experiment. Nowadays, PIXE software packages are available to calculate elemental concentrations directly from a PIXE spectrum.

Many software packages are available for fitting and quantification of PIXE spectra such as GEOPIXE [92], GUPIX [93], AXIL [94], and PIXYKLM [95].

2.1.3 External beam PIXE

Bringing the beam into the air offers numerous advantages compared to doing PIXE in a vacuum. The size, shape and texture of a sample is not an issue anymore because there is enough space for the measurements. The external beam also makes sample change and positioning easier. Bringing the measurement into the atmosphere also lowers the damage that can be caused by the sample heating up at the beam spot. This is because air removes heat through convection. Another advantage is that art and archaeological samples that cannot be placed in the vacuum chamber due to their size or archeological relevance can be simply analyzed by external beam PIXE at atmospheric pressure without causing damage.

In-air PIXE also removes the charging effects of insulating samples [96]. Bremsstrahlung radiation is produced in large quantities as a result of the charging effect. This happens because positively charged ion beams produce a positive charge on the sample surface. When the voltage is high enough, discharge occurs, and electrons accelerate rapidly, resulting in background radiation. In a vacuum, an electron source is usually applied to the sample to eliminate this effect, but this is not required in air.

However, there are certain limitations when applying PIXE in the air. The first is energy loss of the beam on the exit window and in the air till the beam reach the target. The attenuation of the X-rays in the air is also significant in the low-energy region. However, the loss of proton energy and X-ray attenuation can be reduced in a helium atmosphere (Table **2.1**). Furthermore, helium has a lower X-ray absorption than air despite having a higher thermal conductivity.

Current measurement is another issue at external PIXE measurement which might be troublesome. Because the beam ionizes the route it travels in the air, electrons from the ionization route can therefore produce an inaccuracy in current measurement when collecting the charge from the sample. Another thing that might lead to trouble is the fact that measurement geometry must be consistent throughout all measurements, and with external beam PIXE, the set-up is in the lab with no cover. When switching samples, extreme caution should be taken to avoid changing the geometry [97].

Table 2.1. Some characteristics of air and helium using 3MeV proton beam [98].

Material	**Air**	**He**
Density (g/cm^3)	0.00125	0.00017
dE/dx, (3 MeV protons)	12.60 keV/mm	2.21 keV/mm
Range (mm)	139	767
Thermal conductivity (W/m K)	0.026	0.156

As shown in Figure **2.6**, the distance between the exit foil and the sample in a PIXE setup with an external beam must be small to limit the beam's energy loss. The X-ray detector must also be near to the sample in order to detect the low-energy part of the PIXE spectrum. Because of this, most present setups have a nozzle with an exit foil on top. As a result, any object may be placed close to it. A helium environment around the set-up can increase detection efficiency if energy loss and X-ray absorption are still too high.

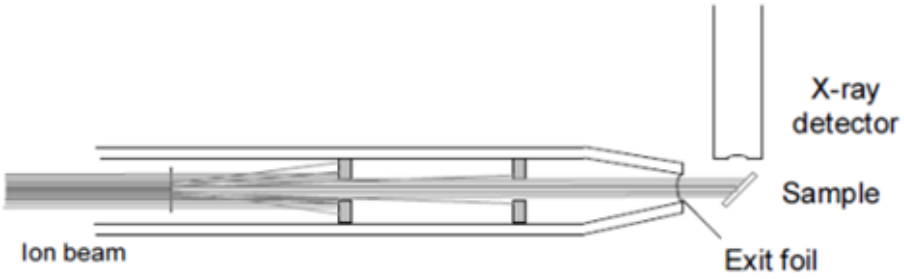

Figure 2.6 a possible external beam PIXE arrangement [99].

Bremsstrahlung and gamma radiation released along the beam path cause a higher background in the PIXE spectrum (exit foil and air). However, in terms of detection limits (LOD), in-air PIXE can be comparable to the conventional PIXE in a vacuum. LOD can be approved e.g., by raising the beam current, as samples in air are much simpler to cool. It is also possible to scan the sample in order to reduce the beam fluence [100]. The background of the spectra can be reduced if all parts in a setup that can get hit by the ion beam are made of graphite.

2.2 Aerosols sampling

2.2.1 Sampling Site

The sampling site was in Debrecen, Hungary's second-largest city (with about 200,000 residents), which is situated in the country's northeast (Figure **2.7**). In the heart of an agricultural region, Debrecen is surrounded by cultivated land (tillage and sward), with some forest to the north. The city has a generally warm and dry climate, with typical summer and winter temperatures of 20.7 and −0.4 °C, respectively, and a mean annual precipitation of ~550 mm. Sand and loess soil types are found along the city's axis since the city lies on the border of two regions: the sandy region of Nyírség and the loess area of Hajdúság [101].

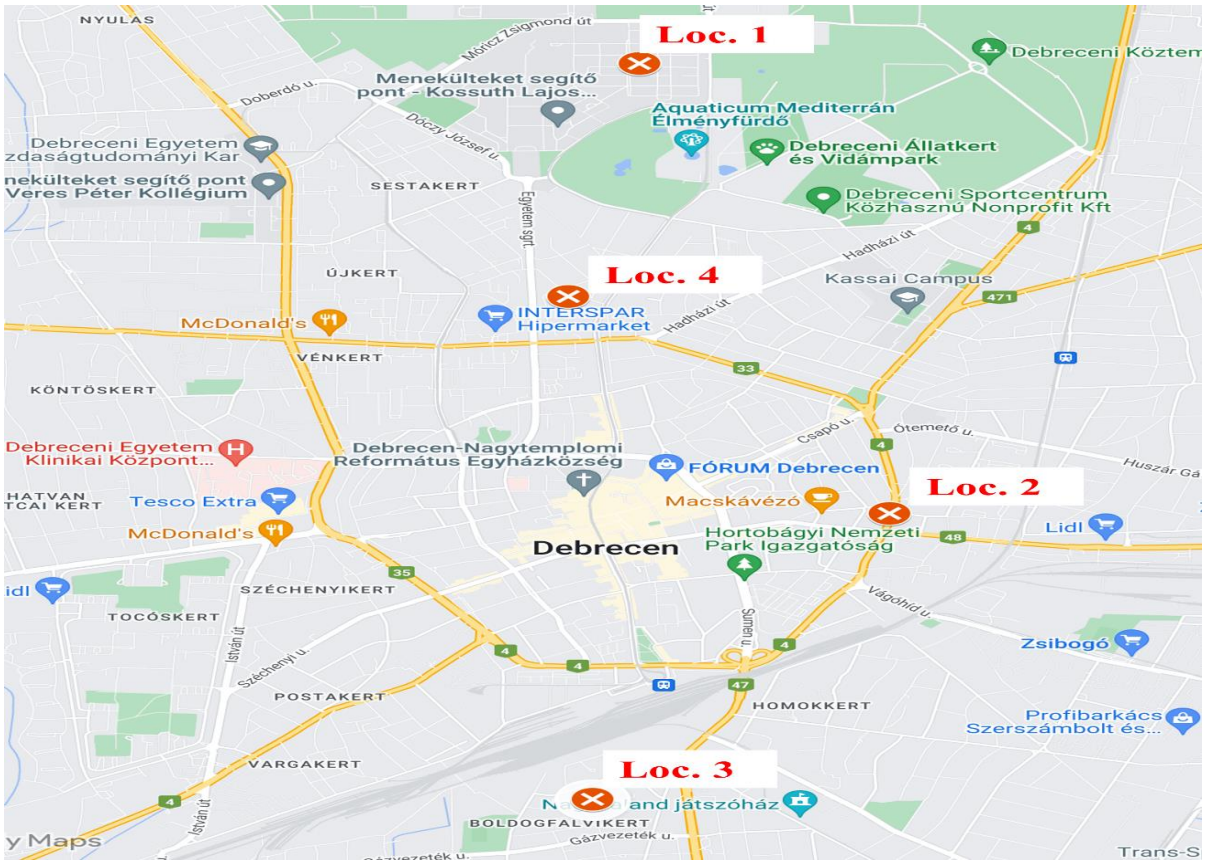

Figure 2.7 The sampling location at Debrecen, (1) Klinika SUB monitoring site of HAQN, (2) Hajnal utca Traffic monitoring site of HAQN, (3) Kaloteszeg ter UB monitoring site of the Hungarian Air Quality Monitoring Network (HAQN), (4) UB sampling site at ATOMKI.

The sampling was carried out ~4 m above ground level on the roof of the building connecting buildings VIII and IX of the Institute for Nuclear Research (ATOMKI, N 47.54445, E 21.62340). ATOMKI is situated in a suburban district of Debrecen, which is surrounded by residential areas and there are two main traffic roads and two tram lines near to the sampling location (Figure **2.8**) [102]. The site can be classified as an urban background since it is not influenced significantly by any single source but rather a combination of sources upwind of the station.

The daily concentrations of NO_2, CO, NO_x, and PM_{10} measured at the three air quality monitoring network sites in Debrecen (as shown in Figure **2.7**) was used as complementary data to our study. This data set allowed time-series data visualization to observe how the data has changed over time and to establish a trend line for each year in order to characterize the overall tendency.

Figure 2.8. ATOMKI sampling station

2.2.2 Aerosols sampler

Aerosols sampling was carried out using a "Gent" Stacked Filter Unit (SFU) PM_{10} sampler [103] shown in Figure **2.9**. It consists of the following main components:

1. A NILU filter cassette
2. A black polyethylene container equipped with a pre-impaction stage from PM_{10}
3. Rain protection cover
4. A needle valve to regulate the flow rate
5. A vacuum gauge
6. A vacuum pump
7. A gas flow meter
8. A precision gas volume meter
9. A time switch and an hour meter

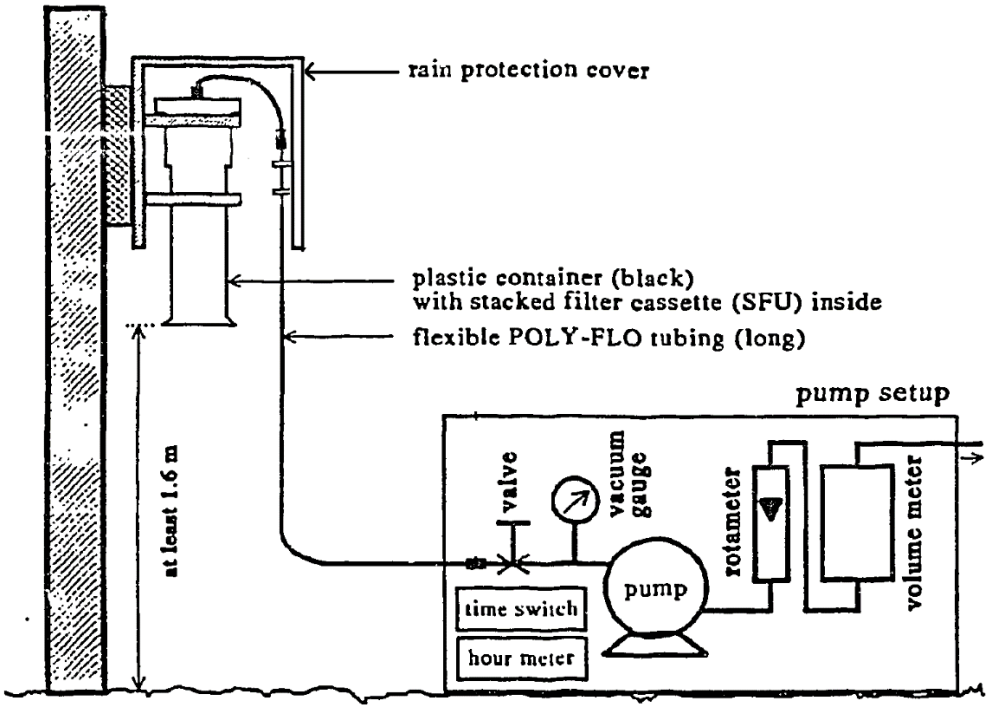

Figure 2.9 Schematic diagram of the two-stage sampler [103]

The stacked filter cassette is a double type filter holder (Figure **2.10**), which is loaded with 2 different Nucleopore type polycarbonate (PC) filters with 47 mm diameter: one with 8 µm pore size as 'coarse' filter; the second, 'fine' filter has 0.4 µm pore diameter. The filter with 8 µm pore diameter has a filtration efficiency of 50% at the minimum of the particle size distribution curve at 2.5 µm, which results in particles with an aerodynamic diameter (EAD) greater than 2.5 µm (coarse fraction) adhering to it. Fine particles, (with EAD smaller than 2.5 µm) are almost completely passed through it and can be collected by another Nucleopore PC filter with a pore diameter of 0.4 µm with a nearly 100 % efficiency.

The shiny side is facing up on both the coarse and fine filters (thus, facing the air intake). 12.88 cm^2 of the filter are exposed to the air flow during sampling (for both the coarse and fine filters). During the sampling, the stacked filter cassette is placed inside the black polyethylene container which has a pre-impaction stage. The system operates at an average flow rate of about 17 liters per min (l/m), allowing only particles with EAD ≤ 10µm entering the sampler.

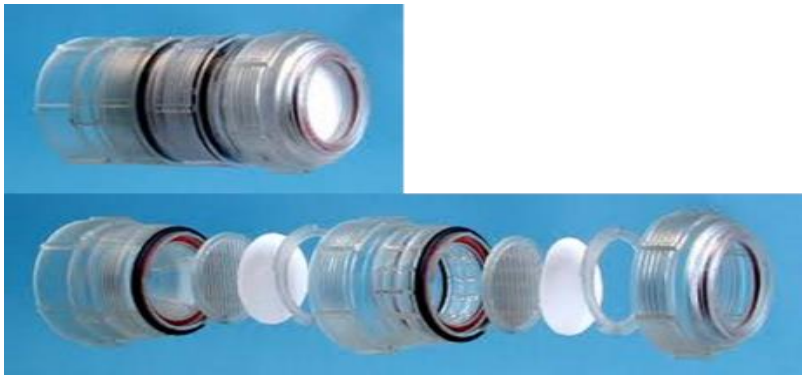

Figure 2.10 NILU filter cassette

2.2.3 Aerosols sampling period

Fine and coarse aerosols samples were collected 2 times a week on workdays from March, 2018 to Feb 2022 as part of the ongoing long-term aerosols research program in the ATOMKI using the above-described Gent SFU. Sampling time was 24 h, and the air filtered through the system varied between (20 and 30) m^3, depending on the actual sampling time and the filter clogging. The exposed filters and field blanks were placed into polycarbonate Petri slide dishes. Parallel to the aerosols sampling local meteorological parameters (temperature, humidity, air pressure, wind

direction, wind strength and rain) were recorded with a micrometeorological station installed next to the sampler.

2.3 Determination of PM mass

The field blanks and actual samples have been weighed before and after sampling with a Radwag microbalance model MYA5 (sensitivity 1 µg) to determine the PM mass concentration (Figure **2.11**). The filters were conditioned for at least 24 hours at a temperature between 22 and 24 °C and a relative humidity of around 50% before being weighed. The filters were exposed to an anti-static ionizer to eliminate any potential static charges. Each filter was weighed at least three times over several days. Repeated weighing of blank and exposed filters over several days led to the development of the uncertainty (in µg) on the net mass of a filter sample for PM mass estimations [104]. The uncertainty (1 standard deviation) of the PM mass determinations was calculated to be 5 µg for the Nuclepore PC filters.

Figure 2.11 the Radwag microbalance with filters in petri slides under conditioning, and the ionisator (right).

2.4 Analysis of Black Carbon (BC)

A portable **M**ulti-Wavelength **A**bsorption **B**lack Carbon **I**nstrument (MABI) developed by The Australian Nuclear Science and Technology Organization ANSTO [105] was used for the evaluation of light-absorbing carbon (Figure **2.12**.)

Figure 2.12 MABI instrument

From ultraviolet to infrared, the MABI device analyzes the absorption of light at seven different wavelengths (405 nm, 465 nm, 525 nm, 639 nm, 870 nm, 940 nm, and 1050 nm). This allows the separation of the contributions from biomass burning (BC_{bb}) and fossil fuel combustion (BC_{ff}) based on varying light absorption from various types of particles at various wavelengths. In order to determine the absorption from the filter substrate at each wavelength, unexposed "blank filters" are first scanned. $\mathbf{I_0}$ refers to these data for blank filters. The exposed filters are then subjected to additional MABI scans. **I** represents the absorption at each wavelength from the filter substrate as well as the collected particles.

The black carbon light absorption coefficient ($\mathbf{b}_{abs}$) in (mm^{-1}) at each wavelength are determined according to Equation (2.1):

$$b_{abs} = 10^2 \frac{A}{V} ln\left(\frac{I_0}{I}\right) \quad (2.1)$$

Where

A is the filter collection area in cm^2,

V is the volume of air sampled through the filter in m^3,

I_o is the measured light transmission through blank filter,

I is the measured light transmission through an exposed filter [105].

The BC concentrations provided in this study were measured at λ = 639 nm.

Black carbon particles formed in high-temperature burning (e.g., diesel fuel burning) absorb at different wavelengths than BC particles originating from lower temperature wood burning [105, 106]. The absorbance of BC owing to BB is greater at shorter wavelengths than at longer wavelengths, whereas the absorbance of BC formed in fossil fuel burning is the opposite: it is greater at longer wavelengths. As a result, the difference in concentrations measured at short (405 nm) and long (1050 nm) wavelengths can be utilized to distinguish between these sources. When the concentration difference is high and positive, BC comes from BB; when it is low or negative, BC comes from high-temperature fossil oil combustion.

2.5 PIXE measurements

Particle Induced X-ray Emission (PIXE) technique is one of the most popular environmental analytical methods in ion beam analysis as discussed before in section 2.1, since it allows the simultaneous analysis of elements with Z > 10 in a single short measurement run. For decades, this method has been widely used to detect and quantify trace elements.

In ATOMKI, facilities dedicated for ion beam analysis and application were built around the 5MV VdG accelerator. An in-vacuum PIXE system was in operation since 1983 [93] which was used for the elemental characterization of atmospheric aerosols, biological and environmental samples. Micro-PIXE became available with the installation of the ATOMKI scanning nuclear microprobe in 1995 [107]. In 2015 an in-air micro-PIXE measurement system has been developed as an

extension of the scanning nuclear microprobe [108]. In 2020, after 50 years of smooth operation, the VdG5 accelerator was shut down because neither the personal nor the technical conditions were any more ensured for further operation. In 2014, a new 2MV Tandetron accelerator was installed as part of an infrastructure development program. Some users progressively switched from the VdG-5 to the Tandetron when the beamlines of the Tandetron became available. Among the 9 available beamlines of the Tandetron 4 is dedicated to ion beam applications, including an external millibeam [109].

PIXE measurements presented in this work were done on the new in-air millibeam setup of the Tandetron accelerator. The detailed description of the setup and its analytical characteristics are presented in Chapter 3.

2.6 PIXE spectrum evaluation

The X-ray spectra were quantitatively analyzed using the GUPIXWIN software [110]. The software uses a non-linear least-squares fitting algorithm to analyze PIXE spectra. Using the fundamental parameter approach, the element concentrations in the samples are quantitatively determined from the X-ray characteristic peak area. Spectral interferences in the X-ray spectra produced by escape and pile-up effects could be automatically resolved using GUPIXWIN. The software requests the following instrumental parameters: experimental geometry, detector information, absorber thickness, incident particle energy, and net charge accumulated. The formula used by GUPIXWIN to determine elemental concentrations is as follows:

$$C_z = \frac{Y(Z,M)}{Y_{It}(Z,M).H.Q.\varepsilon_z.t_z} \tag{2.2}$$

Where Y (Z, M) is the yield of element Z in a matrix M,

Y_{1t} is the theoretical intensity or yield per micro- Coulomb of charge per unit concentration per steradian,

Q is the measured beam charge,

ε_Z is the intrinsic efficiency of the detector,

t_z is the transmission of the respective X-rays through any absorber placed between the detector and the target.

The aerosol samples were considered as 'thin' samples (i.e., the energy loss of the irradiating beam on the sample is negligible and there is no self-absorption of the emitted X-rays). After blank correction, the concentration of 25 elements (O, Na, Mg, Al, Si, P, S, Cl, K, Ca, Ti, V, Cr, Mn, Fe, Co, Ni, Cu, Zn, As, Br, Rb, Sr, Zr, Ba, and Pb) was determined.

2.7 Source apportionment by Positive Matrix Factorization

To characterize the sources of atmospheric aerosols, I used the EPA (Environmental Protection Agency, US) positive matrix factorization (PMF) receptor model version 5.0 [111]. PMF has been used to study a range of air pollutants, including particulate matter, volatile organic compounds, and heavy metals [112], [113]. Its purpose is to identify the main sources of pollution and evaluate their contributions to the PM mass. Receptor models use a mathematical algorithm to determine a source's contribution based on the source's composition or "fingerprint," which are represented as factors.

The mathematical expression of the PMF receptor model can be written as follows:

$$x_{ij} = \sum_{k=1}^{p} g_{ik} f_{kj} + e_{ij} \tag{2.3}$$

Where X_{ij} is the measured concentration of the j element in the i^{th} sample, **P** is the number of factors, g_{ik} is the contribution of the k^{th} source to the total concentration of the i^{th} sample, f_{kj} is the concentration of the element j from the source k and e_{ij} is the residual.

This approximation automatically excludes negative source contributions when solving the problem. In the following, the above system of equations is solved by global minimum search - weighted by the error of the measured value,

$$Q = \sum_{i=1}^{n} \sum_{j=1}^{m} \left[\frac{x_{ij} - \sum_{k=1}^{p} g_{ik} f_{kj}}{u_{ij}} \right]^2 \tag{2.4}$$

Where u_{ij} is the uncertainty of the j^{th} constituent in the i^{th} sample and Q is the objective function.

The model gives us an opportunity to handle uncertainty in multiple ways: for example, the specific error of the measurement can be specified, and on the other hand, it is possible to take the detection limit into account during the solution.

In our case, the uncertainty was calculated as suggested in [114]:

$$\mathbf{UNC} = \sqrt{(\mathbf{Error\ fraction} \times \mathbf{concentration})^2 + (\mathbf{0.5} \times \mathbf{MDL})^2} \tag{2.5}$$

Where MDL is the method specific detection limit, and the error fraction is the estimated measurement uncertainty of the given species.

Concentration values less than MDL were set to ½ MDL, and their uncertainty to 5/6 MDL. Missing data were replaced with the geometric mean of the variable, and the corresponding uncertainty was set to 4 times the geometric mean.

Before using the program, it is necessary to check the measurement data in advance and filter out possible measurement uncertainty. The PMF model offers three options for this task:

1. Measuring of concentrations and their uncertainties

The PMF model can determine (individually for each measurement) the signal/noise ratio (S/N),

$$\left(\frac{S}{N}\right)_j = \sqrt{\frac{\sum_{i=1}^{n}(x_{ij} - s_{ij})^2}{\sum_{i=1}^{n} s_{ij}^2}} \tag{2.6}$$

Which indicates whether the measured value is a real signal or just a fluctuation of the background noise. Based on the obtained value, signals are divided into three groups: the signal is nothing but noise (bad) if S/N < 0.2; the signal is weak if 2 > S/N > 0.2; and the measured value is significant

if S/N > 2. Based on this, individual values can be weighted or excluded from the actual factorization [115].

2. Scatter diagrams of concentrations

If there is a correlation on the scatter diagram of two element concentrations, it is assumed that they come from the same source. This should also be reflected in the result provided by the PMF model, so it can serve as a quick test for the goodness of the generated model.

3. Time series of concentrations

The analysis of the time series of the element concentrations creates an opportunity to recognize the pattern of changes and to filter out any significantly different data, whether they come from a measurement error or an external event that occurred during the measurement. The similarity of the curves over time may also indicate a common source.

After the preprocessing operations, it is possible to perform matrix factorization specifically. During the run, it is advisable to carry out the minimum search procedure several times since the trajectories started from different points of the phase space may even show divergence. Only solutions converging to the global minimum can be taken into account during the analysis. The obtained Q-value is nothing but the "goodness-of-fit" parameter, which gives the goodness of the analysis.

The most important result from running the PMF model is the identification of profiles and their corresponding distributions. The program generates two graphs for each source, which on the one hand display the components of the factor, and on the other hand the contribution of the components to the factors. To check the solution, (1) it is possible to determine how well the selected solution approximated the concentrations from the residual analysis. (2) Scatter diagram between the estimated and calculated concentrations, which provides guidance for reducing the statistical weight of the components or even omitting them from the analysis in case of insufficient correlation; and (3) the time diagrams of the estimated/calculated concentrations, which are also used to filter out erroneous data. The program offers several ways to analyze the resources/contributions received:

- The aggregated distribution graph offers an opportunity to review the distribution of data in annual, seasonal, and daily resolution. In the figures, the interquartile (25-75) % range, the distribution (5th and 95% percentiles), and the median are shown separately to aid the analysis.
- The G-phase space graphs offer an opportunity to decide whether the obtained factors are really independent of each other. If the points of the phase space fill the entire diagram area, the G-phase space indicates with great certainty the independence of the factors. On the other hand, if they are concentrated on one spatial element, and unrealistic edges can be drawn on the scatter diagram - which correspond to the rotated position of the coordinate axes - the independence of the factors is not guaranteed. The PMF program by post-processing the data (and since positive matrix factorization is a linear transformation) allows applying a rotation transformation and ensuring independence.
- The pie charts show in detail, from measurement data to measurement data, the percentage contribution of the elements to the various factors.

The critical point of the PMF model is handling the error of the solution. The program uses the bootstrap procedure for this purpose. As part of this, it generates samples based on the measured values obtained as a given starting value and their errors, and then applies the solution generated by the PMF model to the sample population. The errors from the bootstrap procedure give the values of the errors relative to the original data.

In this work, PMF analysis was performed for the fine and the coarse fraction separately. The composition if the samples was determined using PIXE technique, which provided concentrations in ng/m^3 for all variables. The data set contained components unique to each source, allowing the sources to be differentiated and their contributions specified. There were 340 samples and 25 variables in each data matrix. Only species with concentrations above the method detection limit in more than half of the samples were included in the analysis. Because of this criterion, in the model runs Cr, As, Sr, and Zr were set as bad variables in the coarse fraction, and Cr, As, Sr, P, and Zr were set as bad variables in the $PM_{2.5}$. An extra 7% modelling uncertainty was included. Table **2.2** summarizes the parameters of the PMF analysis used in this study.

Table 2.2. Summary of the PMF input, modelling parameters, output, and diagnostics

	$PM_{2.5}$	**PM_{coarse}**
Input data		
No of samples	340	340
Species	BC, Na, Mg, Al, Si, S, Cl, K, Ca, Ti, V, Mn, Fe, Co, Ni, Cu, Zn, Br, Ba, Pb	Na, Mg, Al, Si, P, S, Cl, K, Ca, Ti, V, Mn, Fe, Co, Ni, Cu, Zn, Br, Rb, Sr, Ba, Pb
No. of used species	20	22
Weak variables	Mg, V, Mn, Co, Ni, Cu, Br, Ba	Na, Mg, Cl, V, Co, Ni, Br, Rb, Sr, Ba
PM mass	Total variable (weak)	Total variable (weak)
Extra modelling unc.	7%	7%
Factors	8	8
F-peak test	Yes, Fpeak=-0.2, dQ_{robust}= 0.33%	Yes, Fpeak=0
Constrain	No	No
Diagnostics		
Q robust	2671.79	2299.32
Q true	2682.61	2308.22
Qtrue/Qexpected	2.27	1.98
DISP % DQ	-0.004	-0.007
DISP swaps	0	0
BS mapping	100% all factors	100% all factors
Correlation between modelled and measured conc. (r^2)	Strong variables: 0.88 – 0.98 weak variables: 0.47 - 0.88 PM: 0.89	Strong variables: 0.91 – 0.99 weak variables: 0.41 - 0.99 PM: 0.83

The model was run with factor numbers between 6 and 10 to find the highest number of factors with physical meaning.

The following factors have been taken into account in order to find the optimal solutions: the difference between the measured and expected Q should be as small as possible, the solution should be stable over several runs (50 random model runs were performed), the modelled species should have a normal distribution, the uncertainty-scaled residual should be between ±3, and the obtained source profiles should have physical meanings [116]. The correlation between modeled and real concentrations showed that most samples and species were well modeled.

The solutions were analyzed using classical bootstrap (BS) and displacement of factor elements (DISP) [114]. The number of bootstrap runs was set to 100, the minimum correlation R-value was set to the default 0.6 in all cases, and the BS uncertainty range for each factor profile was defined as the 5^{th} and 95^{th} percentiles. The BS results showed that the factors were reproduced at the minimum level in 98% of the produced resamples and that there were no swaps for the minimum dQ level with DISP, showing that the factors were well-defined.

The rotational ambiguity of the solutions was explored with the FPEAK tool for parameters ranging between – 1 and + 1. The impact of small rotations on the Q values, F and G matrices as well as scaled residuals was negligible in all cases. FPEAK value = -0.2 was chosen for $PM_{2.5}$ to sharpen the G matrix.

2.8 Trajectories calculation and clustering

To identify the origin of various pollutants and to differentiate between local, regional, and remote contributions, I used trajectory statistical methods (TSM). Dutton [117] defines trajectory as the paths of infinitely small air particles. Backward trajectories indicate where a particle came from, while forward trajectories define where it will go. Trajectories have been used for many years to interpret individual flow events, but statistical approaches for large sets of trajectories were just recently developed.

In this study, three well-known methods for source localization were performed using the HYSPLIT model and 'openair' R package [118], namely the cluster analysis (CA) of the back trajectories method, the method of potential source contribution function PSCF [119], and the concentration weighted trajectory method CWT [120], respectively.

Cluster analysis is a multivariate statistical technique that is increasingly being used in air pollution research to provide information about the source of air masses that arrive at the site. This method divides the trajectory data into several transit clusters using Angle distance or Euclidean distance method [121]. The Euclidean distance method can classify backward trajectories based on velocity and airflow direction [122]. The 4-day backward trajectories served as the input variable for the cluster analysis. For each cluster, an average trajectory was calculated.

The PSCF method can provide a probability map of the areas surrounding a receptor site based on the allocation of air mass residence time, allowing potential sources affecting air quality at the receptor site to be identified [123]. Based on a threshold value, each trajectory is categorized as polluted or clean. The geographic region was divided into grid cells at 0.25° × 0.25° resolution based on the backward trajectories modelling results, and the PSCF value for the **ij**th grid cell is specified as:

$$PSCF_{ij} = \frac{m_{ij}}{n_{ij}} \tag{2.7}$$

Where n_{ij} is the number of occasions when a trajectory passes the cell with coordinates (i, j), m_{ij} is the number of occasions associated with high pollution levels at the receptor site.

Since PSCF is a conditional probability function, there is a high level of uncertainty when the airflow's residency duration in the grid is short, that is, when n_{ij} is less than three times the average number of trajectory endpoints (Avg) of all grid cells in the study area. To reduce uncertainty, an arbitrary weight function W_{ij} is multiplied by the PSCF [124] [125], which is defined as WPSCF and can be derived using Eqs. 2.8 and 2.9 below:

$$WPSCF_{ij} = PSCF_{ij} \times W_{ij} \tag{2.8}$$

$$W_{ij} = \begin{cases} 1.00 & n_{ij} > 3Avg \\ 0.70 & Avg < n_{ij} \leq 3Avg \\ 0.42 & 0.5Avg < n_{ij} \leq Avg \\ 0.17 & 0 < n_{ij} \leq 0.5Avg \end{cases} \tag{2.9}$$

PSCF, on the other hand, only represents the proportion of polluted trajectories in grid cells and cannot reflect their contribution to receptor sites. As a result, the **CWT approach** was utilized to calculate the average weight concentration (C_{ij}) of the ijth grid, analyze its pollution contribution

to the target grid, and identify predicted source regions. The following is the calculation formula [126]:

$$C_{ij} = \frac{\sum_{l=1}^{M} C_l \mathcal{T}_{ij} l}{\sum_{l=1}^{M} \mathcal{T}_{ij} l} \quad (2.10)$$

Where C_{ij} is the average weighted concentration in the grid cell (i,j), l is the trajectory index, M is the number of trajectories associated with the grid cell (i,j), $\tau_{ij}l$ is the residence time of trajectory l at the cell (i,j), and C_l is the concentration measured at the receptor site associated with trajectory l. Since spatial and vertical differences in pollutant abundance along the trajectories can produce uncertainty in concentration contribution to the receptor site, the W_{ij} was also used in the CWT method to reduce uncertainty.

The HYSPLIT model version 5.2, made by the National Oceanic and Air Administration (NOAA) in the United States [127], was used to calculate 96-hour backward trajectories starting at the sampling location. This model is a system for simulating complex dispersion and deposition simulations as well as air mass trajectories. Meteorological data fields for running the model are available from the Global Data Assimilation System's (GDAS1) archived meteorological data. Using the default vertical motion model, three back-trajectories were computed at 12:00, 20:00, and 4:00 CET for each day at different starting heights (200, 500, and 1000 m AGL) to evaluate the effect of release height on clustering analysis and possible source area identification.

3 Results and discussion

3.1 Development and characterization of the new in-air millibeam PIXE setup at the ATOMKI Tandetron Accelerator

A 2 MV Tandetron accelerator by High Voltage Engineering Europa HVEE [128] was installed in 2014 with the financial help of the Hungarian Academy of Sciences infrastructure grants to create a modern Accelerator laboratory.

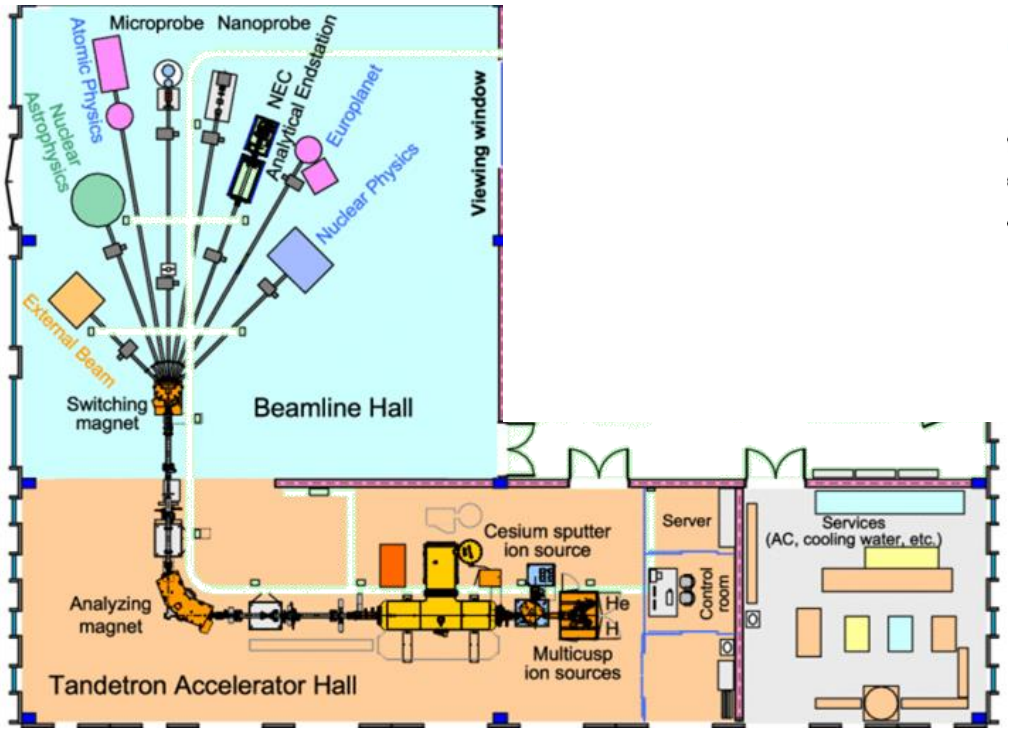

Figure 3.1 Layout of the ATOMKI Tandetron Laboratory.

At first, a duoplasmatron ion source (Model 358) with an injector magnet was deployed in January 2015. A 9-port switching magnet was put right at the Tandetron's exit in May 2015. At that time four experimental beamlines were operational for various purposes: nuclear astrophysics, external beam, scanning ion nano probe, and nuclear physics, respectively, at (+45, +20, 20 and 45) degrees. As a second phase of development, the system was upgraded with two multicusp ion sources (for hydrogen and helium beams, SO120 and SO130, respectively) and a 90-degree analyzing magnet. In addition a cesium sputter ion source (Model 860C) has replaced the duoplasmatron ion source,

which can create negative ion beams from most heavy elements. The switching magnet was placed to its permanent position at the exit of the analyzing magnets. The design of the 9 beamlines have been started. The current layout of the accelerator and its beamlines are presented in Figure **3.1**. [129]

3.1.1. The External Beamline

The left 45^{o} beamline is dedicated for in-air experiments. Usually, in most Ion Beam Application IBA laboratories external-beam PIXE and IBA has an own beamline, so permanent setups are built. In our case the external beamline has many users who has many different setups. Therefore, we had to develop a mobile setup which can be easily fitted to and removed from the beamline while at the same time it has similar characteristics as permanent systems. The in-air PIXE setup was built on a table with 100 cm x 100 cm dimensions. On the top the measurement system itself containing the detectors, the sample stage and the Faraday cup is placed. On the lower shelves the data acquisition system, detector electronics, a current monitor and the measurement control computer can be found. The setup is connected to the beamline end with a KF-40 welded bellows.

3.1.1.1 Exit window

One of the most important parts of in-air systems in the beam exit window. Beam exits vacuum and delivered to air through a thin foil exit window. The exit window should be vacuum tight, it should produce preferably no interfering radiation (through nuclear reactions or X-rays), the energy loss and straggling of the beam should be kept as low as possible, and not least of all, it should be resistant to beam damage (i.e. should not break and change characteristics during irradiation). In our setup, we use silicon nitride membrane (Si_3N_4 made by Norcada) with a thickness of 200 nm and window size: 2mm x 2mm. (Figure **3.2**) According to our and other's experience silicon nitride films are reliable and long-lasting window materials [130] [108]. At the ATOMKI external micro beam the same extraction window is used and the foil had to be replaced only once due to thinning since 2014. Before the exit window, the beam passes through a series of collimators.

The exit window and the external path in the atmosphere produce beam widening and ion energy loss. In our situation, we used the SRIM code to determine these values in both air and helium. According to this calculation the energy loss of a 2.5 MeV H^+ beam in the 200 nm window and 10

mm air or He atmosphere is 150 keV (in air) and 30 keV (in He), respectively. The range of protons and beam straggling simulated by SRIM is shown on Figure **3.3**.

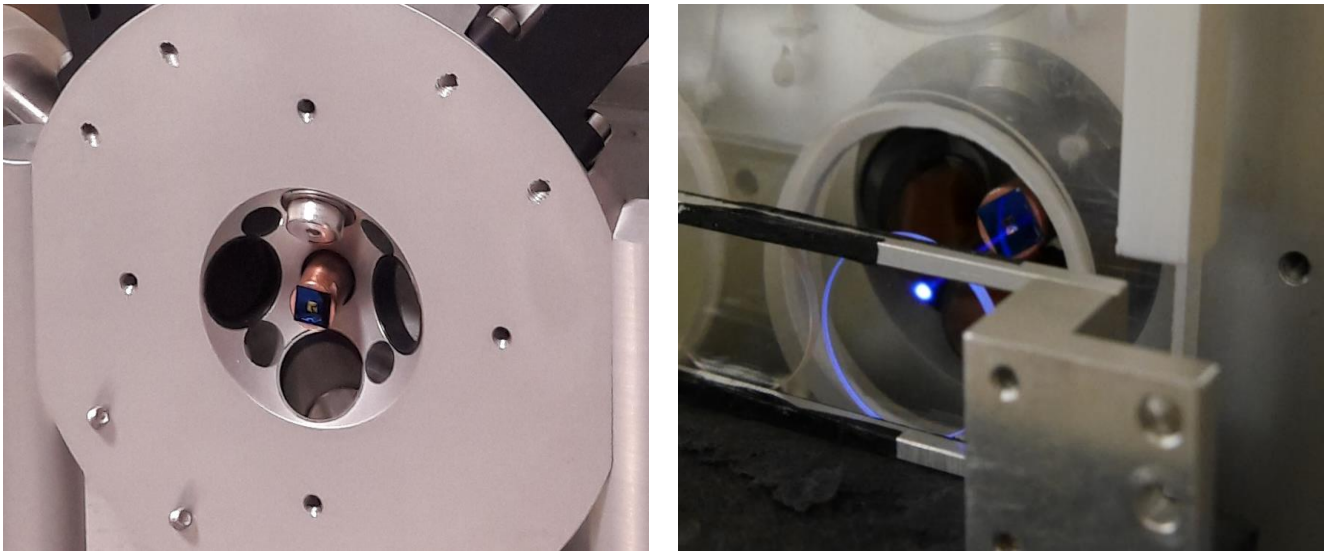

Figure 3.2 Photo of the Si_3N_4 exit window in the setup (left) and when the beam is on (right). Beam energy 2.5 MeV, beam current: 50 nA.

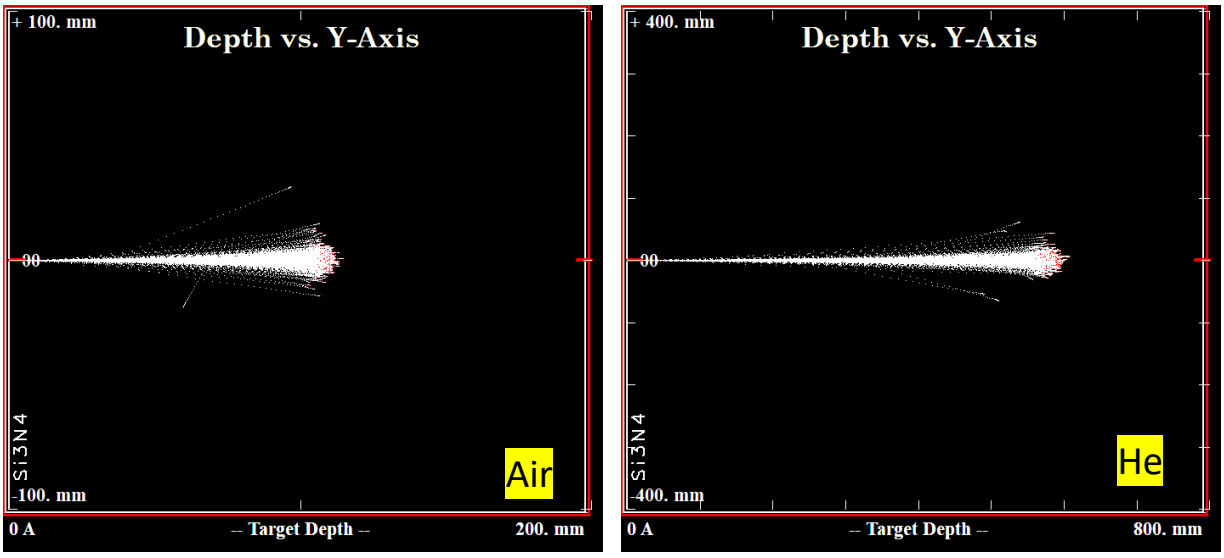

Figure 3.3 SRIM simulation of a 2.5 MeV H^+ beam in air (left) and in He (right) atmosphere. The range of the beam is 125 mm in air and 610 mm in He.

3.1.1.2 X-ray detectors

The set-up was created that way that different arrays of X-ray and other detectors for complementary IBA methods can be used. The default detector combination (Figure **3.4**) is composed of four thermoelectrically cooled Silicon Drift X-ray detectors (SDD) by RaySpec Ltd. that are optimized for detecting X-ray lines with (0.3 – 20) keV, taking into consideration the variations in X-ray production cross sections that span many orders of magnitude.

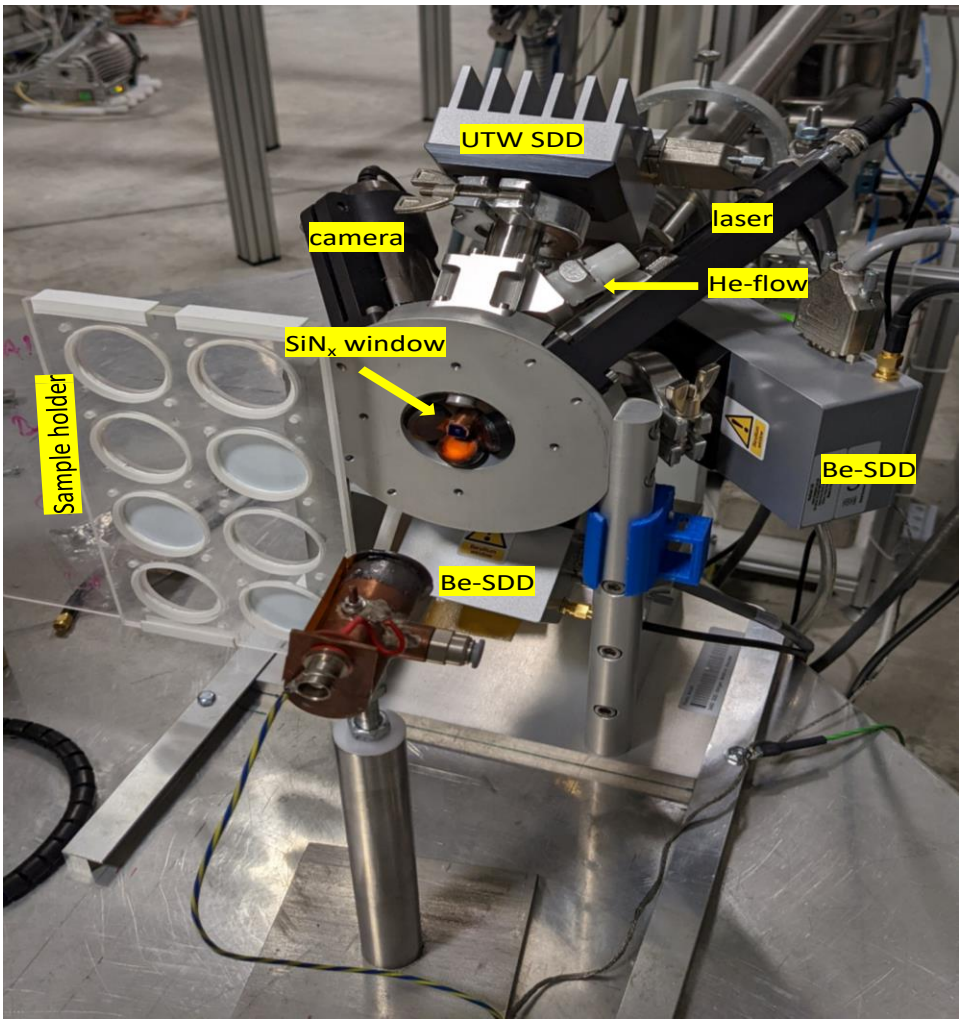

Figure 3.4 Picture of measurement setup with the 4-SDD cluster

Three 65mm² SDD detectors with a 12.5 µm Be window and 450 µm thickness are used in the setup (with 129 eV full width at half maximum (FWHM) energy resolution for the 5.9 keV line of Mn) installed at 135° with respect to the beam direction, at about 12 mm from the target. They used to detect the medium and high energy X- rays (> 3 keV) with excellent efficiency. An additional Kapton foil absorber with 125 µm thickness is placed in front of the detectors in order to attenuate the low-energy X-ray lines and to protect the detectors from the scattered protons, as well. The 3 Be-windowed detectors together cover ~0.45 sr solid angle.

The setup is equipped with another SDD which has an ultra-thin Si_3N_4 window. This SDD serve to measures the X-ray lines with low and medium energy (0.2 – 9) keV, it has energy resolution of 129 eV at 5.9 keV, 0.45 mm nominal thickness and 30 mm^2 active area. The detector is equipped with a pair of 4 cm long permanent magnets of 1T magnetic field each which protects the detector from scattered protons. Scattered beam particles can easily penetrate through the thin window of the detector causing decreased resolution, distortion of peak shapes, and damage to the detector crystal. The ultra-thin window (UTW) detector enables the quantitative analysis of elements down to nitrogen and oxygen. The UTW detector is positioned at 135^o geometry at 80 mm distance from the sample. He flow can be introduced in front of the UTW SDD, if needed. In a 2 (l/min) He flow, the system allows the detection of X-rays down to 0.35 keV, i.e., elements down to N.

The experimental arrangement makes it possible to replace one SDD with a Canberra Si(Li) detector which was used earlier in the old in-vacuum PIXE setup (FWHM 145 eV, active area 50 mm^2 , thickness 5 mm, with 25 µm Be window and additional Kapton foil absorber). The Si(Li) detector is used when we want to enhance the spectrum in the high energy region since it is more sensitive than an SDD in X-ray energies > 15 keV due to the greater crystal thickness. In addition, the detection system can be complemented with an HpGe detector (50% efficiency) and particle detectors, too. See Figure **3.5**.

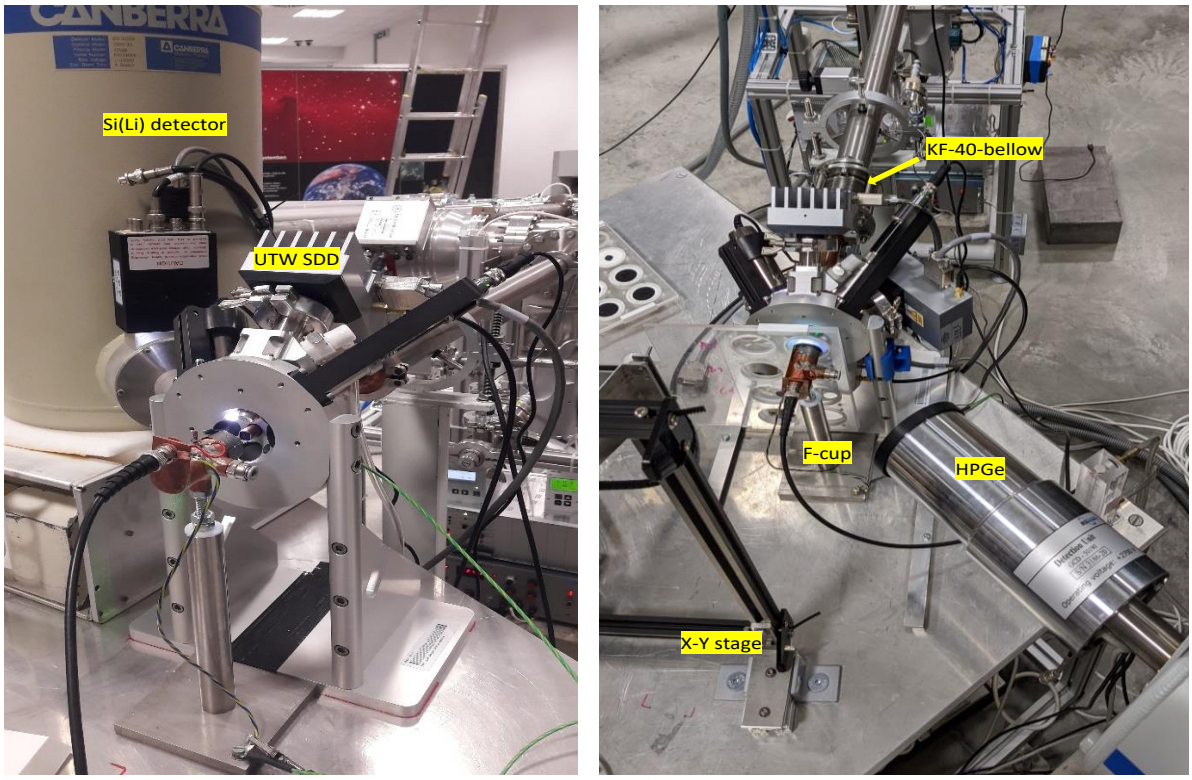

Figure 3.5 Pictures of alternative measurement setups.
(Right) SDD cluster with an HpGe gamma detector by Baltic Scientific during measurement of aerosols samples. (Left) detector arrangement with a Canberra Si (Li) and the UTW SDD.

3.1.1.3. Sample positioning and data acquisition

Samples are mounted perpendicular to the beam on an x-y precision stage. Usually, the samples are scanned in front of the beam (on a few cm^2 area) in order to reduce the risk of possible beam damage and to increase the analyzed area. Data acquisition, sample movement, change and the scanning is controlled remotely in a semi-automatic way. A multi-channel digital X-ray signal processor 'xMAP' by XIA LLC is used for data acquisition.

Two lasers and a digital microscope camera are built in the setup for sample positioning and monitoring. This positioning system is used to adjust the alignment of the setup (i.e., set and check the position of the samples relative to the detectors) every time when it is mounted on the beamline. On the other hand, samples are continuously monitored during the measurements via the camera.

In the case of aerosols samples, when the sample is thin enough for the beam to pass through, the irradiation dose is measured by integrating the current on a Faraday cup placed behind the filters. The Faraday cup is coated with 2 layers of thick carbon foil which prevents the emission of X-rays from it.

3.1.2 Performance of the new experimental setup

PIXE spectra collected on NIST SRM2783 reference sample (urban dust on filter media) are shown on Figures (**3.6** and **3.7)**. X-rays originating from medium and high Z elements (Cl to Pb) were detected by the three Be window SDD detectors equipped with a 125 µm Kapton foil absorber. The 3 identical detector was handled as one detector cluster (3-SDD cluster), and the spectra recorded by them were summed. The UTW SDD detector recorded X-rays from low and medium Z elements (from N to Zn). Beam energy was 2.5 MeV, beam current ~ 50 nA, and the accumulated charge on the sample was 10 µC. The measurement was carried out both in air and in a 2 (l/min) He flow. The effect of the helium atmosphere on the detection of light elements is clearly visible.

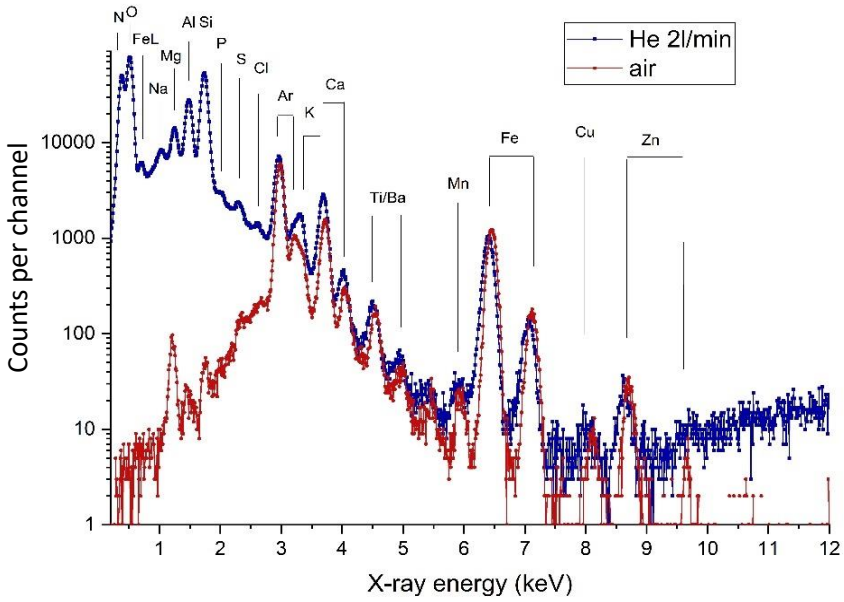

Figure 3.6 PIXE spectra recorded on NIST SRM2783 by the UTW SDD detector in air and under He flow of 2 (l/min). The main characteristic X-ray lines are indicated.

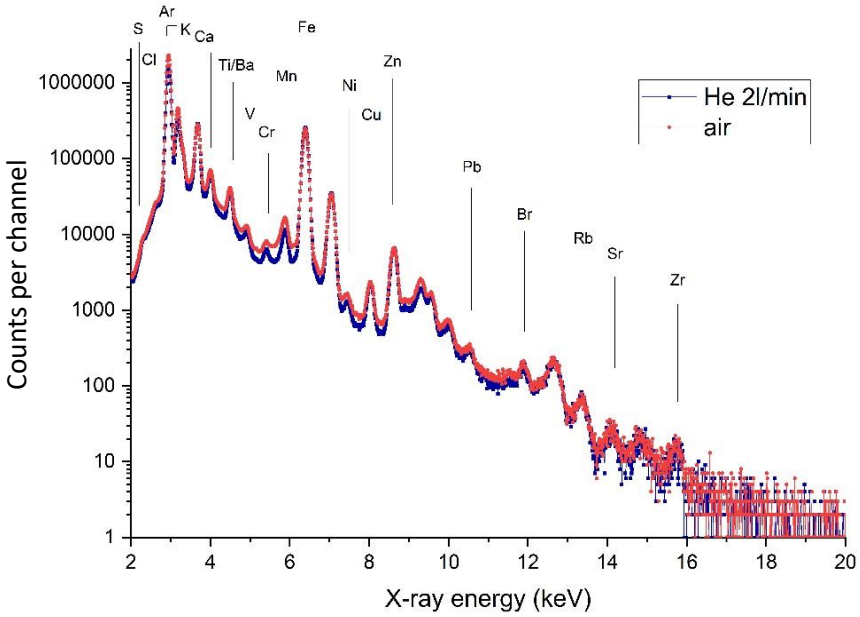

Figure 3.7 PIXE spectra recorded on NIST SRM2783 reference material by the 3-SDD cluster. The main characteristic X-ray lines are indicated.

The spectra were evaluated using the GUPIXWIN program code [131]. At first, the solid angle of detection was calculated from the geometry of the setup using the procedure described in [132]. This approximate value was used as H in GUPIXWIN which is described as the "product of the detector solid angle and the setup correction factor. In an ideal situation, H is equal to the solid angle (Ω) created by the detector in the measurement's geometry". Finally, H was refined by using a series of one-element thin foils (Ti, Zn, Ta, Fe, Ni) and reference materials, e.g., samples from earlier proficiency test exercises by the IAEA [133].

The results obtained for the NIST SRM2783 is presented in Table **3.1**. With both detectors all measured concentrations were within uncertainty to the certified/reference values.

Table 3.1. Elemental concentrations of NIST SRM2783 reference material measured by the UTW-SDD and the 3-SDD cluster. Certified and reference (indicated with*) values are presented in the left columns of the table. Uncertainty originating from the spectrum fitting (fit error) and detection limits (LOD) are also included. In case of Fe and Zn concentration values obtained for K and L lines are also given.

	Certified/reference*		**UTW SDD**			**3-SDD cluster**		
	conc.	**SD**	**Conc.**	**Fit error**	**LOD**	**Conc.**	**Fit error**	**LOD**
	(ng/cm²)	(ng/cm²)	(ng/cm²)	(%)	(ng/cm²)	(ng/cm²)	(%)	(ng/cm²)
Na	186.7	10.0	180	18.3	19.1			
Mg	865.5	52.2	870	1.4	10.9			
Al	2330.3	53.2	2400	0.6	9.9			
Si*	5883.5	160.6	5990	0.5	8.6			
P			100	6.7	10.6			
S*	105.4	26.1	110	4.2	9.3	170	32.6	24.5
Cl			10	13.7	9.4			20.5
K	530.1	52.2	540	1.6	11.1	580	2.3	6.1
Ca	1325.3	170.7	1300	0.9	8.7	1360	0.8	1.7
Ti	149.6	24.1	135	3.8	5.6	136	1.7	1.0
V	4.9	0.6				7	17.2	1.4
Cr	13.6	2.5	10	31.7	5.4	10	6.9	0.5
Mn	32.1	1.2	40	12.0	4.6	27	2.8	1.4
Fe	2660.6	160.6	2510	1.1	8.3	2650	0.4	0.6
Fe L			*2544*	*7.0*	*96.7*			
Co	0.8	0.1			28.3			5.8
Ni	6.8	1.2			8.2	9	7.1	0.5
Cu	40.6	4.2	40	18.6	8.5	35	2.0	0.5
Zn	179.7	13.1	175	8.7	6.4	177	0.9	0.6
Zn L			*195*	*20.5*	*33.5*			
Rb*	2.4	0.6				2	45.4	1.6
Sr								1.2
Zr						10	26.2	1.4
Ba	33.6	5.0				40	10.5	16.7
Pb	31.8	5.4				35	12.4	2.6

As it is shown on the spectrum of the UTW SDD X-ray lines with energies as low as 0.39 keV (N) can be detected. This means that an estimate can be given to the light element content of samples

(except carbon) with one short PIXE measurement. In addition, L lines of medium Z elements (e.g. Ti, Fe, Cu, Zn) can be evaluated which gives an extra information about the quality of the analysis. An example is given in Table **3.1**, when the results for Fe and Zn K and L lines show a very good match indicating that the parameters of the evaluation were correct.

3.1.2.1 Optimization of measurement parameters

When atmospheric aerosols are collected for elemental or chemical analysis, the most commonly used filtration and impaction media are PTFE (Poly Tetra Fluro Ethylene)/ Teflon filters, quartz fiber filters, nucleopore polycarbonate (PC) filters and Kapton foils. At ATOMKI, all these types of filters and impactor foils are used, and thus analyzed by PIXE.

When choosing the beam energy, several aspects had to be taken into consideration.

(1) Increasing the proton beam energy in PIXE studies leads to greater statistics of the X-ray lines due to increased X-ray production cross sections, but also increases the background beneath them.

(2) The gamma radiation from F in Teflon filters results increased background in the high energy part of the PIXE spectrum due to the Compton scattering of γ radiation in the detectors. It is advisable to choose such beam energies where the cross section of the ^{19}F (p, γ p') reaction has a minimum. Such proton energies are < 1.8 MeV, 2.2 MeV, 2.5 MeV, and 3.1 MeV [134].

(3) We have to keep the radiation level in the accelerator hall as low as possible.

(4) The detector crystal in the UTW detector have to be protected from scattered protons. The protection by the two 4 cm long Nd-Fe-B magnets works up to 3 MeV beam energy.

Due to these reasons, we found that 2.5 MeV beam energy (on the target) is the best for in-air PIXE measurements using this setup. The beam current was (10-70) nA. Higher currents (40-70) nA are used for polycarbonate and lower currents (15-25) nA for PTFE and quartz filters. Higher beam currents lead to sample damage and/or too high dead time.

Due to the limited availability of beam time, the time spent with one measurement should be also as short as possible while all the required information is gathered. Therefore, we set the measurements that way that the accumulated charge on all samples should be 10 μC. This provides enough information of a sample with very good sensitivity, as I'll show in the following.

3.1.2.2 Detection limits

Aerosol samples collected on Teflon/PTFE, quartz fibre, and nucleopore polycarbonate filters have been studied so far in the in-air millibeam. Table **3.2** summarizes the detection limits (LOD) calculated for the different filter types. Figure **3.9** shows a comparison of the LODs obtained on filter blanks of various substrates using a 2.5 MeV proton beam (energy on sample). In terms of LOD, the polycarbonate (PC) filter has a significantly lower background spectrum, and thus better LODs are obtained in compared with other substrates.

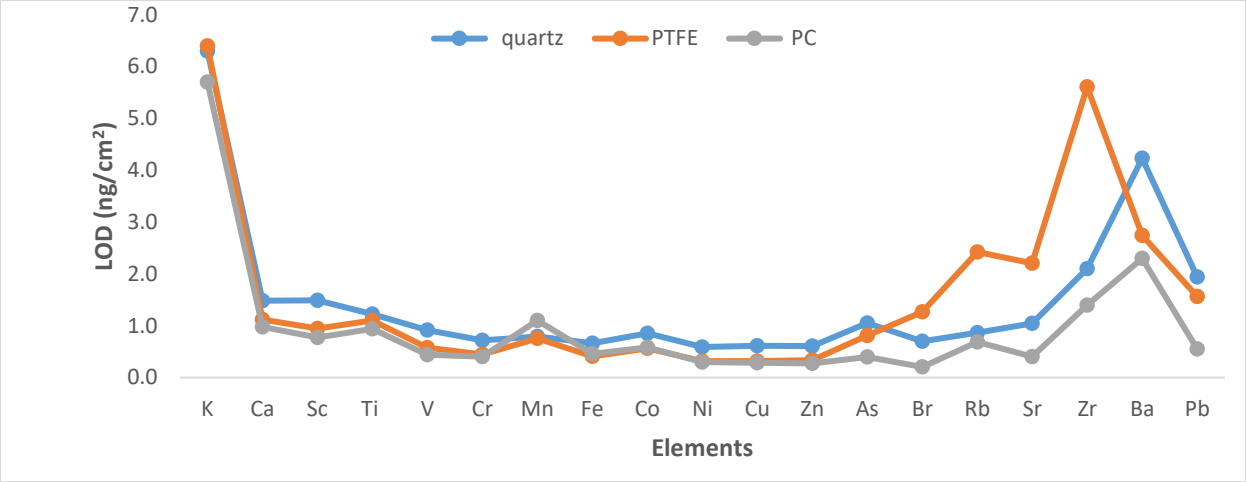

Figure 3.9 Comparison of the MDLs for the various elements detectable by PIXE measurements with 2.5 MeV energy (on target) proton beam on different sampling substrates.

The performance of the new set-up has been compared through LODs achieved on the 'old' in-vacuum PIXE setup [108]. The typical measurement conditions in the vacuum chamber were the following: 2 MeV H^+ beam, (30-50) nA current, 40 µC accumulated charge for polycarbonate, 20 µC accumulated charge on PTFE and quartz filters, detector: 50 mm^2 Si(Li) with 12 µm Be window and 24 µm mylar absorbent. In vacuum, an electron source was used to wave off the charging of the insulating samples. The beam current had to be reduced below 10 nA in the case of PTFE or quartz fiber filters because of the increased high-energy background caused by the Compton scattering of gamma radiation of F within the detector (PTFE) and sample charging (quartz). The right column in Table **3.2** contains LODs achieved on the "old" in-vacuum PIXE setup.

Table 3.2. Detection limits in ng/cm^2 determined for different filter blanks using SDD detectors of the new setup. Measurement conditions: 2.5 MeV H^+ beam, 10 μ C collected charge. The right column of the table contains LODs of the old in-vacuum PIXE setup as a comparison (conditions: 2 MeV H^+ beam, 20/40 μC accumulated charge).

		X-ray	UTW SDD			3-SDD cluster			*Si(Li)*		
	main X-ray line	energy (keV)	quartz	PTFE/ teflon	polycar bonate	quartz	PTFE/ teflon	polycar bonate	*quartz*	*PTFE/ teflon**	*polycar bonate*
			air	He	He	air	He	He	*In-vacuum*		
N	Kα	0.39		67	68.3						
O	Kα	0.525		1332	124						
F	Kα	0.68		721	30.9						
Na	Kα	1.04		35	9.1						
Mg	Kα	1.25		18	8.1						
Al	Kα	1.49		14.3	7.4					*12.7*	*15.6*
Si	Kα	1.74	1393	12.5	7					*5.8*	*6.7*
P	Kα	2.01	100	23	13.2					*4.4*	*4.9*
S	Kα	2.31	47.5	16	7.9	20.2	14.0	9.0	*98.0*	*3.0*	*3.3*
Cl	Kα	2.62	40.0	15.5	8.7	10.7	8.0	8.0	*25.5*	*2.5*	*2.7*
K	Kα	3.31	23.4	17.2	9.8	6.3	6.4	5.7	*7.7*	*1.6*	*1.8*
Ca	Kα	3.69	14.9	16.8	6.4	1.5	1.1	1.0	*9.9*	*1.2*	*1.4*
Ti	Kα	4.51	11.5	9	7.7	1.2	1.1	0.9	*4.6*	*1.7*	*1.0*
V	Kα	4.95	10.2	13	8.1	0.9	0.6	0.4	*6.6*	*1.6*	*0.9*
Cr	Kα	5.41	9.2	7.3	2.7	0.7	0.4	0.4	*3.5*	*0.9*	*0.7*
Mn	Kα	5.9	9.1	7.3	3.2	0.8	0.8	1.1	*3.4*	*1.0*	*0.7*
Fe	Kα	6.4	7.6	12.1	7.2	0.7	0.4	0.5	*3.2*	*1.1*	*0.5*
Co	Kα	6.93	8.6	16.8	5.1	0.9	0.6	0.6	*4.0*	*1.2*	*1.0*
Ni	Kα	7.47	6.3	18.1	9.4	0.6	0.3	0.3	*2.8*	*1.4*	*0.5*
Cu	Kα	8.04	7.1	26.4	5.9	0.6	0.3	0.3	*2.7*	*2.6*	*0.5*
Zn	Kα	8.63	6.9	30.3	12.3	0.6	0.3	0.3	*2.9*	*2.4*	*0.6*
As	Kα	10.51	16.2			1.1	0.8	0.4	*5.1*	*8.7*	*1.1*
Se	Kα	11.21	13.0			1.0	1.0	0.3	*2.6*	*8.4*	*2.3*
Br	Kα	11.91	19.4			0.7	1.3	0.2	*4.6*	*8.4*	*2.5*
Rb	Kα	13.38	35.1			0.9	2.4	0.7	*5.2*	*23.4*	*6.4*
Sr	Kα	14.14	51.6			1.0	2.2	0.4	*13.6*	*31.7*	*7.1*
Zr	Kα	15.75	100.0			2.1	5.6	1.4	*12.2*	*49.1*	*8.4*
Ba	Lα	4.46	43.0			4.2	2.7	2.3	*16.3*	*4.9*	*4.5*
Pb	Lα	10.54	32.0			1.9	1.6	0.6	*13.8*	*18.8*	*5.4*

* Beam energy: 1.8 MeV

The results show that we reached excellent detection limits with the new SDD detector cluster using 25-50 % of the irradiation dose compared to the in-vacuum system. The difference between the old in-vacuum setup and the new in-air setup is most spectacular in the case of quartz and PTFE filters, when LODs were improved by several factors. Thanks to the relatively smaller thickness of SDDs compared to Si(Li) detectors, the Compton background is reduced significantly resulting in improved LODs by factors of 5-15 for medium and high Z elements [135]. In the case of quartz and polycarbonate filters the higher beam energy, the increased solid angle and the reduction of sample charging might lead to better LODs of heavier elements. In addition, the range of analyzed elements has been significantly extended in the direction of low-Z.

3.1.2.3 Setting the optimal He flow

As I have shown in the previous paragraphs, helium (He) flow is applied in order to detect light elements. He is introduced to the system through a small tube directly into the collimator snout of the UTW SDD detector, as shown in Figure **3.10**. This way, the whole volume in front of the detector is filled with He. He flow is controlled through the pressure reducer valves with the help of a rotameter.

In order to determine the optimum He flow, a series of measurements on a 50-mm-thick Ni foil were carried out with varying the He flow rate from (0 to 4) l/min with 0.5 l/min steps. The area under the Ar and N peak and the ratio of Ni K_α (7.474 keV) and Ni L (0.849 keV) lines were observed with the changing He flux. The obtained spectra are presented in Figure **3.11a,** with interesting regions enlarged in Figures **3.11b** and **3.11c**. The counts under the peaks are shown in Figure **3.12**. He flow between 1.5 and 2.5 l/min proved to be optimal, as can be seen from the figures. At 1.5 l/min flow rate, the Ni K_α/L_α peak ratio reached the plateau, and at 2 l/min, the count under the Ar peak was minimum. Higher flow rates resulted in distortion of the PIXE spectra, as shown in Figure **3.11c**. The peaks widened, and a shift can also be observed in the high-energy region.

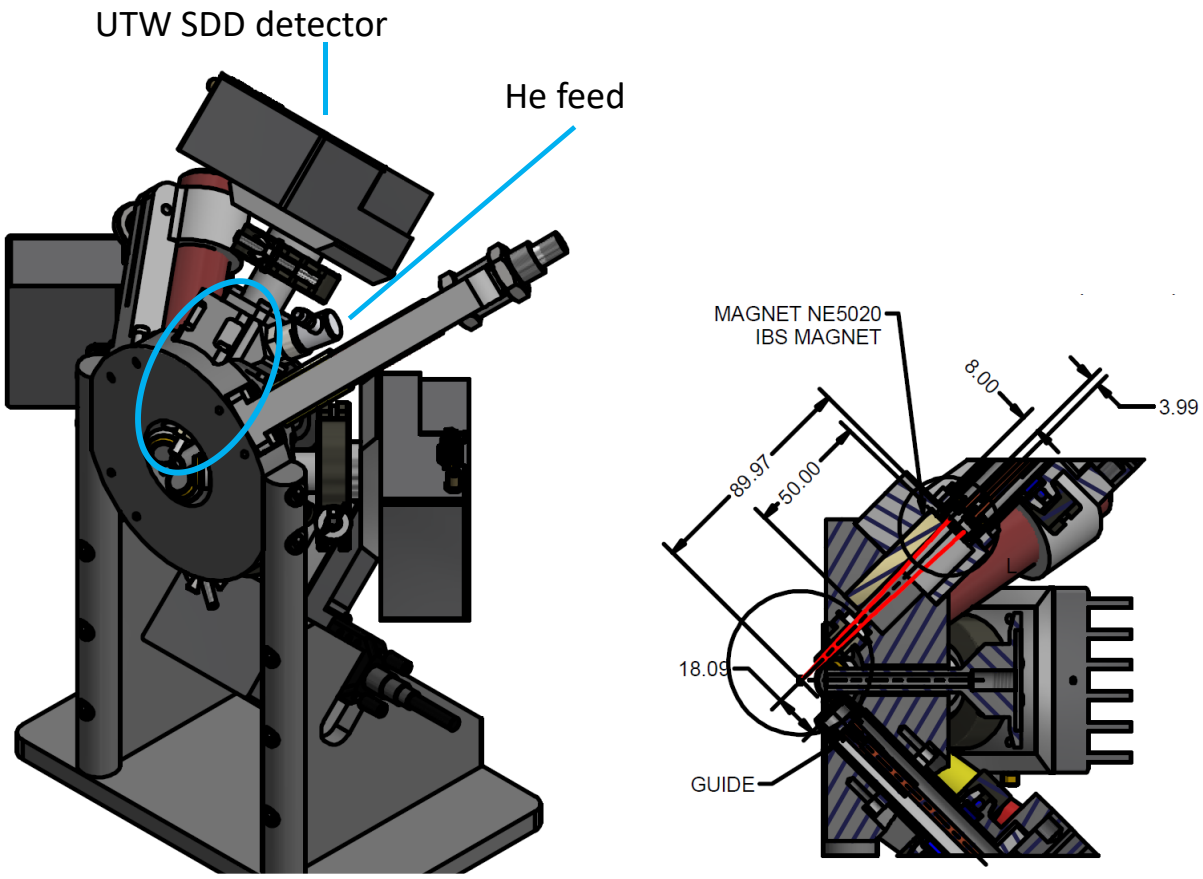

Figure 3.10 The layout of the 4-SDD detector system shows the He feed, and the cross-section image shows the structure of the UTW SDD detector mount with the collimator snout and the magnet.

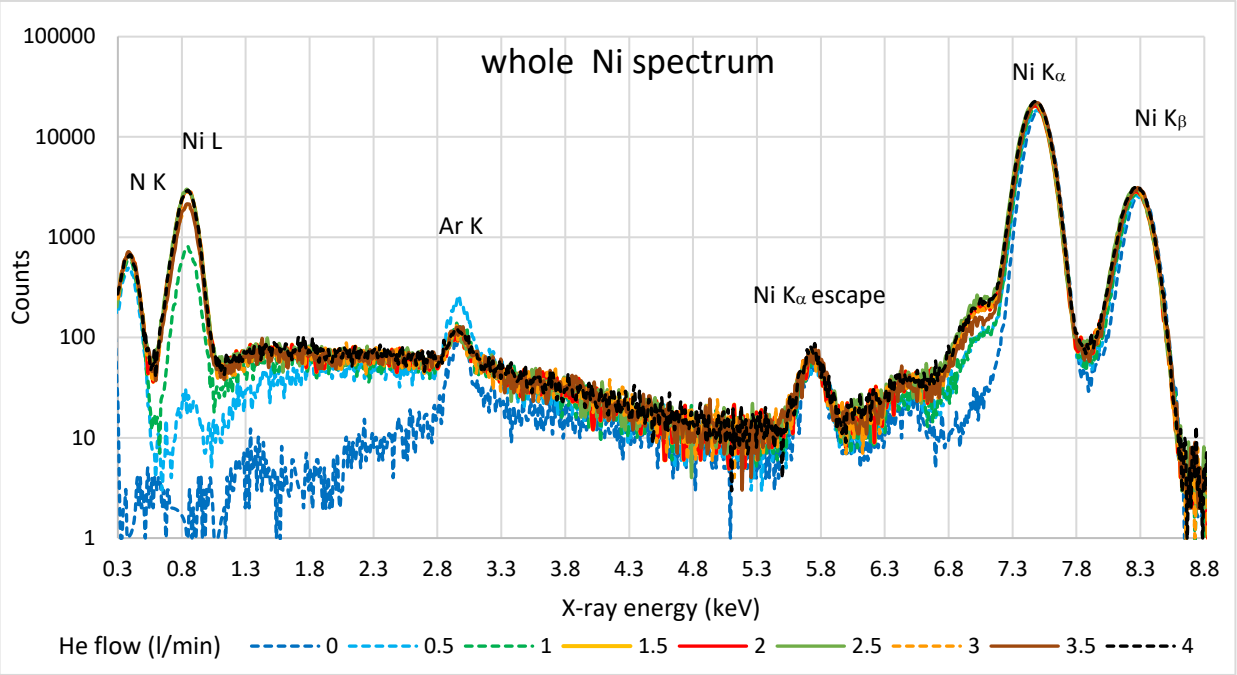

Figure 3.11a Spectrum of a 50 μm thick Ni foil in a He flow from 0 to 4 l/min

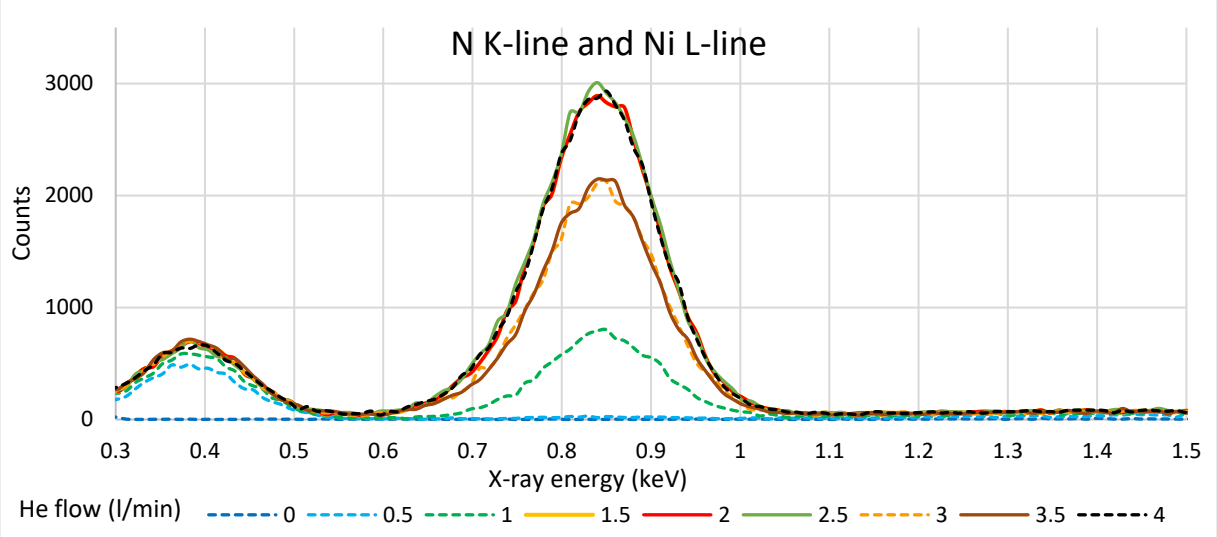

Figure 3.11b N K (0.375 keV) and Ni L (0.85 keV) X-ray lines in a He flow from 0 to 4 l/min.

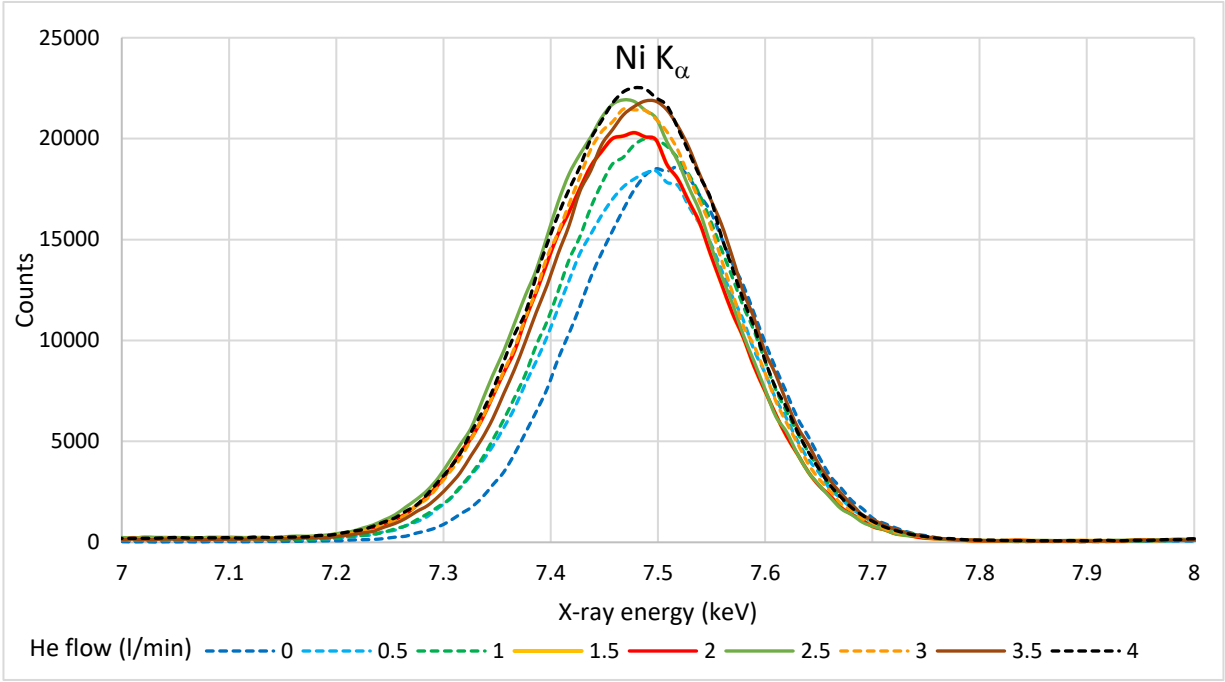

Figure 3.11c Ni Kα (7.46 keV) X-ray line in a He flow from 0 to 4 l/min.

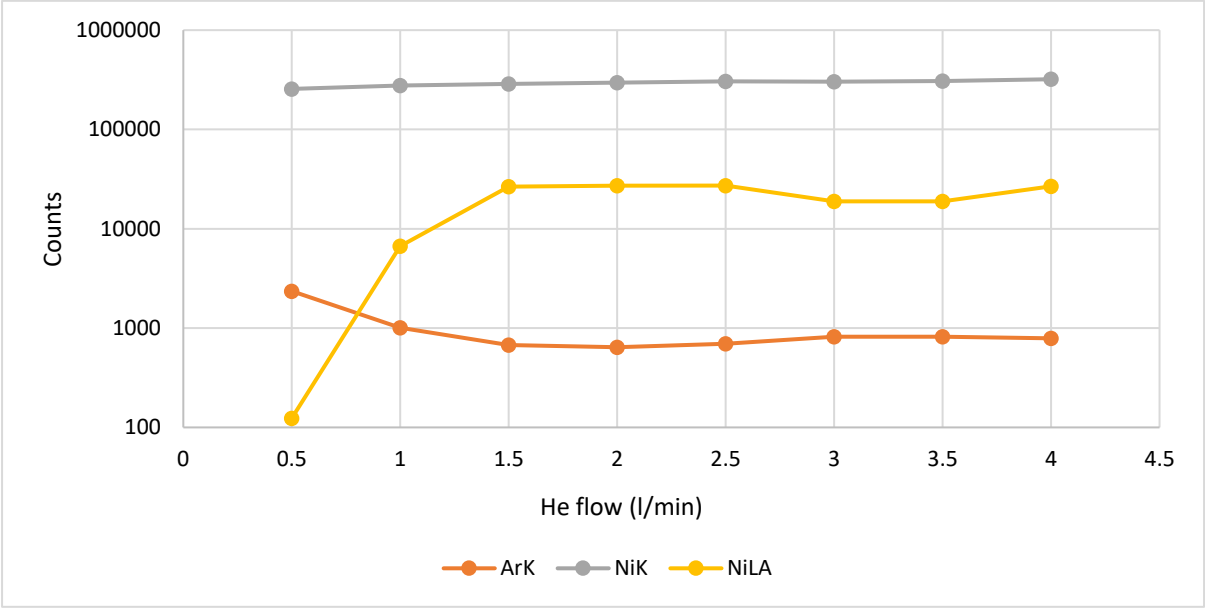

Figure 3.12 Counts under the Ni Kα, Ni L and Ar K peaks with different He flow.

3.1.2.4. The influence of Helium-saturation level

Normally, the saturation of the volume in front of the detector with He should be 100%. However, on the spectra of aerosol samples and filter blanks (Figure **3.6),** we see the presence of N. This can only originate from air between the sample and detector, which means that the level of saturation was not 100%. The origin of Ar is also the air in the laboratory; however, because aerosol samples are thin, most characteristic X-ray lines of Ar originate from the air behind the sample.

For PIXE analysis of the low Z elements, it is essential not only to maintain a high partial pressure of helium but also to maintain the helium-to-air ratio constant with high accuracy. Small changes in the helium concentration will have a large effect on the attenuation of soft X-rays. With the help of the GUPIXWIN program, calculations were made about how the level of He saturation influences the obtained concentration values.

Figure **3.13** demonstrated the influence of the He saturation level on the calculated elemental concentrations as a function of X-ray energy. At first, we calculated the elemental concentrations of an aerosol sample (NIST SRM2783) with He saturation levels set to 97.1%, 98.2%, and 99.3%. We named these values the "real" concentrations. Then, for the same sample, the saturation was changed to the optimal value of 99.9% within the GUPIXWIN, and the elemental concentrations were calculated again with nothing else changed. Finally, concentration ratios between the "real" concentration values and the values with 99.9% saturation were calculated. From the figure, one can see that overestimating the saturation can lead to a significant underestimation of the actual concentrations, especially in the low-energy X-ray region. The actual level of He saturation was 98.2% when measuring the spectrum, as shown in Figure **3.6**. The change in the calculated concentration induced by the presence of 1.7% air is increasing steeply with decreasing X-ray energy. The difference is twice in the case of Na (1.04 keV) and 11 times in the case of O (0.525 keV). For Si (1.74 keV), the change is only 16%, while for K (3.32 keV) and heavier elements, it has no effect. Even a few tenths of a percent change in the saturation level has a significant effect on the calculated concentration of light elements.

The change in the calculated concentration values of light elements as well as FeL and ZnL lines in an aerosol sample is presented in Figure **3.14** when the saturation level of He increased from

96% to 99.9% in the software. The concentration was set to 1 for each element at the 96% level. The modelled concentrations are decreasing exponentially with increasing saturation levels. The extent of change depends on the energy of X-ray lines, as demonstrated in Figure **3.13**. For very low-energy X-ray lines, the decrease is significant; it can reach 98–99%. This is the case for the O K_α (0.525 keV), Fe L_α (0.705 keV), or F K_α (0.677 keV) lines, while for the 2.62 keV K_α line of Cl, the effect is negligible.

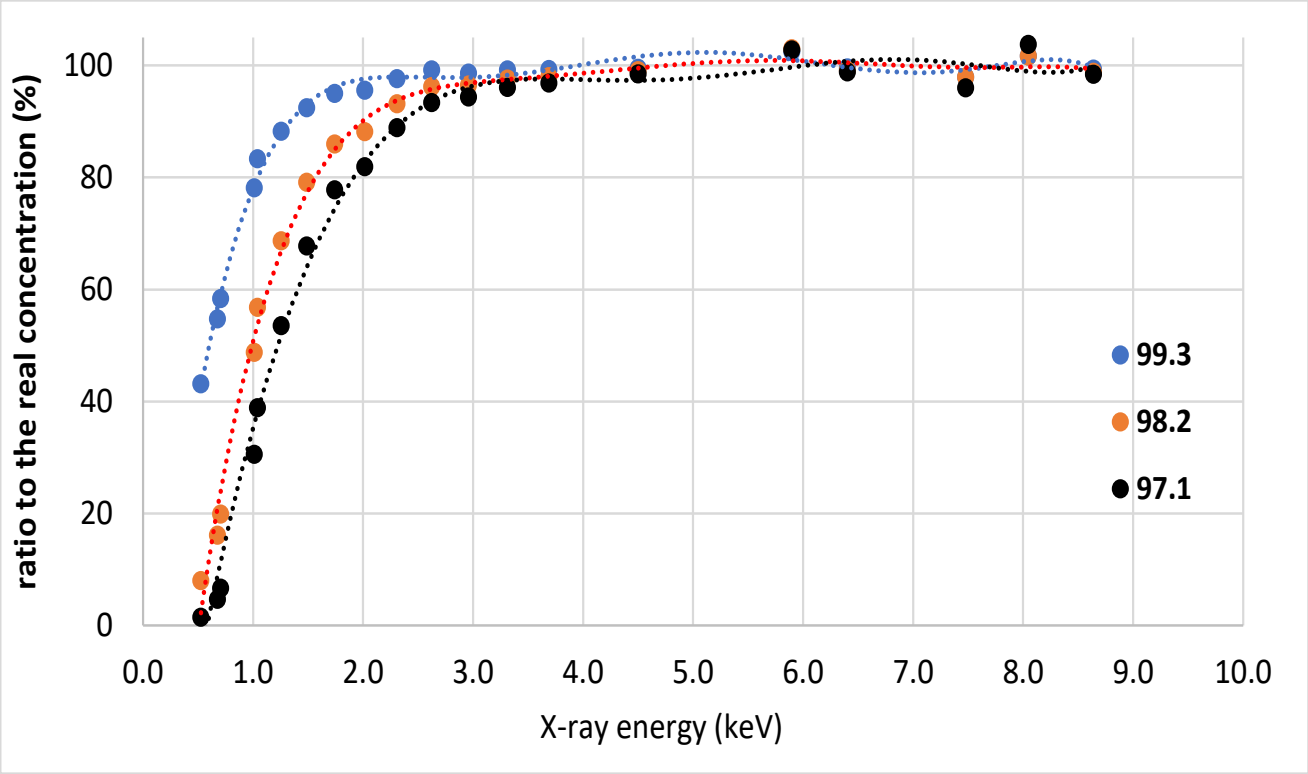

Figure 3.13 Difference in the obtained elemental concentration values for an aerosol sample when the He saturation level is given as 99.9% instead of the actual values of 97.1%, 98.2% and 99.3%.

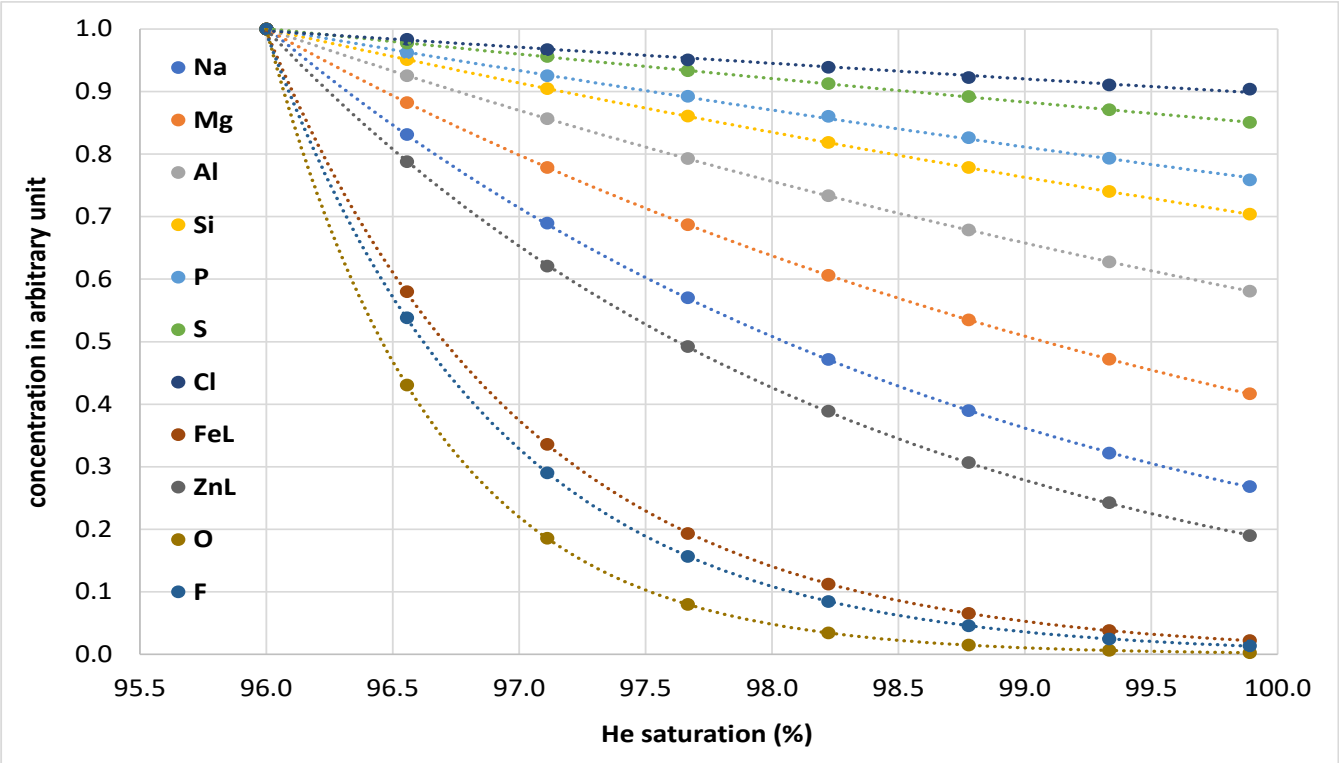

Figure 3.14 Change in concentrations of light elements and low-energy L lines when the saturation level given in the GUPIXWIN software increased from 96% to 99.9%. The concentrations of each element were set to 1 at the 96% level.

As shown above, it is essential to have a good estimate on the actual level of saturation because the presence of air, even in a very low amount, can alter the calculated concentrations of light elements by several factors.

Other IBA techniques, such as backscattering spectrometry (BS) and particle-induced gamma-ray emission (PIGE), can be used to obtain the correct concentrations of light elements such as Na, Mg, and Al. PIGE is particularly sensitive to these components and is widely used in IBA laboratories [135, 136]. However, because PIGE cross sections are substantially lower (by orders of magnitude) than PIXE cross sections, and PIGE sensitivity is beam energy dependent, higher beam energies, much longer measurement durations, or larger beam doses are frequently required. This is especially true for aerosol samples when concentrations are low and the quantities to be

analyzed are small. Using PIGE together with PIXE would result in a significant increase in measurement time as well as an increase in beam energy of at least 3 MeV.

Due to the reasons described earlier, we prefer the beam energy at 2.5 MeV. Fortunately, the PIXE spectrum itself provides the solution in our case. In the case of aerosol samples, the filter material itself has a very strong signal in the spectrum of the UTW detector. Fluorine is present in known quantities in PTFE filters, and oxygen in the spectrum of the polycarbonate filter samples originates predominantly from the filter material. When compared to the O content of the PC filters, the contribution of the particle deposit and (1-2) % air is insignificant. Because the concentrations of these components are known or easily calculated, they act as an 'inner standard' for estimating the level of saturation. The only unknown parameter for the spectrum evaluation is the mixing ratio of He and air. In the GUPIXWIN program the filter parameters (amount of air and He) have to be set in such a way that we get back the known concentration of the characteristic elements of the filters. It is a kind if iteration process done manually in several steps until the right concentration is obtained. In addition, low-energy L-lines (typically, Fe, Cu, and Zn) and the independent results of the 3-SDD cluster (or the actual other detectors(s)) function as a secondary control for the goodness of this approach.

We found that during our measurements, the saturation of He changed between 97% and 99.5%.

3.1.3 PIXE measurement of thick samples

Although the measurement setup is optimized for the elemental characterization of thin aerosol samples, the system is capable for the analysis of thick specimen like glasses or metals with good sensitivity and good efficiency. Because the current monitoring is not solved for thick targets the irradiation dose is estimated from the measurement time and the beam current before and after the measurement. The composition of the material is calculated by normalizing the measured concentrations to 100%. For this approach the knowledge of the matrix composition is essential, which means one must measure all main elemental components. As an example, results obtained for CorningA archeological reference glass [137] are presented. PIXE spectra recorded by the UTW SDD are shown on Figure **3.15**.

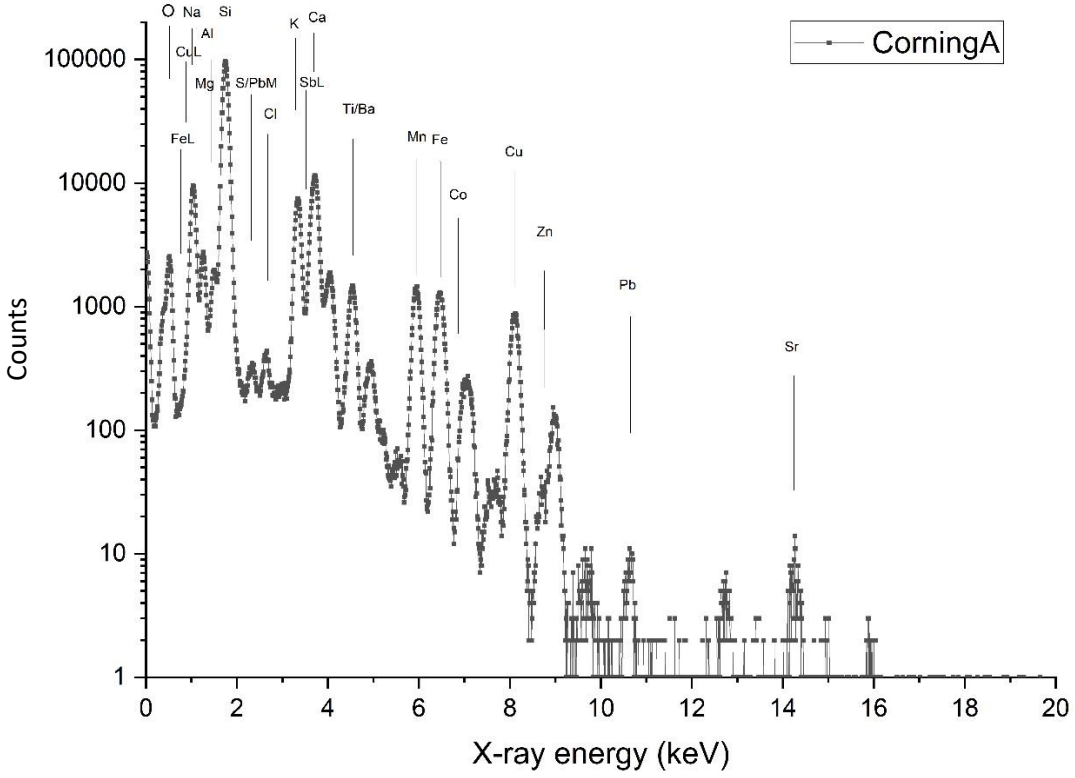

Figure 3.15 PIXE spectra recorded on CorningA reference glass by the UTW SDD. The main characteristic X-ray lines are indicated.

Spectra collected by the UTW detector were evaluated using the iterated matrix solution in which all measured elements were included independently. Measurement conditions were like that of the aerosol samples: 2.5 MeV H^+ beam, ~10 nA beam current, 2 (l/min) He flow. Spectra measured by the 3-SDD cluster were evaluated in the fixed matrix solution mode. Obtained results together with reference values are presented in Table **3.3**. For most elements the obtained concentrations were within uncertainties. In case of Sn and Sb the deviation from the reference value might originate from that only the L lines of these elements were detected. The energies of K lines were out of measurement range. In addition, the detection efficiency of the SDDs is very low for the energy region of 20 keV or higher, as was mentioned earlier. Therefore, in this case the application of a Si(Li) detector would have been justified.

Naturally, for glasses and most minerals the oxygen content of a sample can be estimated from the common oxide formulas, and therefore it is not strictly necessary to measure oxygen. However,

measuring directly the light element content gives an extra information about the operation of our system, and it can be used as a quality control of the measurement. On the other hand, there are samples with unknown N, O, F content when the capability of measuring low energy X-rays with (0.35 – 1) keV energies comes useful.

Table 3.3. Elemental concentrations in wt.% of CorningA reference glass material measured by the UTW-SDD and the 3-SDD cluster. Reference values are presented in the left columns of the table. Uncertainty originating from the spectrum fitting (fit error) and detection limits (LOD) are also included. In case of Fe and Zn concentration values obtained for K and L lines are also given.

	reference	**UTW SDD**			**3-SDD cluster**		
	conc. wt.%	**conc. wt.%**	**Fit err. %**	**LOD wt.%**	**conc. wt.%**	**Fit err. %**	**LOD wt.%**
O	44.7*	44.4	2.01	0.1711			
Na	10.60	10.4	0.35	0.0132			
Mg	1.596	1.53	0.69	0.0076			
Al	0.529	0.59	0.96	0.0079			
Si	31.061	31.4	0.09	0.0028			
P	0.035			0.0104			
S	0.056	0.072	4.53	0.0048			
Cl	0.090	0.097	3.01	0.0038	0.084	4.57	0.0016
K	2.381	2.430	0.29	0.0042	2.380	0.62	0.0007
Ca	3.593	3.517	0.23	0.0198	3.458	0.35	0.0088
Ti	0.474	0.511	0.81	0.0072	0.491	0.34	0.0035
V	0.003			0.0131	0.004	10.43	0.0036
Cr	0.002			0.0024	0.001	9.76	0.0003
Mn	0.775	0.774	0.63	0.0021	0.771	0.19	0.0003
Fe	0.763	0.734	0.71	0.0073	0.740	0.18	0.0028
Co	0.134	0.142	2.34	0.0056	0.142	0.3	0.0019
Ni	0.016	0.019	10.01	0.0026	0.014	1.41	0.0006
Cu	0.935	0.937	0.75	0.0011	0.948	0.16	0.0003
CuL		0.832	3.52	0.1621			
Zn	0.035	0.031	8.63	0.0034	0.036	0.71	0.0004
Rb	0.008			0.0096	0.013	4.32	0.0009
Sr	0.085	0.084	12.31	0.0078	0.075	1.3	0.0014
Sn	0.150						0.0225
Sb	1.276	1.131	2.91	0.3056	1.408	1.03	0.1994
Ba	0.412	0.380	3.05	0.0832	0.439	0.43	0.0514
Pb	0.067	0.078	9.65	0.0071	0.065	4.93	0.0067
Pb M		0.070	20.97	0.0288			

*reference O concentration value was calculated from the common oxide forms of elements

3.2 Characterization of urban aerosol pollution before and during the COVID-19 crisis in Debrecen

The COVID-19 virus swiftly spread over the world, beginning in Wuhan, the capital of China's Hubei province, and was declared a pandemic by the World Health Organization in early 2020. In December 2019, the virus spread to Europe, with the first cases being verified on January 24, 2020, in France. By the end of March 2020, all countries in Europe had confirmed cases.

Many countries around the world were forced to impose severe restrictions on their populations as a result of the virus's spread, including temporary suspensions of travel, non-essential activities for citizens, and social aggregation in order to reduce physical contact between people and thus the spread of the virus's acute respiratory disease (COVID-19).

Aside from the desired outcome of containing the pandemic by lowering the infection curve [138], the lockdowns had a side effect that was beneficial to the population's health in all of the cities around the world that adopted the lockdown policy. Basically, there was a time when there was essentially no traffic in and outside the cities. Industrial activities were also reduced significantly. As a result, the emission of many atmospheric pollutants was reduced, and the air quality gradually improved. This valuable occasion allowed us to investigate how air pollutants, including airborne particulate matter respond to a rapid reduction in anthropogenic emissions.
There are a number of studies available that deal with the influence of lockdown on air pollution and accompanying meteorological conditions. They revealed that there has been a considerable reduction in atmospheric pollutants and an improvement in air quality compared to the pre-lockdown period [139]. According to Menut et al., NO_2 concentrations have decreased by 30% to 50% in all Western European countries [140]. In the United States, the decrease in NO_2 level was 25.5%, by 4.8 ppb on average. In the meantime, $PM_{2.5}$ levels dropped by 11.3% [141]. Brazil had the highest reduction in NO_2 concentrations, at 54.3%, while the concentration of O_3 increased by 30% [142].

Similar tendencies were detected at traffic sites in Budapest, Hungary, for the first lockdown period in spring 2020 [143, 144]. However, during the first lockdown, the reduction in air pollution was not observable in Budapest's suburban areas or other cities. Furthermore, in the majority of cities,

PM_{10} concentrations showed no decline at all. The absence of a decrease in PM concentration was explained by meteorological conditions.

More recently, a limited number of studies have been available on the composition and sources of PM pollution during the COVID-19 lockdown [145, 149], but only a few are related to middle Europe [150, 151] and none to Hungary. Furthermore, the majority of these work reports are the outcome of the first lockdown period in early 2020. These investigations reveal a large drop in the concentration of traffic-related components and source contributions, but secondary aerosol behavior is variable. [152]

In Hungary, the first cases were announced on March 4, 2020, and the first coronavirus-related death was reported on March 15th. The government reported on March 18, 2020, that the virus has spread to every region of the country. Various epidemiological measures were implemented, including diagnostic testing, contact management, etc. Throughout the next two years, varying degrees of restrictions were periodically implemented based on how the epidemiological situation changed.

In Hungary, the COVID-19-affected period lasted from early 2020 to March 2022. There were four lockdowns and two relaxation periods during this time, as illustrated in Table **3.4**. The four lockdowns corresponded to the four COVID waves. We divided the two years of pandemic into ten periods: the four lockdowns that linked with springs (LD1 and LD3) and winters (LD2 and LD4), the summers of the relaxation periods (Relax 1 and 2), the first two months of autumn, which belonged to the relaxation too (Relax 1 and 2), and the Novembers, which were transition time into lockdowns and also to winters (Pre-LD2, Pre-LD4). September and October were treated separately from the summer months because of the different activities in the population; this is the time of year when work and school resume after the summer holidays. The heating season starts in November, and high pollution levels frequently occur throughout this month due to increasing pollutant emissions and unfavorable climatic conditions, such as temperature inversions.

To characterize a lockdown period, we used the stringency index developed by the OxCGRT project [153]. It is a complex measure comprised of nine variables, including school and workplace closures, public event cancellations, limitations on public gatherings, stay-at-home regulations, restrictions on internal movements and travel abroad, and so on. Data were gathered from the web

resource (Our World in Data) [154]. The stringency index was quite comparable in the first three lockdown periods, but there were variances in the measures.

A change in mobility accurately describes how people's lifestyles have changed as a result of closures and restrictions [155, 156]. During lockdowns, the mobility of individuals in residential areas increased by around 10%, whereas it decreased by 20%–40% in recreation areas, transport stations, and workplaces. The biggest shift occurred during the first lockdown, while the lowest occurred during the last one. During relaxation periods, mobility was close to baseline values; however, increased activity was seen in parks, shops, and recreational facilities, particularly in the second year of the pandemic. The Data about mobility was obtained from [157].

In addition to the characteristics of the lockdown and relaxation periods, weather conditions affecting air pollution are presented in Table **3.5**, and the corresponding baseline values (pre-COVID) from years 2018–19 are in Table **3.6**. Meteorological parameters for Debrecen available in the archives of the Hungarian Meteorological Service were used [158]. Planetary boundary layer heights (PBLH) were collected from the Copernicus Climate Data Store [159], using the ERA5 reanalysis dataset [160]. Considering the whole 2-year period of the pandemic, the weather conditions were quite comparable to the prior two years. The variations between the investigated seasons and other times will be discussed alongside the findings

Table 3.4 Stringency index and mobility change during the COVID-19 pandemic (2020–2022) compared to baseline (2018–2019).

	Whole COVID	SPRING		SUMMER		SEP/OCT		NOV		WINTER	
		LD1	LD3	Relax 1	Relax2	Relax1	Relax2	Pre-LD2	Pre-LD4	LD2	LD4
Start date	1-3-2020	11-3-2020	8-3-2021	1-6-2020	1-6-2021	1-9-2020	1-9-2021	1-11-2020	1-11-2021	1-12-2020	11-12-2021
End date	28-2-2022	31-5-2020	17-5-2021	31-8-2020	13-8-2021	31-10-2020	31-10-2021	30-11-2020	30-11-2021	8-3-2021	6-3-2022
Stringency index		71.8	72.6	54.6	33.9	42.3	28.3	66.2	29.9	72.4	49.4
Mobility change (%)											
Retail, recreation	-8.9	-38.0	-20.8	0.6	15.8	-4.7	16.4	-23.8	6.1	-33.5	1.2
Grocery, pharmacy	5.9	-15.0	2.9	0.0	22.3	1.2	23.4	-2.7	21.3	-4.1	17.2
Residential	5.7	13.2	7.8	2.7	0.3	2.1	0.5	8.0	4.2	10.2	6.2
Transit stations	-17.4	-40.9	-23.9	-15.6	-0.2	-10.7	5.4	-26.0	-5.9	-33.6	-12.7
Parks	43.0	1.8	33.3	86.5	120.7	45.0	72.6	1.4	26.1	-3.2	18.1
Work-places	-19.8	-34.0	-22.0	-21.7	-15.5	-15.0	-9.2	-20.8	-11.8	-25.7	-13.9

Table 3.5 Meteorological parameters during the 10 investigated periods of the COVID-19 pandemic (March 2020– February 2022)

	COVID	SPRING		SUMMER		SEP/OCT		NOV		WINTER	
		LD1	LD3	Relax 1	Relax2	Relax1	Relax2	Pre-LD2	Pre-LD4	LD2	LD4
Start date	1-3-2020	11-3-2020	8-3-2021	1-6-2020	1-6-2021	1-9-2020	1-9-2021	1-11-2020	1-11-2021	1-12-2020	11-12-2021
End date	28-2-2022	31-5-2020	17-5-2021	31-8-2020	13-8-2021	31-10-2020	31-10-2021	30-11-2020	30-11-2021	8-3-2021	6-3-2022
Precipitation Monthly avg. (mm)	37.3	28.2	35.0	82.8	25.7	56.1	14.7	15.6	41.5	40.7	19.6
Temperature Daily avg. (ºC)	11.4	10.9	9.5	21.5	22.8	15.2	13.2	5.0	5.3	2.6	1.4
Air Pressure Daily avg. (hPa)	1003.9	1004.3	1003.4	1000.3	1001.4	1003.0	1007.8	1014.4	1004.7	1003.3	1005.0
Rel. Humidity Daily avg. (%)	73.4	57.7	66.7	71.8	62.1	77.5	69.6	92.4	88.1	87.6	83.4
Wind Speed Daily avg. (m/s)	3	3.7	3.5	2.8	2.9	2.8	2.5	1.8	2.3	2.9	3.5
WS < 1m/s No. of days monthly avg		1	1	1	0	2	3	7	3	7	4
PBLH daily avg. (m)	682	784	756	997	973	805	698	468	398	376	347
PBLH < 50 m No. of hours monthly avg								126	172	104	140

Table 3.6 Meteorological parameters corresponding to the pre-COVID period (March 2018– February 2020) were used as baseline values.

	March 2018 – February 2020	SPRING	SUMMER	SEP/OCT	NOV	WINTER
Precipitation Monthly avg. (mm)	35.3	43.4	36.9	19.3	55.7	29.0
Temperature Daily avg. (ºC)	12.4	12.5	22.6	15.3	8.2	1.4
Air Pressure Daily avg. (hPa)	1003.6	1000.8	1001.6	1006.1	1004.5	1006.5
Rel. Humidity Daily avg. (%)	73.3	66.8	67.1	67.8	84.5	85.9
Wind Speed Daily avg. (m/s)	3	3.5	2.8	2.5	2.7	3.1
WS < 1m/s No. of days monthly avg		1	0	5	1.5	6
PBLH daily avg (m)	726	767	1010	853	488	399
PBLH < 50 m No. of hours monthly avg					70	85

3.2.1 The evolution of air pollutants in Debrecen

In addition to the results obtained from elemental composition through the PIXE technique, the variation in the concentrations of air pollutants measured at the 3 fixed monitoring stations of the Hungarian Air Quality Monitoring Network in the city of Debrecen before and during the national lockdown was also studied. The locations of the stations are indicated in Figure **2.7**. These stations provide hourly and daily mean concentrations of air pollutants such as O_3, CO, PM_{10}, NO, NO_2, SO_2, etc. In this work, daily concentrations of NO_2, CO, NO_x, and PM_{10} were used as complementary data to our work because concentrations of these components were available at all stations without larger gaps in the data series.

The average concentrations of CO, NO_2, NOx, and PM_{10} measured at the three AQ monitoring stations in Debrecen, as well as the averages of PM_{10}, $PM_{2.5}$, and PM_{coarse} at ATOMKI are presented in Tables **3.7, 3.8, 3.9**, and **3.10** for the 4-year-long (pre- and COVID) periods and broken down to the above-described lockdowns and relaxation periods, too.

The traffic site had the largest amount of all pollutants. The greatest difference was noted for NO_x when compared to the background stations; its concentration was 50%–60% lower at the background sites than at the traffic sites. The difference in average concentrations was over 40% for NO_2, but less than 10% for CO and PM_{10}. This difference between the traffic and background sites decreased during the epidemic, indicating a reduction in traffic emissions and a shift in mobility towards residential areas. The highest amounts of all pollutants were observed during the heating season (November–April), indicating that residential heating is a further major factor in air pollution in Debrecen. NO_x/CO ratios can provide an approximate assessment of the relative contribution of traffic and biomass burning at a site because the ratios differ significantly for the two emission types: the traffic emission ratio is much higher than the biomass burning emission ratio [161].

Table 3.7 Mean concentrations of NO_2, CO, NO_x, PM_{10} and NO_x/CO ratios in µg/m^3 at the **Hajnal utca - TRAFFIC** AQ monitoring site in Debrecen for the 10 studied periods of the COVID-19 pandemic, as well as the corresponding baseline values (pre-COVID) from 2018-19.

	SPRING		EX*	SUMMER		EX*	SEP/OCT		EX*	NOV		EX*	WINTER		EX*
NO_2	2018	35.3		2018	31.2		2018	40.5		2018	38.3		18/19	41	
	2019	37.8		2019	36.2		2019	50.1		2019	38.6		19/20	34.1	
	LD 1	25.9		relax1	22.7		Relax1	30.5		pre-LD2	28.1		LD2	28.2	
	LD3	24.4		relax2	23		Relax2	32.4		pre-LD4	30.5		LD4	29	
CO	2018	481.9		2018	479.3		2018	598.1		2018	662.4		18/19	774.6	
	2019			2019	399.5		2019	584.5		2019	650.5		19/20	585.2	
	LD 1			relax1	396.7		Relax1	479.8		pre-LD2	526.6		LD2	596.7	
	LD3	561.5		relax2	434.9		Relax2	565.8		pre-LD4	634.5		LD4	668.3	
NO_X	2018	59.7		2018	39.9		2018	78.8		2018	86.9		18/19	94.4	
	2019	60.6		2019	47.1		2019	102.4		2019	96.5		19/20	80.7	
	LD 1	53.4		Relax1	40.2		Relax1	72.3		pre-LD2	69.3		LD2	64.6	
	LD3	46.4		Relax2	37.7		Relax2	78.8		pre-LD4	93.5		LD4	69.6	
PM_{10}	2018	27.9	9	2018	20		2018	30.2	7	2018	38.3	10	18/19	32.1	8
	2019	22.3	5	2019	22.7		2019	34.2	6	2019	25.3		19/20	26.9	6
	LD 1	23.8	5	Relax1	18.8		Relax1	25.7	2	pre-LD2	23.9		LD2	23.3	2
	LD3	17.3	0	Relax2	18.7		Relax2	24.8	5	pre-LD4	33.8	7	LD4	23.2	2
NO_x/CO	2018	0.124		2018	0.083		2018	0.132		2018	0.131		18/19	0.122	
	2019			2019	0.118		2019	0.175		2019	0.148		19/20	0.138	
	LD 1			Relax1	0.101		Relax1	0.151		pre-LD2	0.132		LD2	0.108	
	LD3	0.082		Relax2	0.087		Relax2	0.139		pre-LD4	0.147		LD4	0.104	

EX*: no of exceedances

Where LD 1 denotes the first lockdown period, from March to May 2020,
LD 2 denotes the second lockdown period, from December 2020 to February 2021.
LD 3 denotes the third lockdown period, from March to May 2021.
LD 4 denotes the second lockdown period, from December 2021 to February 2022.
Relax 1 denotes June-August 2020 and September-October 2020.
Relax 2 denotes June–August 2021 and September–October 2021.
Pre-LD2 denotes November 2020; pre-LD4 denotes November 2021.

Table 3.8 Mean concentrations of NO_2, CO, NO_x, PM_{10} and NO_x/CO ratios in µg/m^3 at the **Kalotaszeg tér – urban background (UB)** AQ monitoring site in Debrecen for the 10 studied periods of the COVID-19 pandemic, as well as the corresponding baseline values (pre-COVI) from 2018-19.

	SPRING		EX*	SUMMER		EX*	SEP/OCT		EX*	NOV		EX*	WINTER		EX*
NO_2	2018	20.4		2018	15		2018	24.4		2018	28.2		18/19	26.4	
	2019	18		2019	13.7		2019	23.2		2019	22.6		19/20	21	
	LD 1	16.9		relax1	11.5		relax1	17.6		pre-LD2	19.6		LD2	20.2	
	LD3	13.3		relax2	10.6		relax2	23.4		pre-LD4	23.7		LD4	17.5	
CO	2018	292.4		2018	310.3		2018	486.2		2018	659.7		18/19	631.4	
	2019	366.6		2019	352		2019	415		2019	448.9		19/20	545.7	
	LD 1	405.5		Relax1	310.1		Relax1	443.9		pre-LD2	520.9		LD2	587	
	LD3	464.7		Relax2	229.1		Relax2	596.2		pre-LD4	760.7		LD4	679.1	
NO_X	2018	27.2		2018	18.7		2018	36.4		2018	50.7		18/19	44.4	
	2019	25.7		2019	18.5		2019	37.9		2019	41.3		19/20	35.4	
	LD 1	24.7		Relax1	15.4		Relax1	29.6		pre-LD2	32.7		LD2	32.5	
	LD3	18.2		Relax2	18.2		Relax2	48.7		pre-LD4	57.1		LD4	31.8	
PM_{10}	2018	24.4	3	2018	18.6		2018	22.4	3	2018	37	9	18/19	32.6	11
	2019	23.1	3	2019	21.2		2019	31.6	11	2019	26.2	2	19/20	25.3	6
	LD 1	25.6	4	Relax1	16.3		Relax1	19.3		pre-LD2	21.1		LD2	22.1	4
	LD3	16.1	3	Relax2	20.9		Relax2	24.2	6	pre-LD4	27.5	4	LD4	18.9	3
NO_x/CO	2018	0.093		2018	0.06		2018	0.075		2018	0.077		18/19	0.07	
	2019	0.07		2019	0.052		2019	0.091		2019	0.092		19/20	0.065	
	LD 1	0.061		Relax1	0.05		Relax1	0.067		pre-LD2	0.063		LD2	0.055	
	LD3	0.039		Relax2	0.079		Relax2	0.082		pre-LD4	0.075		LD4	0.047	

EX*: no of exceedances

Where LD 1 denotes the first lockdown period, from March to May 2020,
LD 2 denotes the second lockdown period, from December 2020 to February 2021.
LD 3 denotes the third lockdown period, from March to May 2021.
LD 4 denotes the second lockdown period, from December 2021 to February 2022.
Relax 1 denotes June-August 2020 and September-October 2020.
Relax 2 denotes June–August 2021 and September–October 2021.
Pre-LD2 denotes November 2020; pre-LD4 denotes November 2021.

Table 3.9 Mean concentrations of NO_2, CO, NO_x, PM_{10} and NO_x/CO ratios in µg/m^3 at the **Klinika – suburban background (SUB)** AQ monitoring site in Debrecen for the 10 studied periods of the COVID-19 pandemic, as well as the corresponding baseline values (pre-COVI) from 2018-19.

	SPRING		EX*	SUMMER		EX*	SEP/OCT		EX*	NOV		EX*	WINTER		EX*
NO_2	2018	21.4		2018	14.3		2018	33.5		2018	25.6		18/19	33.1	
	2019	11		2019	14.2		2019	35.1		2019	30.4		19/20	29.3	
	LD 1	21.8		Relax1	17.2		Relax1	26.9		pre-LD2	25.7		LD2	27	
	LD3	20.5		Relax2	19.7		Relax2	32.2		pre-LD4	37		LD4	2.3	
CO	2018	317.7		2018	299.1		2018	509.6		2018	395.4		18/19	445.9	
	2019	273.1		2019	376.4		2019	427.1		2019	502.5		19/20		
	LD 1			Relax1	282.9		Relax1	481.5		pre-LD2	530.9		LD2	552.7	
	LD3	326.8		Relax2	308.8		Relax2	465.7		pre-LD4	725.9		LD4	607.6	
NO_X	2018	24.5		2018	17.1		2018	41.3		2018	33.5		18/19	42.1	
	2019	14.4		2019	17.1		2019	44.5		2019	40.2		19/20	40.8	
	LD 1	25.6		Relax1	19.9		Relax1	34.4		pre-LD2	31.5		LD2	32.5	
	LD3	24		Relax2	21.9		Relax2	40.6		pre-LD4	55.8		LD4	9.4	
PM_{10}	2018	22.8	6	2018	17.9		2018	22.4		2018	27.3	4	18/19	28.1	7
	2019	21	4	2019	20.8		2019	27.4		2019	21.6		19/20	26.4	5
	LD 1	21.7	3	Relax1	16.8		Relax1	19.6		pre-LD2	21.5		LD2	22.8	4
	LD3	16.1		Relax2	18.1		Relax2	21.3		pre-LD4	21.9	1	LD4	15.5	
NO_x/CO	2018	0.077		2018	0.057		2018	0.081		2018	0.085		18/19	0.094	
	2019	0.053		2019	0.045		2019	0.104		2019	0.08		19/20		
	LD 1			Relax1	0.07		relax1	0.071		pre-LD2	0.059		LD2	0.059	
	LD3	0.073		Relax2	0.071		relax2	0.087		pre-LD4	0.077		LD4	0.016	

EX*: no of exceedances

Where LD 1 denotes the first lockdown period, from March to May 2020,
LD 2 denotes the second lockdown period, from December 2020 to February 2021.
LD 3 denotes the third lockdown period, from March to May 2021.
LD 4 denotes the second lockdown period, from December 2021 to February 2022.
Relax 1 denotes June-August 2020 and September-October 2020.
Relax 2 denotes June–August 2021 and September–October 2021.
Pre-LD2 denotes November 2020; pre-LD4 denotes November 2021.

Table 3.10 Mean concentrations of PM_{coarse}, $PM_{2.5}$, and PM10 in µg/m^3, and $PM_{2.5}/PM_{10}$ ratios for pre-COVID and during-COVID were measured at the urban background site in ATOMKI.

	SPRING		SUMMER		SEP/OCT		NOV		WINTER	
PM_{Coarse}	2018	12.8	2018	6.6	2018	12.5	2018	5.9	18/19	6.8
	2019	11.2	2019	9.3	2019	8.6	2019	4.1	19/20	4.4
	LD 1	12.3	Relax1	6.1	Relax1	6.9	pre-LD2	3.2	LD2	4.9
	LD3	5.9	Relax2	6.7	Relax2	7.1	pre-LD4	5.2	LD4	4.0
$PM_{2.5}$	2018	12.1	2018	7.9	2018	11.5	2018	12.0	18/19	14.4
	2019	8.9	2019	10.0	2019	8.4	2019	7.7	19/20	10.4
	LD 1	8.8	Relax1	7.7	Relax1	5.9	pre-LD2	7.5	LD2	11.2
	LD3	7.0	Relax2	7.0	Relax2	8.0	pre-LD4	11.6	LD4	9.5
PM_{10}	2018	24.9	2018	14.4	2018	24.0	2018	17.9	18/19	21.2
	2019	20.1	2019	19.3	2019	17.0	2019	11.8	19/20	14.8
	LD 1	21.1	Relax1	13.9	Relax1	12.8	pre-LD2	10.6	LD2	16.1
	LD3	12.9	Relax2	13.7	Relax2	15.2	pre-LD4	16.8	LD4	13.5
$PM_{2.5}/PM_{10}$	2018	0.486	2018	0.545	2018	0.479	2018	0.670	18/19	0.678
	2019	0.442	2019	0.519	2019	0.495	2019	0.651	19/20	0.703
	LD 1	0.417	Relax1	0.558	Relax1	0.462	pre-LD2	0.702	LD2	0.697
	LD3	0.541	Relax2	0.512	Relax2	0.530	pre-LD4	0.689	LD4	0.703

Where LD 1 denotes the first lockdown period, from March to May 2020,
LD 2 denotes the second lockdown period, from December 2020 to February 2021.
LD 3 denotes the third lockdown period, from March to May 2021.
LD 4 denotes the second lockdown period, from December 2021 to February 2022.
Relax 1 denotes June-August 2020 and September-October 2020.
Relax 2 denotes June–August 2021 and September–October 2021.
Pre-LD2 denotes November 2020; pre-LD4 denotes November 2021.

Pollutant concentrations decreased by 20% on average across all sites over the pandemic's two years. The concentration of CO, on the other hand, remained the same or even increased at the Klinika site. This suburban monitoring station is located on the inside of the county hospital's clinic campus. This site was obviously busier than usual throughout the epidemic; therefore, we did not expect a major reduction in air pollution here. Indeed, as the number of new COVID cases increased, so did the concentration of traffic-related gaseous pollution.

Pollutant reduction was at its maximum during lockdowns (20%–30% on average). Concentrations remained 10%–20% lower than the baseline during the relaxation periods. During the lockdowns, the NO_x/CO ratios changed significantly, indicating that biomass burning contributed significantly more than traffic emissions. Since the relaxation periods were in the summer, when heating was negligible, this ratio had no particular significance for those times.

The yearly average concentrations for all pollutants and all sites were well below the EU limit values set in Directive 2008/50/EC (40 $\mu g/m^3$ for PM_{10} and NO_2, 70 $\mu g/m^3$ for NO_x, and 3000 $\mu g/m^3$ for CO) [162]. Only PM_{10} exceeded daily (24-hour) limit values. In the two years prior to the pandemic, exceedance was 51, 48, and 26 in traffic, UB and SUB sites, respectively. During the pandemic, the values were 23, 24, and 8, indicating a decrease of at least 50%. Most of the excesses happened in November and the winter months.

Typically, lower PM_{10} concentrations have been identified at the ATOMKI UB site; nonetheless, PM_{10} data from all stations correlated strongly with one another. The deviation can be explained by the different methodologies, namely standard gravimetry of filter samples vs. automatic station data. This phenomenon is explained in depth in [163].

The yearly average for PM_{10} and $PM_{2.5}$ was notably below the EU limit values (40 and 25 $\mu g/m^3$, respectively). For $PM_{2.5}$, the WHO AQG value for the yearly average is 5 $\mu g/m^3$, and the recommended 24-h limit value is 15 $\mu g/m^3$ [69]. $PM_{2.5}$ concentrations have exceeded this limit many times. Exceedances occurred primarily during heating periods. The percentage of polluted days (i.e., days with concentrations greater than 15 $\mu g/m^3$) to sampling days dropped significantly during the COVID compared to the baseline. For example, during the winter, $PM_{2.5}$ concentrations exceeded the WHO AQG limit on about half of the sampling days, but during the COVID years,

the proportion was lowered to less than 20%. The $PM_{2.5}/PM_{10}$ ratio was 0.57 ± 0.15 for the whole period, fluctuating between 0.7 during the heating season and 0.5 on average during the summer, which is comparable with previous results corresponding to Debrecen [164, 165]. The $PM_{2.5}/PM_{10}$ ratio remained unchanged under the COVID compared to baseline.

During lockdowns 1 and 4, the behavior of air pollutants differed from what was expected. Despite the rigorous precautions and the fact that life in the city has come to a stop, the anticipated valuable reduction in pollution did not occur during the first lockdown. On the other hand, during lockdown 4, the opposite occurred: while there were no restrictions and life returned to normal, the concentration of most pollutants was 25%–30% lower than the baseline. The solution to this apparent contradiction is expected to be found by studying the composition, sources, meteorological conditions, and geographical source areas.

3.2.2 Elemental composition of PM_{coarse} and $PM_{2.5}$

The average PM concentrations and measured species during the two time periods for the coarse and fine fractions are summarized in Tables **3.11** and **3.12**, respectively. The mineral dust component has been calculated as follows: 1.46 [Mg] + 1.9 [Al] + 2.14 [Si] + 1.4 [Ca] + 1.67 [Ti] + 1.42 [Fe] [166]. Assuming that S exists as SO_4^{2-} and mineral dust elements are present in their common oxide form, the detected components account for 40%–50% of the total PM mass [31]. Organic carbon (OC), nitrate (NO_3^-), and ammonia (NH_4^+) are anticipated to make up the unmeasured portion of PM mass.

Mineral dust was the main component of PM_{coarse}, contributing more than 30% of the total amount in both time periods. The primary constituents of $PM_{2.5}$ were BC 14%–16%, SO_4^{-2} 17%–20%, and mineral dust 11.5%–14%. These results agree with prior findings [163–165] as well as data from other studies related to urban sites in the region [151], [167]. Figures **3.15–3.20** show the time series of PM_{coarse} and $PM_{2.5}$, as well as their primary components.

Table 3.11 Mean (AVG), standard deviation (SD), median, maximum, and minimum concentrations (in ng/m^3) of elemental, and mineral dust (Min-dust) components of **PM_{coarse}** and contribution of some components to the PM mass in % for pre- and during COVID periods

	Pre- COVID (March 2018- Feb 2020)					COVID (March 2020- Feb2022)				
	AVG	**SD**	**MED**	**Max**	**Min**	**AVG**	**SD**	**MED**	**Max**	**Min**
Na	82.9	63.0	66.8	321.5	3.4	81.5	175.0	39.0	1461.4	3.4
Mg	45.5	41.8	32.3	316.0	1.4	34.4	37.7	24.8	327.1	2.4
Al	230.4	239.6	145.7	1704.8	12.2	166.2	159.5	120.2	811.7	2.0
Si	781.0	790.1	527.1	6006.8	37.6	591.3	538.6	445.3	2631.4	6.6
P	11	8.3	9.4	42.8	1.8	8.4	5.7	7.5	26.6	1.6
S	93.4	67.9	72.2	397.8	18.4	72.6	105.6	45.4	1166.3	5.2
Cl	104.6	108.1	68.2	637.5	3.8	58.2	18.8	18.5	1867.9	1.9
K	109.0	86.6	80.3	593.3	22.3	91.5	73.7	70.1	369.2	11.0
Ca	263.2	222.1	198.9	1498.9	15.6	226.1	213.1	174.5	1751.6	14.8
Ti	15.8	16.3	10.6	126.8	0.2	12.3	12.8	9.2	60.4	0.2
V	0.6	0.6	0.4	4.0	0.1	0.9	1.2	0.4	6.3	0.1
Cr	0.6	1.0	0.1	9.3	0.1	0.4	0.7	0.1	3.5	0.1
Mn	6.9	5.1	5.6	37.7	0.9	6.8	4.9	5.8	26.1	0.3
Fe	238.3	187.6	181.6	1201.9	44.3	189.1	155.6	148.3	882.4	28.2
Co	1.8	1.1	1.5	7.1	0.3	1.6	1.3	1.3	7.0	0.1
Ni	0.5	0.3	0.4	1.8	0.1	0.4	0.4	0.2	1.8	0.1
Cu	2.0	1.7	1.5	9.2	0.1	1.3	1.3	1.0	7.6	0.05
Zn	4.6	3.2	3.7	15.4	0.6	3.6	2.9	2.7	18.8	0.7
Br	0.3	0.3	0.2	1.6	0.1	0.4	0.4	0.2	2.3	0.1
Ba	6.0	3.3	5.0	18.8	0.8	4.9	3.1	4.3	17.4	1.1
Pb	2.2	1.5	1.7	6.7	0.2	2.0	1.9	1.4	12.4	0.2
PM_{coarse}	8300	6300	6100	36600	700	6700	5500	4600	27500	1000
PM_{10}	19200	9500	17400	52000	3600	14900	13800	8300	51800	3400
SO_4^{2-}	280.1	203.6	216.6	1193.3	55.3	217.7	316.7	136.3	3499.0	15.5
Min-dust	2915.4	2746.5	2016.1	18710.2	197.8	2242.0	1991.5	1725.7	9837.5	85.9
SO_4^{2-} %	4.7	4.5	3.2	36	0.9	3.8	3.4	2.6	18	0.4
Min-dust%	32.4	10	33.4	52.4	3.1	31.0	11.5	31.0	65.4	3.9

Table 3.12 Mean (AVG), standard deviation (SD), median, maximum, and minimum concentrations (in ng/m^3) of elemental, BC, and mineral dust (Min-dust) components of **$PM_{2.5}$** and contribution of some components to the PM mass in % for pre- and during COVID periods.

	Pre-COVID (March 2018- Feb 2020)					COVID (March 2020- Feb2022)				
	AVG	**SD**	**MED**	**Max**	**Min**	**AVG**	**SD**	**MED**	**Max**	**Min**
Na	60.6	41.9	50.2	213.2	3.2	71.6	155.0	42.8	1578.6	2.76
Mg	22.0	27.5	14.5	232.1	2.3	22.6	40.2	14.7	438.4	0.49
Al	101.7	121.2	60.7	973.7	1.9	86.9	108.8	55.0	934.1	0.6
Si	300.8	332.1	186.6	2326.1	16.1	268.2	293.6	183.2	2339.8	15.1
P	4.3	2.5	3.9	13.6	1.4	4.0	2.7	3.2	18.2	0.6
S	590.4	359.2	510.7	1769.6	49.7	497.7	271.8	403.7	1645.3	79.8
Cl	5.3	5.3	3.1	33.3	1.1	12.1	34.0	4.8	301.6	1.1
K	194.3	145.0	145.7	773.0	20.2	169.1	164.9	115.3	1078.8	22.1
Ca	87.2	84.2	61.3	650.0	3.0	96.5	159.2	67.1	1798.9	6.3
Ti	6.1	7.2	3.7	52.0	0.15	5.4	7.1	3.4	60.6	0.1
V	0.4	0.3	0.4	1.7	0.1	0.6	0.7	0.4	4.1	0.1
Cr	0.6	0.6	0.4	2.7	0.1	0.2	0.2	0.1	1.5	0.1
Mn	4.6	3.9	3.7	24.8	0.4	6.2	3.2	5.7	20.3	0.8
Fe	119.1	84.4	90.5	565.2	7.4	112.0	83.1	94.7	648.6	21.8
Co	1.0	0.6	0.9	3.7	0.2	1.1	0.8	0.9	6.6	0.3
Ni	0.4	0.3	0.4	1.5	0.1	0.3	0.3	0.2	2.7	0.1
Cu	2.3	1.8	1.7	9.1	0.1	1.9	1.4	1.5	9.7	0.1
Zn	11.4	7.9	9.2	48.6	1.7	9.3	7.4	6.7	40.9	1.4
Br	1.0	0.7	0.8	3.5	0.1	1.5	1.4	1.1	8.5	0.1
Ba	2.8	2.0	2.3	11.2	0.7	3.0	2.4	2.6	21.4	0.7
Pb	5.0	3.7	4.1	23.5	0.7	4.4	3.5	3.4	18.4	0.4
SO_4^{2-}	1771.2	1077.5	1532.2	5308.8	149.2	1493.2	815.3	1211.0	4936.0	239.4
Min-dust	1173.9	1205.9	771.6	9004.8	73.6	1078.9	1180.4	760.4	9177.1	91.2
BC	1519.5	1116.4	1182.2	5945.8	96.5	1279.9	1013.7	926.2	4777.6	125.4
$PM_{2.5}$	10900	5600	10100	32500	2200	8200	5200	7100	37300	1900
SO_4^{2-}%	16.6	6.3	15.6	34.7	4.1	20.0	7.0	19.5	42.3	2.8
Min-dust%	11.5	9.4	9.3	53.2	0.8	13.8	9.2	12.8	46.6	0.8
BC %	13.9	7.4	13.0	37.9	1.0	15.8	6.2	15.7	30.7	2.7

Seasonality can be observed in the time series of both PM size fractions and their components. Winter maximums and summer minimums have been seen for $PM_{2.5}$, as well as for BC, K, Pb, and Zn. These components have a strong association with household heating, which explains their increased occurrence throughout the heating season. The fine fraction S showed little seasonal variation, whereas the coarse fraction S had winter maxima, indicating that its source was possibly local heating (see Figure **3.20**). Regional transportation is the source of S in $PM_{2.5}$, as will be explained later. Mineral dust elements have maximums in the spring and autumn and minimums in the winter in both size fractions. The same behavior may be seen with PM_{coarse}. This pattern must be explained through meteorology and seasonal agricultural work. During the vegetation period phosphorus, a fingerprint element of biogenic emission, is present in significant amounts. Elements connected to traffic (for example, Cu) did not display seasonal changes.

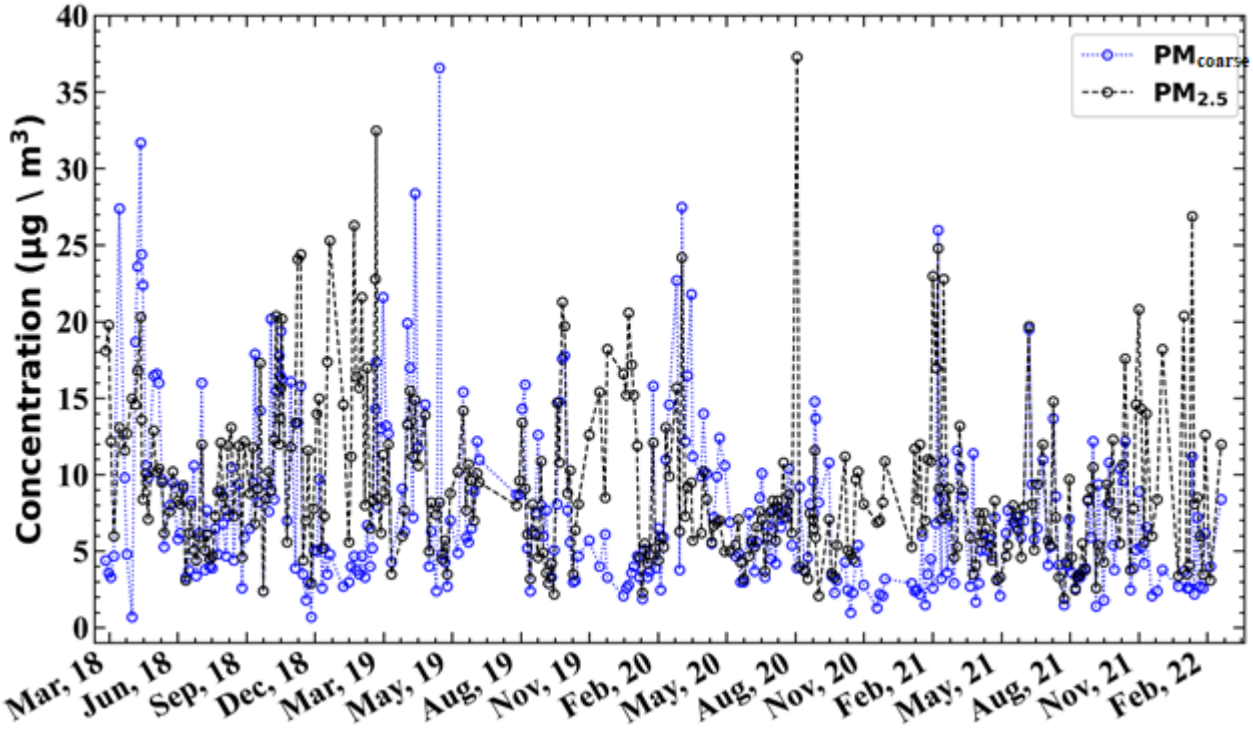

Figure 3.15. Time series of measured PM in coarse and fine fractions from March 2018 to Feb 2022.

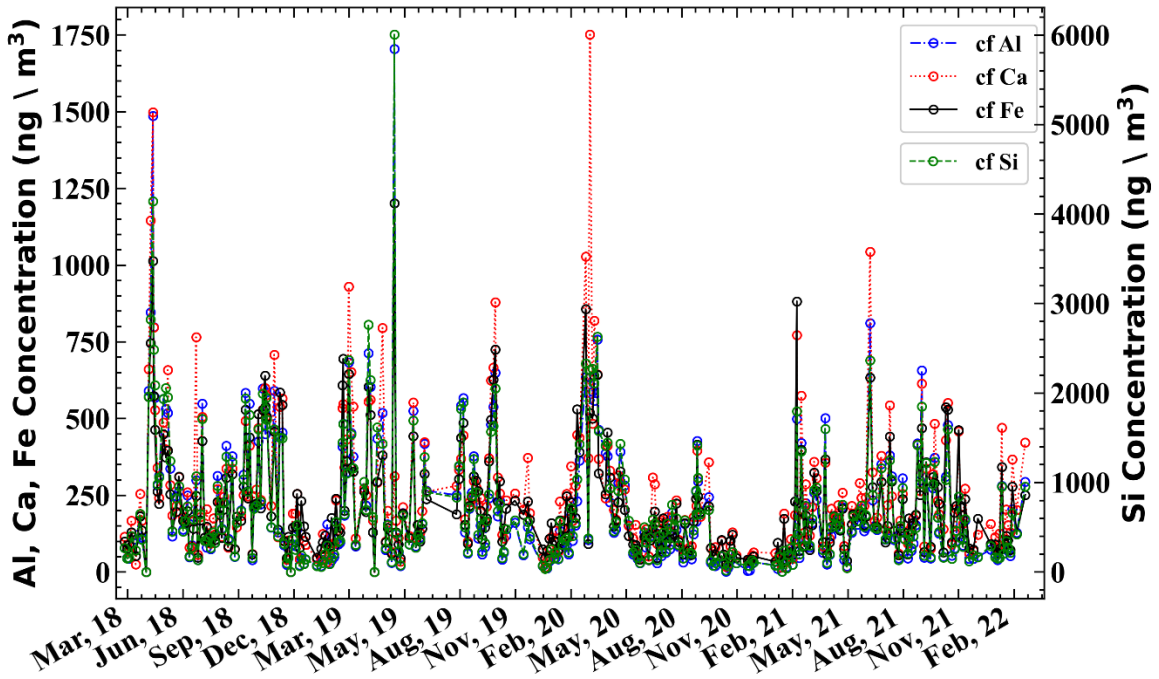

Figure3.16. Time series of Fe, Ca, Al and Si concentrations in coarse fraction from March 2018 to Feb 2022.

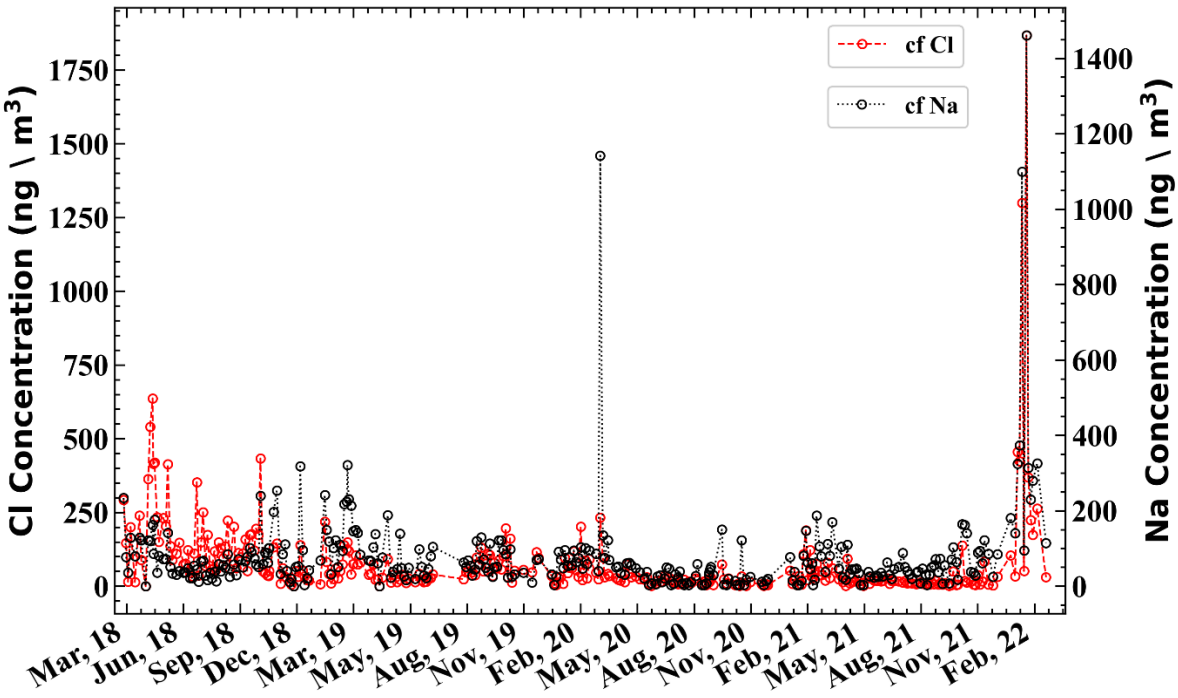

Figure 3.17. Time series of Na and Cl concentrations in coarse fraction from March 2018 to Feb 2022.

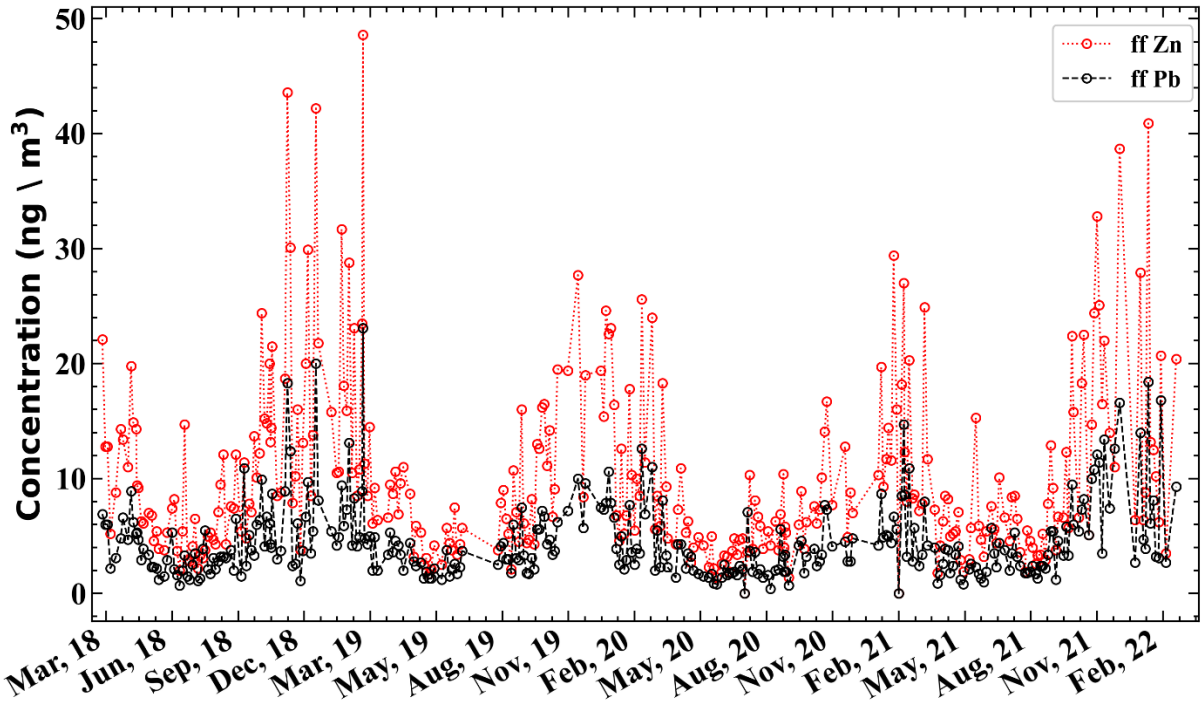

Figure 3.18. Time series of Pb and Zn concentrations in fine fraction from March 2018 to Feb 2022.

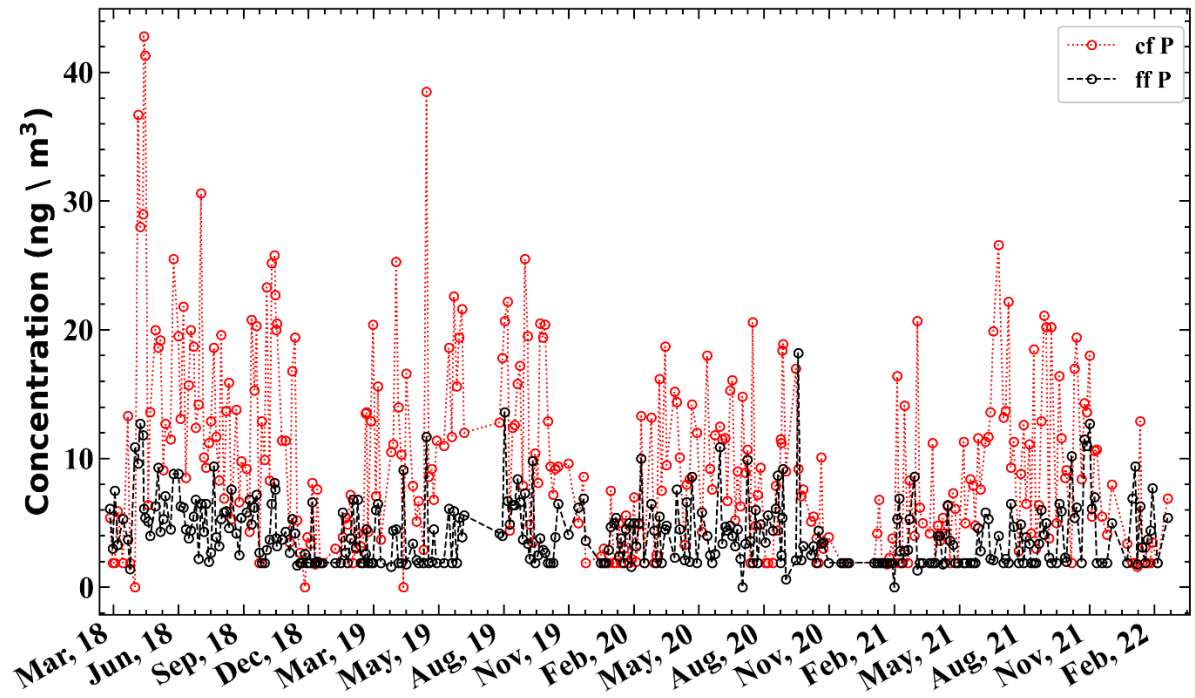

Figure 3.19. Time series of P concentration in coarse and fine fraction.

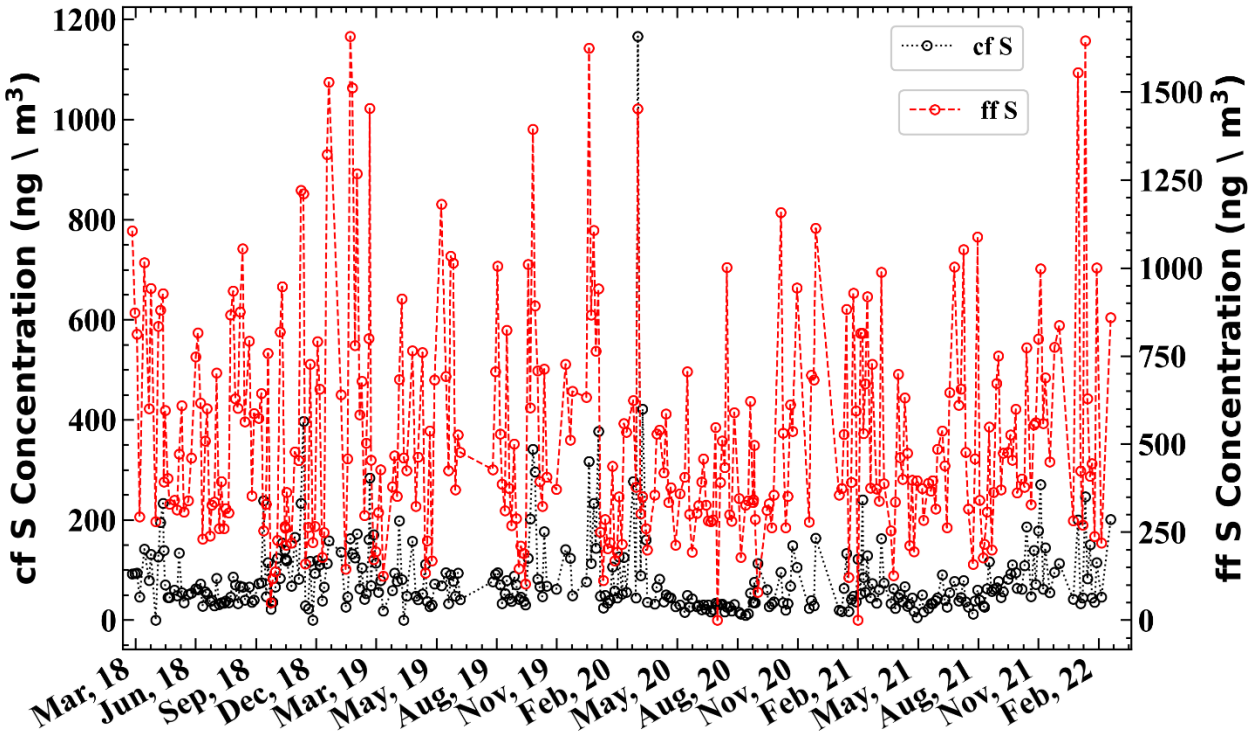

Figure 3.20. Time series of S concentration in coarse and fine fraction.

Several episodes can be seen in the mineral dust time series, which are associated with Saharan and Asian dust episodes as well as local sand storms. Backward trajectories and the composition of the sample were helpful in identifying these episodes. Local sandstorms, for example, have a relatively high Si content, but Sharan dust often has a high Ti and Fe content. There were numerous Saharan episodes throughout the study period, usually in the spring (see Figure **3.21**). Mg and Sr were found in extraordinarily high amounts in aerosols collected on March 26, 2020. Backward trajectories identified that they originated from Asia, the Caspian Sea region, and the Karakum Desert (Figure **3.22**).

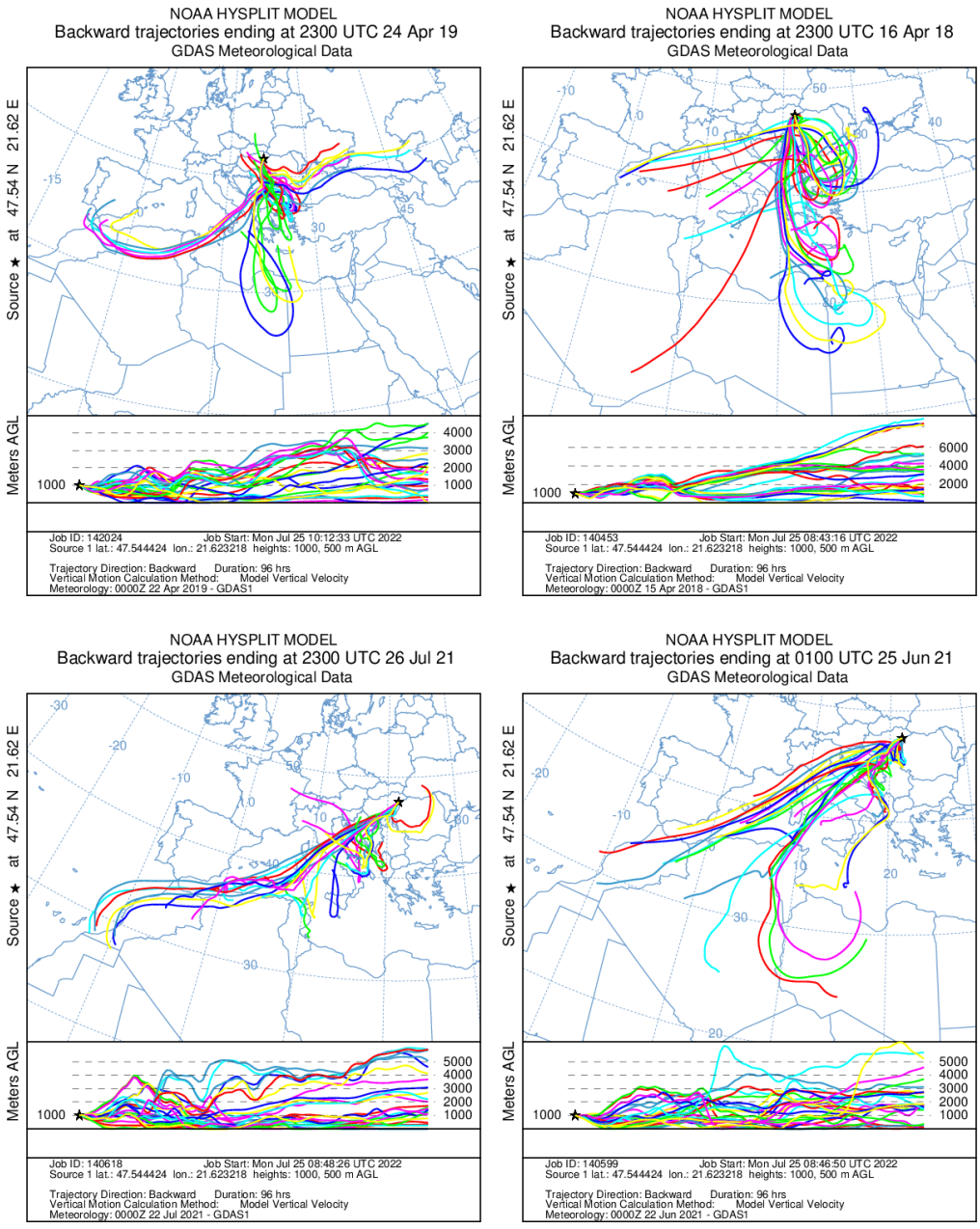

Figure 3.21. Backward trajectories (trajectory ensembles)[1] of Saharan dust events in April 2018, April 2019, and June, July 2021 by NOAA HYSPLIT model (96 h backwards, 1000m AGL)

[1] Trajectory ensembles were calculated to reduce errors associated with a single trajectory. These are all trajectories calculated for the same starting location and same starting time, with offsetting the meteorological data by a fixed grid factor (one grid meteorological grid point in the horizontal and 0.01 sigma units in the vertical). This results in 27 members for all-possible offsets in X, Y, and Z. (https://www.ready.noaa.gov/hypub-bin/trajtype.pl).

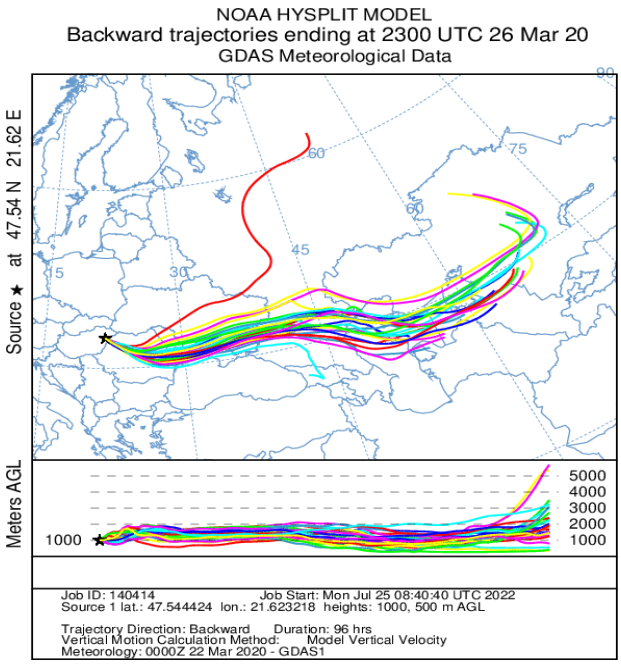

Figure 3.22. Backward trajectories of Asian dust event on 26 March, 2020 by NOAA HYSPLIT model (96 h backwards, 1000m AGL).

The case of chlorine is never straightforward: it can come from a variety of sources in both size fractions, including salt, buildings, pesticides, fertilizers, biomass burning, and industries [168]. Most Cl in the coarse mode occurs as salts, mostly NaCl; thus, we predicted a strong correlation between Na and Cl. However, in Figure **3.17**, Cl has no correlation with Na in 2018, but they move together from 2019. Calculating pairwise correlations (Spearman correlation) for these two periods revealed that the correlation coefficient (r) between Cl and Na was 0.6 in 2018 and 0.9 in 2019-2022. Meanwhile, the Cl:Ca correlation in 2018 was 0.6, and there was no correlation between these two elements in 2019-2022. Cl, together with Ca, points towards construction as its source [168]. Indeed, foundation work for a tower block was carried out nearby in 2018. Cl concentrations over DL in the fine fraction were only measured during the heating period; thus, fine fraction Cl was attributed to biomass burning. The episodic peaks, particularly in the winter of 2021–22, appeared alongside Na; thus, their source was most likely sea salt, which assumption was proven by backward trajectory calculations, too (Figure **3.23**).

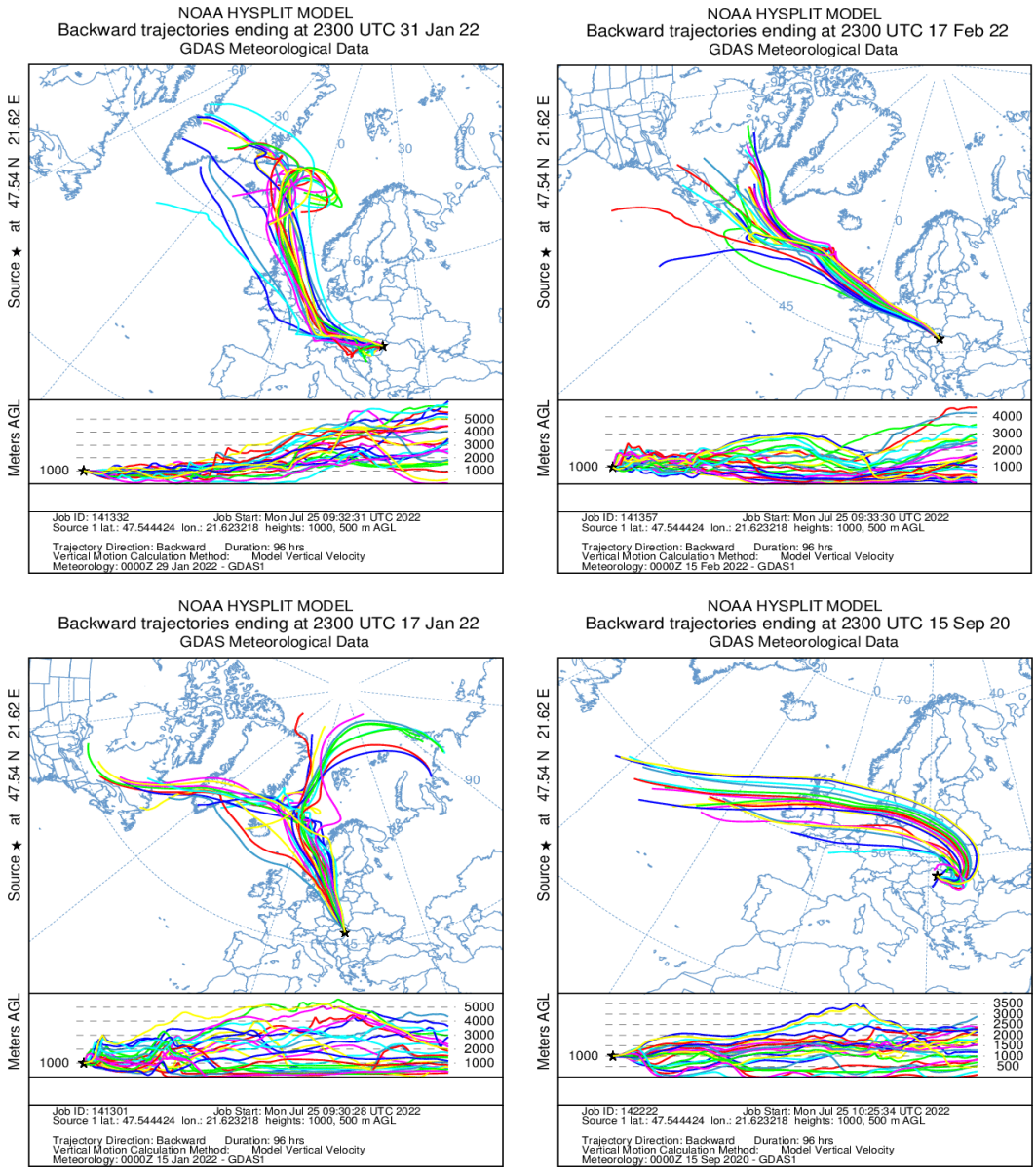

Figure 3.23. Backward trajectories of Na and Cl episodes in January-February 2022 and September, 2020 by NOAA HYSPLIT model (96 h backwards, 1000m AGL)

Black carbon (BC) was a major component of $PM_{2.5}$, with concentrations ranging from 0.7 μg/m^3 (summer) to 2 μg/m^3 (heating season) and the average seasonal contribution ranging from 7% (summer) to 28% (winter). Its main sources in an urban setting are vehicular traffic and biomass burning (BB) [169,170]. One way to separate BC originating from the two sources is to study the correlation to tracer elements such as K and levoglucosan [171]. Another method is measuring the absorption of BC at different wavelengths [105], [106], as described in Section 2.4. Figure **3.24** displays the time series of BC along with K, as well as the concentration difference determined at 405 nm and 1050 nm.

There is a significant seasonal dependence on BC concentration. It shows highs in the winter and lows in the summer. The fine fraction K has a strong correlation with BC (r = 0.9), indicating that biomass burning is its primary source. In the winter, wood is used for residential heating. The concentration difference also shows that during the heating season (November–March), the predominant source was BB, but during the summers, it was traffic. Figure **3.24** offers some further interesting details. In 2018 and 2019, there were high BB signals in September–October, which were most likely caused by field fires or the burning of organic waste in gardens (a frequent practice despite EU laws) [102], These indicators have disappeared totally during the COVID era, indicating lower activity in these locations as well.

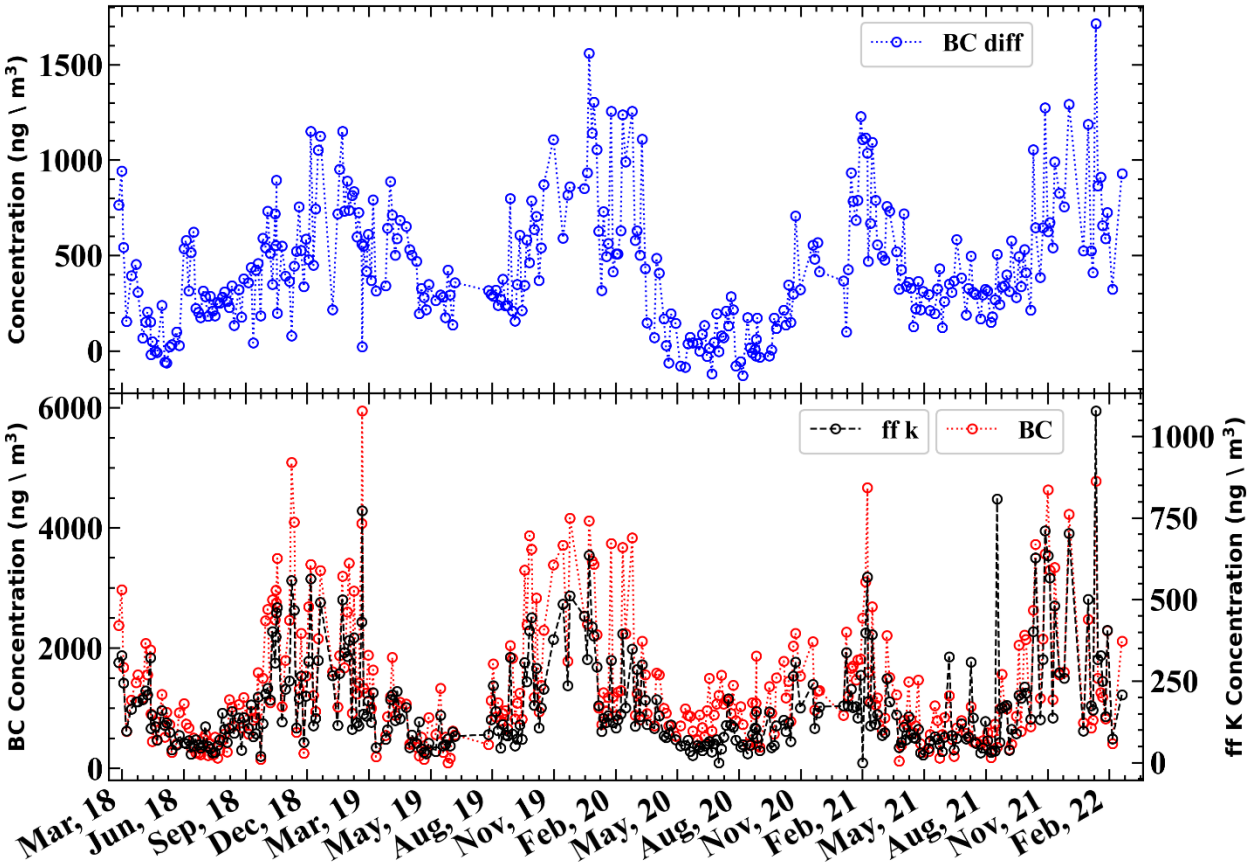

Figure 3.24: concentration difference of BC measured at 405 and 1050 nm. (BC_{diff} = BC_{405nm}-BC_{1050nm}) and time series of BC and K in fine fraction.

3.2.3 Sources of PM pollution in Debrecen

Source apportionment using positive matrix factorization found 8 factors for both the coarse and fine fractions. Figures **3.25** and **3.26** show the factor profiles and time series of relative source contributions obtained for the coarse and fine fraction, respectively. The coarse fraction factors were assigned to the following sources: traffic, two types of soil, two types of combustion, roadworks, a mixed source of construction and Cl salts, and biogenic emissions. Pollution sources in $PM_{2.5}$ were identified as **2** soil types, biomass burning, combustion, roadworks, traffic, sea salt, and secondary sulphates.

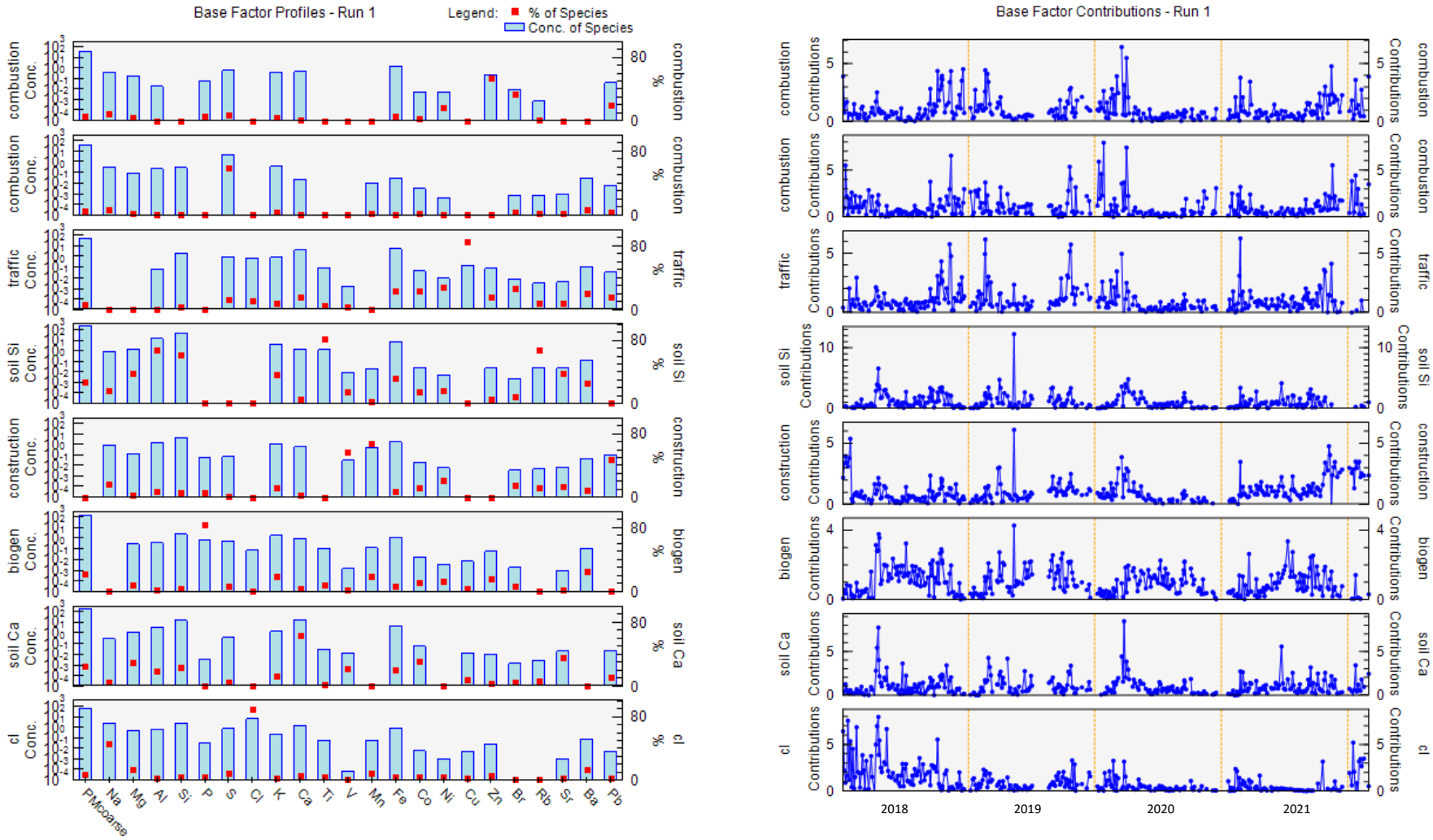

Figure 3.25. Source profiles and factor contributions for the **coarse fraction**. The blue bars represent the concentrations of components on a logarithmic scale, in ng/m^3. The red dots show the relative contribution of each source to the total concentration of the given component in %. On the right side is the time series of relative factor contributions (when factor contribution is normalized to 1)

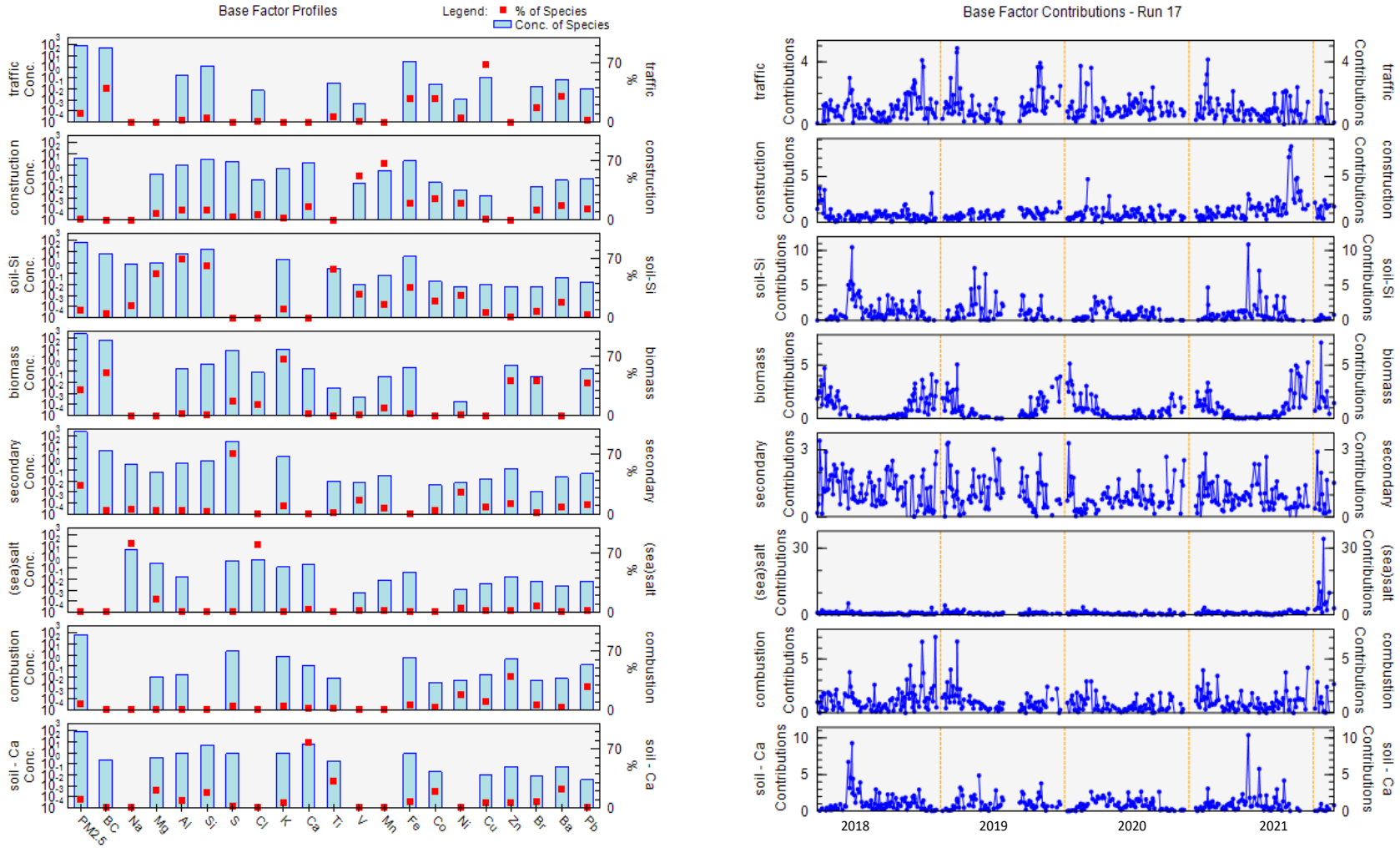

Figure 3.26. Source profiles and factor contributions for the **fine fraction**. Blue bars represent the concentrations of components on a logarithmic scale, in ng/m^3. The red dots show the relative contribution of each source to the total concentration of the given component in %. On the right side is the time series of relative factor contributions (when factor contribution is normalized to 1).

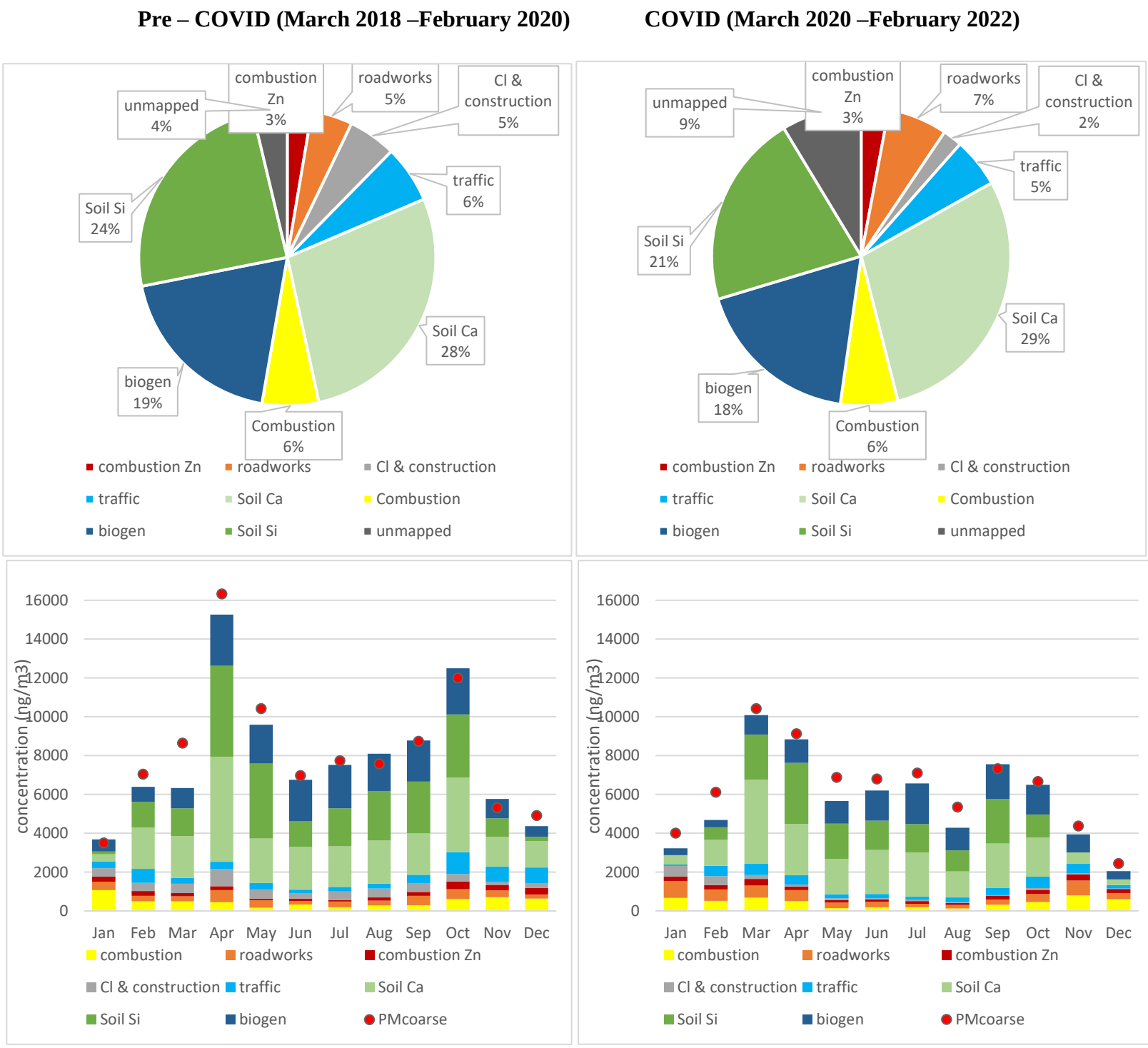

Figure 3.27. Source contributions of PM_{coarse} before and during the COVID-19 pandemic and the monthly variation of source contributions in the coarse fraction.

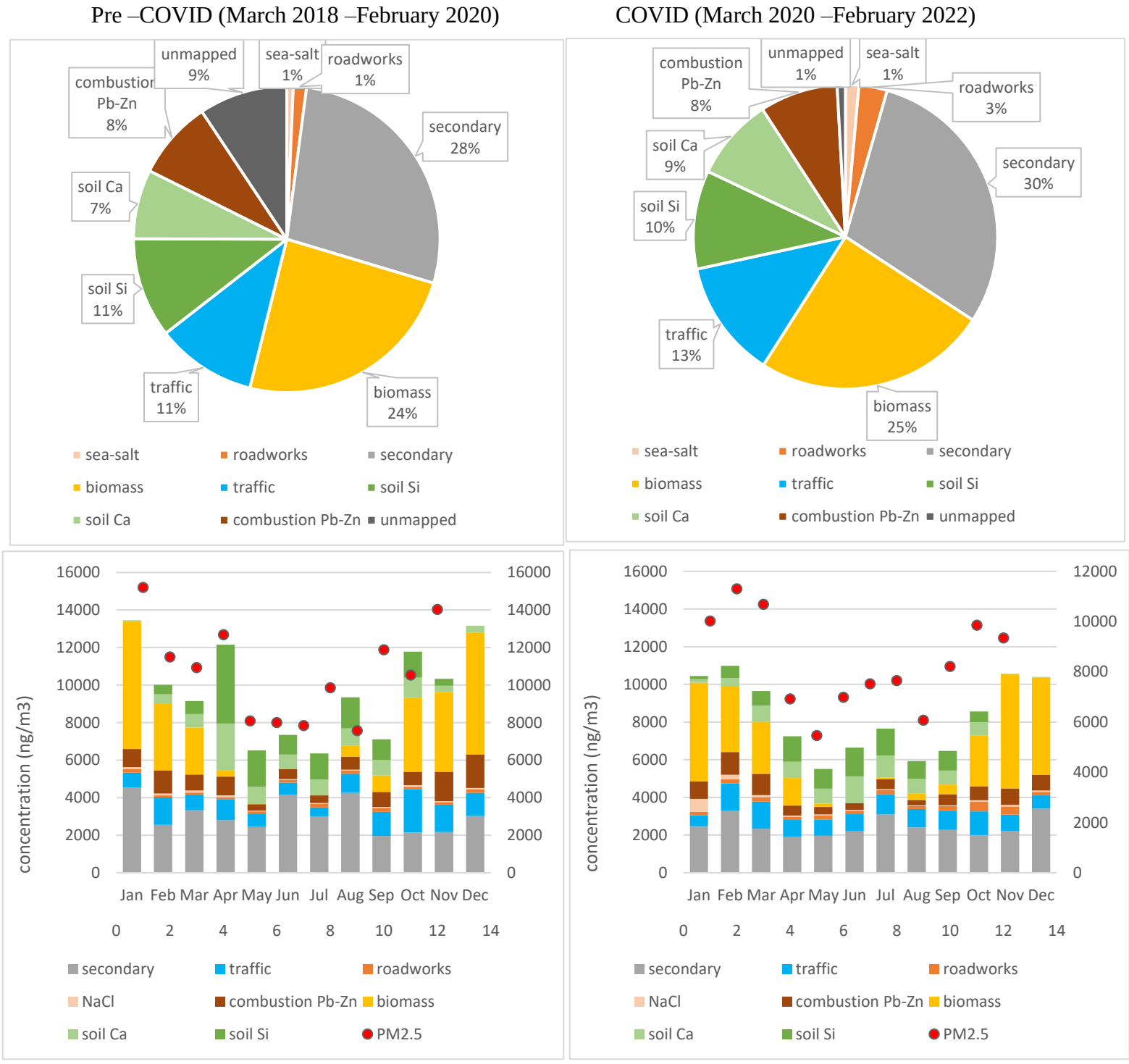

Figure 3.28. Source contributions of $PM_{2.5}$ before and during the COVID-19 pandemic and the monthly variation of source contributions in the fine fraction.

Figures **3.27** and **3.28** show the source contributions for the coarse and fine fractions, respectively. Mineral dust elements such as Mg, Al, Ca, Si, Ti, Fe, Rb, Sr, and Ba are found in the soil factors. The presence of two soil types is explained by the city's location on the border of a loess and a sandy area, as previously mentioned. Soil contributed around 50% of PM_{coarse} and 18% of $PM_{2.5}$. The contribution of soil components was greatest in spring and early autumn, while it was almost completely absent in winter. The dry and windy weather encourages dust resuspension, which increases by agricultural field activity. Furthermore, Saharan dust episodes, which frequently occur in the spring, contribute significantly to soil factors too.

BC and heavy metals such as Cu, Fe, Co, Br, and Pb characterize the traffic source. These elements are vehicle transport tracers, such as break, wear, tramway abrasion, and diesel fuel exhaust [172,173]. For the coarse and fine fractions, traffic contributed 6% and 12%, respectively. Before the pandemic, the traffic source was the strongest in the months of the school year. The gap between the academic year and vacation time has been equalized over the years of COVID.

One of the most significant sources of $PM_{2.5}$ is biomass burning. It is identified by high K and BC concentrations. It contributed more than 50% during the heating season but was undetectable throughout the summer months. The combustion factor is characterized by Zn, Pb, and Br. Its possible origin is a boiler of a neighboring condominium or a secondary school dormitory near the sampling site, which provides heating and warm water all year. It, like the BB source, reaches maximums during the heating season.

A similar combustion source was identified in the PM_{coarse}, contributing 3% on average. Another factor contributing to the coarse fraction's high S content was fossil fuel burning from residential heating. It contributed 6% on average per year, with the highest output in the winter and the lowest in the summer.

The factor ‘secondary aerosol' is another major source of $PM_{2.5}$. It is marked by a high Sulphur content. The main origin of different SO_4^{-2} compounds is the burning of fossil fuels [174]. This factor also contains V and Ni, which are heavy oil combustion's fingerprint elements. Secondary sulphate contributed about 28%–30% of the total mass of $PM_{2.5}$. Secondary sulphate has a residence time of 2–10 days [175] allowing for regional and long-distance transportation. Figure **3.29** shows that the source origins of secondary sulphate pollution in Debrecen were the industrial

districts of SW Romania, the Balkan countries, and, on occasion, western Ukraine, and southern Poland.

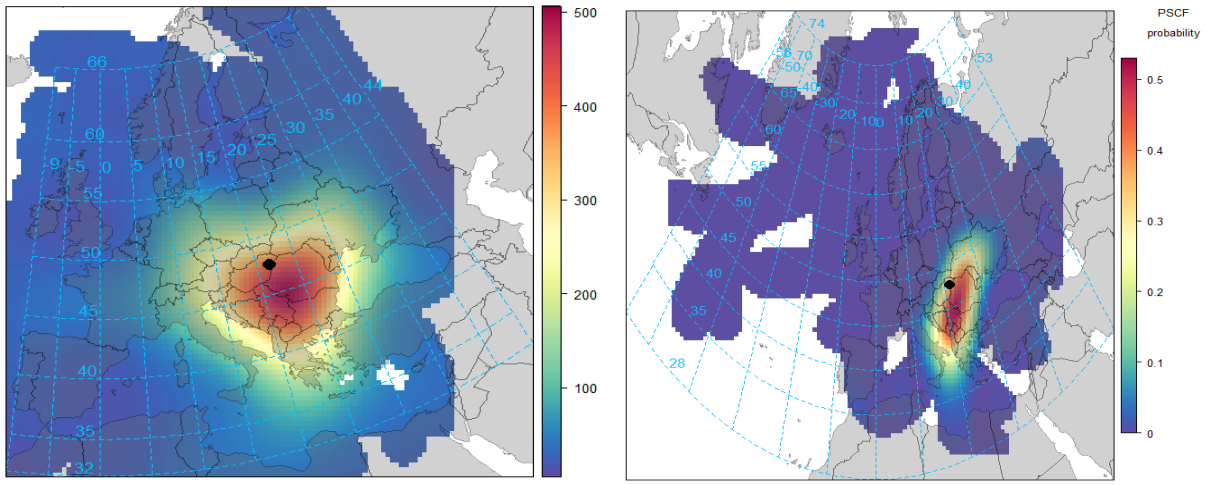

Figure 3.29. Results of CWT (left) and PSCF (threshold: 75%) (right) of S in $PM_{2.5}$ for summer 2018-2019.

Biogenic emissions were a major component of PM_{coarse}, accounting for 19% of the yearly average contribution. This factor's distinguishing elements were P and K, both of which are the necessary substances for plants. This source was dominant during the vegetative period, with summer peak levels.

Mn, soil dust elements, and metals are assigned to the road works factor in both size fractions. This was a temporary source, beginning in 2021, when major road renovations in neighboring streets were starting along with tram line rail replacement. A construction/building factor also appears in PM_{coarse}. This can be linked to the construction of a tower block, as previously discussed in connection with Cl. This is a mixed source of construction and salt. The factor which includes 90% of the fine fraction Na and Cl is identified as sea salt. The contribution of these sources was a small percent, and they were only present occasionally.

Figures **3.27** and **3.28** show that, considering the whole year, there was essentially no change in the relative contribution of sources between the period of pre-COVID and COVID, with the exception of temporary sources such as construction and roadworks. The seasonal variation in both fractions was similar in the two studied periods; however, the differences became smaller during

the COVID years. The high soil factor concentrations in April pre-COVID and March COVID resulted by many Saharan dust episodes. In the pre-COVID years, an increased contribution of soil can be observed in October. The most likely explanation is a shortage of precipitation this month in 2018 and 2019, as well as increased agricultural activities, as discussed previously in connection with the BC timeline.

3.2.4. COVID crisis induced changes in $PM_{2.5}$, PM_{coarse}, composition and sources

Tables **3.13** and **3.14** show the relative changes in $PM_{2.5}$, PM_{coarse}, elemental components, and source contributions among the investigated time periods. Species for which the change was found significant by using the Mann-Whitney-U test are highlighted in red. Taking the whole period into account, $PM_{2.5}$, PM_{coarse}, and PM_{10} concentrations were 25%, 20%, and 22% lower, respectively, during the COVID years than the corresponding baseline values.

Almost all elemental components showed a significant drop in the coarse fraction, with a few exceptions. Mineral dust and soil factors were reduced by 30% on average. The reduction in traffic-related elements and sources was more than 40%. Biogenic emissions were also reduced by 30%, which could be attributed to lower resuspension due to traffic and a reduction in agricultural activity on the land surrounding them.

In the case of $PM_{2.5}$, only traffic-related elemental components such as Cu and Zn showed significant changes. In the cases of BC and S the change was significant throughout the summer (25% increase for BC and 35% decrease for S). Source contributions decreased by 10%–30% on average, with the exception of the periodic sources of sea salt and roadworks.

Figure 3.13. Relative change of PM_{coarse}, components and source contributions %

	Whole period	SPRING		SUMMER		SEP/OCT		NOV		WINTER	
		LD1	LD3	Relax 1	Relax2	Relax1	Relax2	PRE-LD2	PRE-LD4	LD2	LD4
PM_{coarse}	-20	3	-51	-22	-15	-35	-32	-37	4	-13	-29
Na	-2	-22	-30	-57	-28	-67	-17	-30	37	-62	266
Mg	-32	4	-50	-65	-19	-57	-13	-47	-4	-60	48
Al	-39	5	-57	-58	-12	-57	-20	-79	-11	-40	-17
Si	-32	11	-55	-51	-9	-55	-21	-75	-14	-34	-21
P	-33	-33	-56	-37	-24	-34	-19	-45	40	-28	-17
S	-29	15	-37	-57	-30	-53	-15	-34	15	-38	-19
Cl	-80	-63	-78	-77	-81	-81	-80	-78	-52	-37	484
K	-19	24	-47	-43	2	-51	-15	-63	21	-26	-4
Ca	-16	58	-44	-39	7	-51	-15	-68	3	-33	-7
Ti	-28	22	-53	-43	4	-47	-27	-68		-10	
Mn	-2	14	-10	-55	31	-54	6	-67	103	-44	219
Fe	-26	28	-45	-43	2	-54	-16	-67	6	-25	-29
Co	-13	45	-26	-43	21	-54	-8	-67	3	-30	-21
Cu	-49	14	-17	-45	9	-65	-18	-73	-12	-31	
Zn	-29	39	-23	-33	-3	-60	-20	-64	20	-42	-28
Rb	-2	53	-39	-40	15	-50	-12	-27	48	-21	-10
Ba	-23	23	-15	-22	23	-42	-19	-45	-64	-18	-68
Pb	-8	36	-4	-55	20	-67	-12	-68	94	-40	61
Min-dust	-30	17	-53	-50	-6	-54	-19	-73	-8	-34	-18
Min-dust contribution%	-5	13	-2	-33	15	-38	22	-54	-2	-32	22
SO_4^{2-} contribution%	-22	15	1	-41	-13	-14	65	3	12	-23	-9
Source contributions											
Traffic	-45	-6	8	-40	35	-69	-18	-70	-13	-20	-91
Soil Ca	-19	33	-47	-33	5	-43	-17	-60	-62	-37	-68
Soil Si	-44	5	-60	-57	-13	-54	-28	-81		-33	
Combustion	-24	76	-22	-59	-34	-43	3	-12	45	-43	-12
Combustion Zn	-12	89	8	-12	3	-56	-15	-55	67	-55	-4
Roadworks	14	36	-23	-73	28	-72	6	-79	266	-39	371
Cl & construction	-210	-75	-80	-80	-89	-84	-89	-82	-65	-45	171
Biogen	-31	-31	-52	-32	-16	-27	-24	-29	2	-34	-62

Figure 3.14. Relative change of $PM_{2.5}$, components and source contributions %

	Whole period	SPRING		SUMMER		SEP/OCT		NOV		WINTER	
		LD1	LD3	Relax 1	Relax2	Relax1	Relax2	PRE-LD2	PRE-LD4	LD2	LD4
$PM_{2.5}$	-25	-16	-33	-13	-21	-40	-19	-24	18	-10	-24
PM_{10}	-22	-6	-43	-18	-19	-37	-26	-28	13	-11	-25
BC	-19	45	-3	54	-3	-43	-20	-23	31	-16	-23
Na	15	-22	-40	-32	5	-60	-12	-8	32	-26	284
Mg	3	1	-64	-30	35	-45	31	-16	-14	4	160
Al	-17	-5	-68	-37	36	-46	7	-57	-5	-19	-2
Si	-12	4	-65	-30	30	-41	5	-51	-4	-15	-10
P	-9	-9	-42	-15	-37	6	-8	-12	117	-26	21
S	-19	-14	-13	-37	-23	-8	9	6	26	-7	1
K	-15	22	-17	-20	7	-55	21	-23	76	-20	17
Ca	10	54	-50	-6	45	-36	12	-51	8	-9	2
Ti	-12	10	-65	-30	32	-26	-19	-61		-3	
Mn	26	13	25	21	62	1	92	7	174	4	89
Fe	-6	22	-44	-18	26	-40	6	-38	24	-12	-16
Cu	-23	-35	-30	-14	4	-42	5	-24	-27	3	-44
Zn	-23	11	-6	-23	1	-45	-2	-29	27	-15	-6
Ba	7	11	-2	11	48	-30	35	-27	-69	5	-22
Pb	-14	1	-4	-24	-5	-37	5	-16	57	-11	25
Min-dust	-9	14	-62	-27	32	-41	7	-48	3	-21	-4
Min-dust contribution %	17	27	-34	4	50	-6	27	-37	-6	-3	45
SO_4^{2-} contribution %	17	1	33	-13	6	50	46	23	10	20	47
BC contribution %	13	83	49	118	49	-9	-12	2	15	-8	0
Source contributions											
Traffic	-12	16	7	73	-9	-40	-38	-33	-45	14	-67
Soil Ca	-10	59	-59	1	58	-39	-16	-86	-104	1	-56
Soil Si	-29	-9	-74	-47	29	-47	-21	-84			-34
Secondary	-21	-42	-13	-39	-33	19	0	34	35	22	-16
Biomass	-26	115	49			-68	-15	-18	93	-32	5
Combustion Pb-Zn	-28	-6	-1	-43	7	-36	6	-43	4	-17	-30
Sea-salt	44	-10	-9	-14	10	-56	22	26	91	-21	545
Roadworks	48	28	47	-25	41	-2	230	-4	307	2	132

When the periods are examined separately, it is clear that the first, strictest closure did not result in a significant drop in pollutant concentrations, but the relaxation period of 2020 resulted in a decrease of 30%–50% for most components. During the first lockdown, from March to May 2020, there was an increase in the amount of some soil-related elements, BC and K. The contribution of soil Ca, biomass burning, combustion, and roadworks increased significantly in both size fractions compared to the same period in the previous two years. There were multiple Saharan dust episodes in March; the average temperature in the spring of 2020 was 1.5 ^{o}C lower, and the air was 10% less humid (Table **3.5**). Furthermore, because people were obliged to stay at home throughout the day, extra heating was required. In addition, car traffic also increased in the residential areas. Thus, the combined effect of meteorology, desert dust storms and the change in the lifestyle of the population caused the anomaly observed in the first lockdown.

The amount of precipitation in the summer and autumn of 2020 was 2–2.5 times higher than the baseline amount. The rainy weather may have resulted in a significant drop of PM and its components in the coarse fraction, whereas the decrease was smaller in the fine fraction, which was less affected by the precipitation. During this time period, enhancement of BC originating from vehicle exhaust emissions and hence traffic source contribution to $PM_{2.5}$ could be observed.

In summer 2021, mineral dust and traffic components, as well as source contributions, were similar to or higher than the baseline levels, when the weather was warm and dry. This time, a considerable decrease in secondary sulphate concentration caused the decrease of $PM_{2.5}$ concentration by 20%. In September–October 2021, somewhat lower concentration values were recorded compared to the baseline, which was followed by a decrease in traffic and soil source contributions; nevertheless, the extent was smaller than in the wet year of 2020. Reduced biogenic emissions and P concentrations also indicate less agricultural activity.

Because the number of COVID cases was increasing considerably in November 2020, people stayed at home and tried to maintain social distance even before the lockdown. As a result, the concentration levels and source contributions to the following lockdowns were similar. During winter 2020–21 and spring 2021, i.e., lockdowns 2 and 3, the results were as expected: a reduction in most components compared to the baseline. The decline was smaller during Lockdown 2, when educational institutions and workplaces remained open. Because of the milder weather, heating (biomass and combustion) may contribute less. During lockdown 3, in spring 2021, we experienced

the biggest reduction of air pollutants in all AQ monitoring points in the city, except at the Klinika site. The concentration of coarse PM and mineral dust was lowered by 50%–60%, while the concentration of $PM_{2.5}$ was reduced by 33%. At the same time, due to the cold weather and the fact that people had to stay at home during the day, the contribution of household heating increased significantly. The traffic contribution did not vary significantly.

The meteorological conditions in November 2021 were favorable for the development of high pollution-level episodes with very low boundary layer and mixing layer heights, low wind speed, and low temperatures. As a result, higher concentrations, especially with $PM_{2.5}$, were recorded as compared to the baseline. At this time, the main pollution sources were household heating and road construction.

In the winter of 2021–22, PM levels were 25% lower than the baseline. Since there were essentially no COVID restrictions this time and life was back to 'normal,' pollution levels similar to baseline were expected. Furthermore, weather conditions indicated a tendency towards further high pollution episodes, as seen earlier in November. The appearance of sea salt in Debrecen's air could be the answer to this controversy. Figure **3.30** shows the cluster means for the whole period of study, for winters 2018 to 2022, as well as for lockdown 4.

In 30% of cases, air masses arrive in Debrecen from the west or northwest. This winter, the percentage was well over 70%. Furthermore, trajectories from Romania were missing. It appears that clean air masses of oceanic origin influenced the air above Debrecen between December 2021 and February 2022, leading to low air pollution levels and a high sea salt content of APM.

Air pollution from long-range and local transport has a significant impact on the evolution of the city's air quality. Secondary sulphate is a major component of $PM_{2.5}$. A considerable drop in the source contribution of secondary sulphate aerosol was seen in spring and summer 2020, as well as summer 2021. CWT calculations revealed that the Sulphur source areas were South-West Romania and the Balkan countries during the 4-year investigation period (see Figure **3.31**); thus, we could conclude that SO_2 emissions in the source areas decreased significantly. Secondary aerosol contributions increased in autumn 2020 compared to baseline. PSCF analysis (Figure **3.32**) showed that the higher S concentration was originated from the Po region.

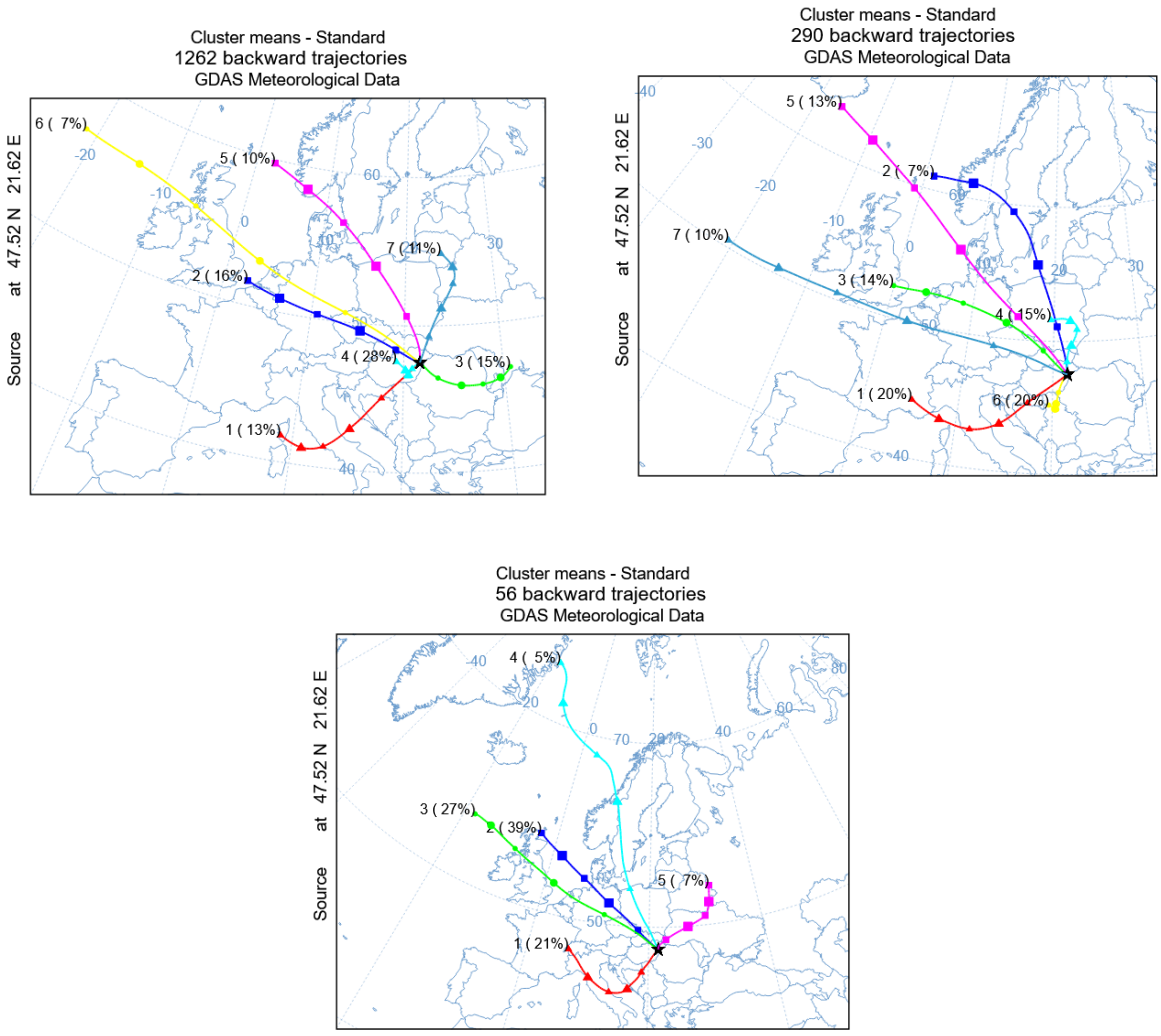

Figure 3.30. Cluster means of backward trajectories calculated by trajectory clustering in HYSPLIT for winter 2018-2022 (left) and December 2021-February 2022 (right).

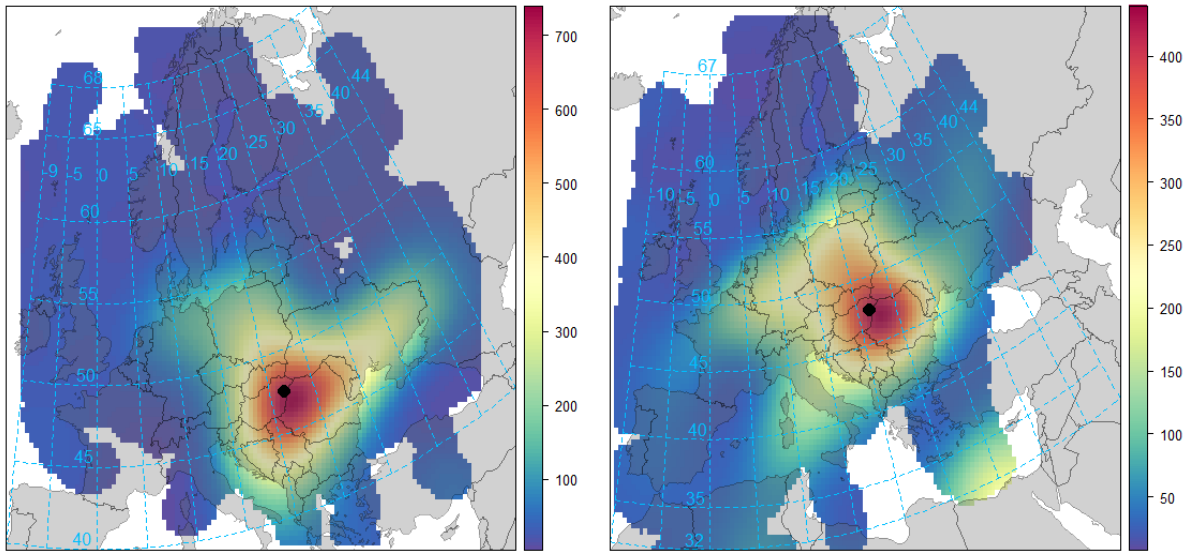

Figure 3.31. CWT analysis for secondary sulphate for summer 2018-2019 (left) and summer 2020-2021 (right)

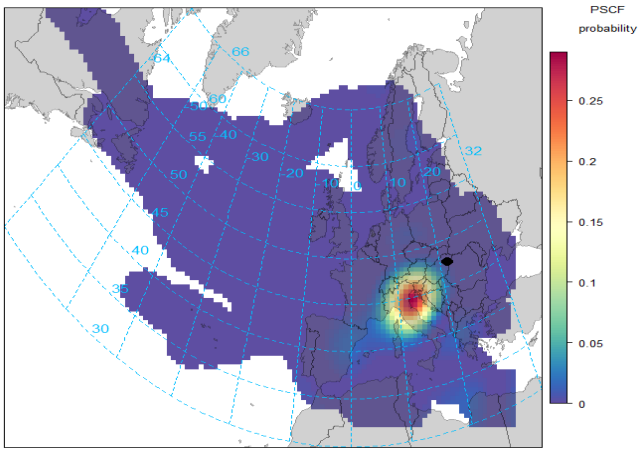

Figure 3.32. Result of PSCF calculation for secondary sulphate in September-November 2020.

4 Summary

Atmospheric aerosols (or atmospheric particulate matter, APM) have significant effects on many aspects of our lives. They affect the Earth's climate as strongly as greenhouse gases, and they cause several health problems like lung cancer, heart disease, and stroke. Therefore, characterization of aerosol pollution and identification of sources of particulate matter are important issues for societies, too.

The COVID-19 pandemic caused by coronavirus (SARS-CoV-2) emerged at the end of 2019. It forced the majority of governments to establish strict regulations and shut down their countries in an effort to stop the spread of the virus. We took this opportunity to study how the different measures introduced locally and globally affect urban aerosol pollution. The objective of my work was to characterize urban particulate matter pollution in Debrecen during the years of the COVID crisis and to compare it with the data from the previous two years.

For this purpose, $PM_{2.5}$, PM_{coarse}, and PM_{10} aerosol samples were collected at an urban background site two times a week between March 2018 and Feb 2022. Concentration, elemental composition, and sources of APM pollution were determined, and the daily concentrations of NO_2, CO, NO_X, and PM_{10} were used from the Hungarian Air Quality Monitoring Network (OLM) stations as complementary data to our study. On this basis, changes in particulate matter pollution induced by lockdowns were studied. The elemental composition of the aerosol samples was determined by the particle-induced X-ray emission (PIXE) method at the new in-air millibeam PIXE setup of the ATOMKI Tandetron accelerator. In the first part of my work, I deal with the characterization of the new in-air PIXE setup. In the second part, the results concerning the aerosol pollution in Debrecen between 2018 and 2022 are presented.

Characterization of the new in-air millibeam PIXE setup

A mobile external millibeam PIXE measurement system have been developed which is capable of the elemental characterization of thin and thick samples in a wide elemental range (N-U) with very good sensitivity. The unique feature of the setup is the detection of very low energy X-rays (down to 0.35 keV) in atmospheric conditions.

Applying a detector cluster with 4 SDD X-ray detectors lead to a significant increase of solid angle of detection. Together with the fast-counting electronics it became possible to collect enough

information about the elemental composition of a sample in a very short time. A typical measurement time of an aerosol sample is now 100-300 seconds.

The analytical performance of the new system was compared to the old in-vacuum PIXE setup of ATOMKI, which was used for PIXE analysis of aerosol samples for over 20 years. Despite the reduced measurement time and the much less collected charge on a sample much better minimum detection limits (MDL) were achieved for the 3 investigated aerosol filter types (polycarbonate, PTFE and quartz) with the new setup.

In order to detect low energy X-rays, He flow have to be applied. A flow rate between 1.5 and 2.5 l/min proved to be optimal. Therefore, in our experiments the He flow was set to 2 l/min.

The effect of the level of He saturation on the quantification of light elements was also presented. I showed that the change of the saturation level with only 1% might lead to significant change in the calculated concentration of light elements. The smaller the atomic number the higher is this effect. For elements with Z >18 it has no influence.

Using the known light element content of aerosol filters and the parallel detection of K and L X-ray lines provide a solution for this problem.

Thanks to the knowledge of light elements the system can be used for the characterization of thick targets as well, when the normalization of the measured concentration to 100% gives very good result as long the sample does not contain unknown quantity of C.

I have shown that the measurement system can be easily supplemented with other detectors if the analytical task requires the use of complementary ion beam analytical methods like PIGE or RBS (Rutherford Backscattering Spectrometry).

Characterization of urban aerosol pollution in Debrecen during COVID-19 lockdowns

In the second part of my thesis, a comparative study of aerosol pollution in Debrecen during the COVID crisis with the previous two years is presented. I studied the changes in the concentration of air pollutants (PM_{10}, NO_x, NO_2, and CO) measured at the 3 fixed monitoring stations of the Hungarian Air Quality Monitoring Network in Debrecen. Furthermore, concentration, elemental composition, and sources of $PM_{2.5}$ and PM_{coarse} were determined at an urban background site in ATOMKI. The variation of aerosol concentration, its elemental composition, and pollution sources were determined between 2018 and 2022. This time interval included 4 lockdowns and 2 relaxation periods, which were also studied individually.

The average concentrations of $PM_{2.5}$, PM_{coarse}, and PM_{10} were higher in the pre-COVID period than during COVID. The decrease in $PM_{2.5}$ and PM_{coarse} was around 25%, 20%, and 22%, respectively. Considering the whole 2-year period of COVID-19, a 20% reduction in average could be detected in the case of most gaseous and APM pollutants and in the components and sources of $PM_{2.5}$ and PM_{coarse}.

The yearly average concentrations for all pollutants and all sites were well below the EU limit values set in Directive 2008/50/EC (40 $\mu g/m^3$ for PM_{10} and NO_2, 70 $\mu g/m^3$ for NO_x, and 3000 $\mu g/m^3$ for CO). Only PM_{10} exceeded daily (24-hour) limit values. In the two years prior to the pandemic, exceedance was 51, 48, and 26 in traffic, UB and SUB sites, respectively. During the pandemic, the values were 23, 24, and 8, indicating a decrease of at least 50%. Most of the excesses happened in November and the winter months.

In the coarse fraction, the main components were the mineral dust elements: Mg, Al, Si, Fe, Ca, and Cl. The contribution of mineral dust to PM_{coarse} mass was more than 30% on average for both periods. The highest contributions were measured in spring and autumn, and the lowest in winter. During COVID a significant decrease was observed in the concentration of almost all elemental components, with a few exceptions. In the case of mineral dust elements, the biggest drop in concentration occurred in autumn, while for elements related to anthropogenic activities like traffic (e.g., Pb, Zn, Cu, Ni), the highest level of decrease occurred in winter. The smallest differences were in the summer. Almost all elemental components showed a significant drop in the coarse fraction, with a few exceptions. Mineral dust and soil factors were reduced by 30% on average. The reduction in traffic-related elements and sources was more than 40%. Biogenic emissions were also reduced by 30%, which could be attributed to lower resuspension due to traffic and a reduction in agricultural activity on the land surrounding them.

In the fine fraction, the main components were BC (14%–16%), SO_4^{2-} (17%–20%), and mineral dust (11.5%–14%). The smallest contribution was measured in the summer, the highest in the winter. BC, K, Cl, Zn and Pb have a strong association with household heating, which explains their increased occurrence throughout the heating season. The concentration of S showed little seasonal variation.

Studying the differences in the components between the pre-COVID and COVID periods it turned out that only traffic-related elemental components such as Cu and Zn showed significant changes. In the cases of BC and S was significant change occurred only throughout the summer periods (25% increase for BC and 35% decrease for S). The source contributions decreased by 10%–30% on average, with the exception of the periodic sources of sea salt and roadworks. The concentration of most components in the summers of 2020 and 2021 increased or did not change compared to the pre-COVID period. The concentration of mineral dust elements dropped significantly in autumn of 2020 and spring of 2021. A definite increase in concentrations of Cl, V, Mn, and Br could be seen. The origin of the metals was most probably the road reconstruction works around the sampling site, which took place in 2021. Sea-salt episodes in the winter of 2021-22 were responsible for the increase of Cl.

I have shown that chlorine had different sources during the investigated period. In 2018, a significant part of the coarse fraction Cl originated from construction because it showed a correlation with Ca. From 2019, it could be found in the form of NaCl, which mainly originated from sea-salt episodes. In the fine fraction the sources of Cl were sea salt and biomass burning.
I have shown that a large part of APM pollution of Debrecen comes from regional and long-range transport. The main source areas of secondary sulphate aerosols were the western Balkan countries and south-west Romania. Therefore, the change in emission in these countries also had a strong influence on the air pollution level in the city.

Using Positive Matrix Factorization (PMF) receptor model analysis, the following sources were identified in the coarse fraction: traffic, two types of soil, two types of combustion, roadworks, a mixed source of construction and Cl salts, and biogenic emissions. Sources identified in the fine fraction were the two soil types, biomass burning, combustion, roadworks, traffic, sea salt, and secondary sulphates. In the coarse fraction, the contribution of soil was ~50% and biogenic emission was 19%. Traffic gave ~6% and combustion 3% contribution. Another factor contributing to the coarse fraction's high S content was fossil fuel burning from residential heating. It contributed 6% on average per year, with the highest output in the winter and the lowest in the summer. The two main contributors in the fine fraction were secondary aerosols and biomass burning with ~ (28–30) % and ~25%, respectively, while the traffic contribution varied around 12% and the soil ~18%. During the heating season the contribution of BB source was ~ 50% and it was undetectable

throughout the summer months. Considering the whole COVID period, there was basically no change in the relative contribution of sources. Differences were found only in the case of temporary sources like construction and roadworks.

I have additionally shown the significance of understanding the impact of local and global meteorological conditions as well as episodic emissions from distant natural and anthropogenic sources.

Publication related to the thesis

In international journals

- Aljboor, S., Angyal, A., Baranyai, D., Papp, E., Szarka, M., Szikszai, Z., Rajta, I., Vajda, I., & Kertész, Z. (2023). Light-element sensitive in-air millibeam PIXE setup for fast measurement of atmospheric aerosol samples. Journal of Analytical Atomic Spectrometry, 38(1), 57–65. https://doi.org/10.1039/D2JA00291D
  IF: 3.4 (Q2) (2022)

- Zsófia Kertész, Shafa Aljboor, Anikó Angyal, Enikő Papp, Enikő Furu, Máté Szarka, Sándor Bán, Zita Szikszai (2024). Characterization of urban aerosol pollution before and during the COVID-19 crisis in a central-eastern European urban environment,,Atmospheric Environment, 318, 120267. https://doi.org/10.1016/j.atmosenv.2023.120267
  IF:5.0 (Q1) (2022)

List of conference talks and posters

- Shafa Aljboor, Máté Szarka, Anikó Angyal, Dávid Baranyai, István Vajda, Zita Szikszai, István Rajta and Zsófia Kertész: The new in-air millibeam-PIXE setup at the ATOMKI Tandetron accelerator, 25th International Conference on Ion Beam Analysis & 17th International Conference on Particle Induce X-ray Emission & International Conference on Secondary Ion Mass Spectrometry, 11-15 October 2021. virtual conference
- Aljboor, S., Angyal, A., Papp, E., Furu, E., Török, Zs., Szikszai, Z., Kertész, Zs.: COVID-crisis induced changes in the atmospheric particulate matter pollution in Debrecen, Magyar Aeroszol Konferencia, September 21-23, 2022, Hévíz.
- Shafa Aljboor, Máté Szarka, Anikó Angyal, Dávid Baranyai, István Vajda, Zita Szikszai, István Rajta and Zsófia Kertész: The new in-air millibeam-PIXE setup at the ATOMKI Tandetron accelerator RADIATE Summer School 2022, 5-7 October 2022, Firenze, Italy.
- Shafa Aljboor, Anikó Angyal, Enikő Papp, Enikő Furu, Máté Szarka, Zita Szikszai, Zsófia Kertész: Variation of composition and sources of urban atmospheric particulate matter pollution during COVID-19 lockdowns in Debrecen, Hungary, 26th International Conference on Ion Beam Analysis & 18th International Conference on Particle Induced X-ray Emission, 7 – 13. October, 2023, Toyama, Japan.
- Zsófia Kertész, Shafa Aljboor, Máté Szarka, Anikó Angyal, Enikő Papp, Zita Szikszai: The new in-air millibeam PIXE setup at ATOMKI: description, performance and some interesting aspects, 26th International Conference on Ion Beam Analysis & 18th International Conference on Particle Induced X-ray Emission, 7 – 13. October, 2023, Toyama, Japan.

References

1."Ambient (Outdoor) Air Pollution." *World Health Organization*, World Health Organization, 22 Sept. 2021, https://www.who.int/news-room/fact-sheets/detail/ambient-(outdoor)-air-quality-and-health.

2.Manisalidis, I., et al., *Environmental and Health Impacts of Air Pollution: A Review.* Front Public Health, 2020. **8**: p. 14.

3.Kulmala, M., et al., *Formation and growth rates of ultrafine atmospheric particles: a review of observations.* Journal of Aerosol Science, 2004. **35**(2): p. 143-176

4.Sokan-Adeaga, A., et al., *Secondary inorganic aerosols: impacts on the global climate system and human health.* 2019. **3**: p. 249-259.

5.Kittelson, D.B., *Engines and nanoparticles: a review.* Journal of Aerosol Science, 1998. **29**(5): p. 575-588.

6.Mkoma, S.L., *Physico-Chemical Characterisation of Atmospheric Aerosols in Tanzania, with Emphasis on the Carbonaceous Aerosol Components and on Chemical Mass Closure*. 2008.

7.Vallius, M., *Characteristics and sources of fine particulate matter in urban air.* 2005.

8.Jaenicke, R. and C.N. Davies, *The mathematical expression of the size distribution of atmospheric aerosols.* Journal of Aerosol Science, 1976. **7**(3): p. 255-259.

9.Seinfeld, J.H., S.N. Pandis, and K. Noone, *Atmospheric Chemistry and Physics: From Air Pollution to Climate Change.* Physics Today, 1998. **51**(10): p. 88-90.

10.Foltescu, V.L. and A. Zahn, *Aerosols used as tracers for stratosphere-troposphere exchange in the arctic.* Atmospheric Environment, 1995. **29**(15): p. 1777-1784.

11.Aboh, I.J.K. *Characterization and Sources of Air Particulate Matter at Kwabenya, Near Accra, Ghana*. 2000.

12.Sillanpää, M., et al., *Chemical composition and mass closure of particulate matter at six urban sites in Europe.* Atmospheric Environment, 2006. **40**: p. 212-223.

13.Harkel, M.J.T., *The effects of particle-size distribution and chloride depletion of sea-salt aerosols on estimating atmospheric deposition at a coastal site.* Atmospheric Environment, 1997. **31**(3): p. 417-427.

14.Seinfeld, J.H.P.S.N., *Atmospheric chemistry and physics : from air pollution to climate change*. 2016.

15.Raes, F., et al., *Formation and cycling of aerosols in the global troposphere.* Atmospheric Environment, 2000. 34(25): p. 4215-4240.

16.Michael, S., G. de Leeuw, and Y. Balkanski, *Sea-salt aerosol source functions and emissions*. 2004. p. 333-359.

17.Reid, J. and R. Sayer, *Chemistry in the clouds: the role of aerosols in atmospheric chemistry.* Science progress, 2002. 85: p. 263-96.

18.Colbeck, I. and A.-M. Kitto, *Measurement of particulate and gaseous pollutants during photochemical ozone episodes.* Journal of Aerosol Science, 1992. 23: p. 913-916.

19.Michael, S., G. de Leeuw, and Y. Balkanski, *Sea-salt aerosol source functions and emissions*. 2004. p. 333-359.

20.Yao, X., M. Fang, and C.K. Chan, *The size dependence of chloride depletion in fine and coarse sea-salt particles.* Atmospheric Environment, 2003. 37(6): p. 743-751.

21.Xiu, G., et al., *Characterization of major water-soluble inorganic ions in size-fractionated particulate matters in Shanghai campus ambient air.* Atmospheric Environment, 2004. 38(2): p. 227-236.

22.Hu, M., et al., *Seasonal variation of ionic species in fine particles at Qingdao, China.* Atmospheric Environment, 2002. 36(38): p. 5853-5859.

23.Simoneit, B. and M. Mazurek, *Organic Matter of the Troposphere—II.* Atmospheric Environment - ATMOS ENVIRON, 2007. **41**: p. 4-24.

24.Artaxo, P. and H.-C. Hansson, *Size distribution of biogenic aerosol particles from the amazon basin.* Atmospheric Environment, 1995. 29(3): p. 393-402.

25.O'Dowd, C., et al., *Biogenically driven organic contribution to marine aerosol.* Nature, 2004. 431: p. 676-80.
26.Lighty, J.S., J.M. Veranth, and A.F. Sarofim, *Combustion Aerosols: Factors Governing Their Size and Composition and Implications to Human Health.* Journal of the Air & Waste Management Association, 2000. 50(9): p. 1565-1618.
27.Pöschl, U., *Atmospheric Aerosols: Composition, Transformation, Climate and Health Effects.* Angewandte Chemie International Edition, 2005. **44**(46): p. 7520-7540.
28.Khoder, M., *Atmospheric conversion of sulfur dioxide to particulate sulfate and nitrogen dioxide to particulate nitrate and gaseous nitric acid in an urban area.* Chemosphere, 2002. **49**: p. 675-84.
29.Kölling, C. and J. Prietzel, *Correlations between nitrate and sulfate in the soil solution of disturbed forest ecosystems.* Biogeochemistry, 1995. **31**(3): p. 121-138.
30.Yao, X., et al., *Size distributions and formation of ionic species in atmospheric particulate pollutants in Beijing, China: 1—inorganic ions.* Atmospheric Environment, 2003. **37**(21): p. 2991-3000.
31.Langner, J. and H. Rodhe, *A global three-dimensional model of the tropospheric sulfur cycle.* Journal of Atmospheric Chemistry, 1991. **13**(3): p. 225-263.
32.Pakkanen, T.A., *Study of formation of coarse particle nitrate aerosol.* Atmospheric Environment, 1996. **30**(14): p. 2475-2482.
33.Hassan, S., El–Abssawy, and M. Khoder, *Characteristics of gas-phase nitric acid and ammonium-nitrate-sulfate aerosol, and their gas-phase precursors in a suburban area in Cairo, Egypt.* Atmospheric Pollution Research, 2013. **4**: p. 117-129.
34.Savoie, D.L. and J.M. Prospero, *Particle size distribution of nitrate and sulfate in the marine atmosphere.* Geophysical Research Letters, 1982. **9**(10): p. 1207-1210.
35.Seinfeld, J.H. and S.N. Pandis, eds. *Atmospheric chemistry and physics: From air pollution to climate change*. 2nd ed., ed. J.H. Seinfeld and S.N. Pandis. 2006, John Wiley & Sons: Hoboken, NJ.
36.Aneja, V., et al., *Agricultural ammonia emissions and ammonium concentrations associated with aerosols and precipitation in the southeast United States.* J. Geophys. Res, 2003. **108**.
37.Yeatman, S.G., L.J. Spokes, and T.D. Jickells, *Comparisons of coarse-mode aerosol nitrate and ammonium at two polluted coastal sites.* Atmospheric Environment, 2001. **35**: p. 1321-1335.
38.Blando, J.D. and B.J. Turpin, *Secondary organic aerosol formation in cloud and fog droplets: a literature evaluation of plausibility.* Atmospheric Environment, 2000. **34**(10): p. 1623-1632
39.Tuncer, S., et al., *Trace element and magnesium levels and superoxide dismutase activity in rheumatoid arthritis.* Biological Trace Element Research, 1999. **68**(2): p. 137-142.
40.Allen, A.G., et al., *Size Distributions of Trace Metals in Atmospheric Aerosols in the United Kingdom.* Atmospheric Environment, 2001. **35**: p. 4581-4591.
41.Pacyna, J.M. and E.G. Pacyna, *An assessment of global and regional emissions of trace metals to the atmosphere from anthropogenic sources worldwide.* Environmental Reviews, 2001. **9**(4): p. 269-298.
42.Prinn, R., et al., *Evidence for variability of atmospheric hydroxyl radicals over the past quarter century.* Geophysical Research Letters - GEOPHYS RES LETT, 2005. **32**.
43.Balasubramanian, R. and W.B. Qian, *Characterization and source identification of airborne trace metals in Singapore.* J Environ Monit, 2004. **6**(10): p. 813-8.
44.Nriagu, J.O., *A global assessment of natural sources of atmospheric trace metals.* Nature, 1989. **338**(6210): p. 47-49.
45.Pope, C. and D. Dockery, *Health Effects of Fine Particulate Air Pollution: Lines that Connect.* Journal of Air & Waster Management Association, 2005. **56**: p. 709-742.
46.Alexander, L., et al., *Climate change 2013: The physical science basis, in contribution of Working Group I (WGI) to the Fifth Assessment Report (AR5) of the Intergovernmental Panel on Climate Change (IPCC)*. 2013.
47.Simon, V., L. Luchetta, and L. Torres, *Estimating the emission of volatile organic compounds (VOC) from the French forest ecosystem.* Atmospheric Environment, 2001. **35**: p. S115-S126.

48.Namdeo, A. and M.C. Bell, *Characteristics and health implications of fine and coarse particulates at roadside, urban background and rural sites in UK.* Environ Int, 2005. **31**(4): p. 565-73.
49.Stieb, D.M., S. Judek, and R.T. Burnett, *Meta-analysis of time-series studies of air pollution and mortality: effects of gases and particles and the influence of cause of death, age, and season.* J Air Waste Manag Assoc, 2002. **52**(4): p. 470-84.
50.Pope, C.A., 3rd, et al., *Lung cancer, cardiopulmonary mortality, and long-term exposure to fine particulate air pollution.* Jama, 2002. **287**(9): p. 1132-41.
51.Knaapen, A.M., et al., *Inhaled particles and lung cancer. Part A: Mechanisms.* Int J Cancer, 2004. **109**(6): p. 799-809.
52.Salma, I., et al., *Effect of particle mass size distribution on the deposition of aerosols in the human respiratory system.* Journal of Aerosol Science, 2002. **33**: p. 119-132.
53.World Health Organization. Regional Office for, E. and W.H.O.C.T.F.o.t.H.A.o.A.P. Joint, *Health risks of heavy metals from long-range transboundary air pollution*. 2007, Copenhagen: World Health Organization. Regional Office for Europe.
54.Prospero, J., et al., *Prospero JM, Blades E, Mathison G, Naidu R.. Interhemispheric transport of viable fungi and bacteria from Africa to the Caribbean with soil dust. Aerobiologia 21: 1-19.* Aerobiologia, 2005. **21**: p. 1-19.
55.Horwell, C. and P. Baxter, *The respiratory health hazards of volcanic ash: A review for volcanic risk mitigation.* Bulletin of Volcanology, 2006. **69**: p. 1-24.
56.Schwarze, P.E., et al., *Mineral composition other than quartz is a critical determinant of the particle inflammatory potential1 1Following a presentation given as part of the International Congress on Environmental Health and the 4th Annual Meeting of the International Society of Environmental Medicine (ISEM), 1 – 4 October, 2000, Hannover, Germany*. International Journal of Hygiene and Environmental Health, 2002. **204**(5): p. 327-331.
57.Sokhi, R.S., et al., *Advances in air quality research – current and emerging challenges.* Atmos. Chem. Phys., 2022. **22**(7): p. 4615-4703.
58.Haywood, J., et al., *451Global Indirect Radiative Forcing Caused by Aerosols: IPCC (2007) and Beyond*, in *Clouds in the Perturbed Climate System: Their Relationship to Energy Balance, Atmospheric Dynamics, and Precipitation*, J. Heintzenberg and R.J. Charlson, Editors. 2009, The MIT Press. p. 0.
59.Myhre, G., D.T. Shindell, and J. Pongratz. *Anthropogenic and Natural Radiative Forcing*. 2014.
60.Rosenfeld, D., *Suppression of Rain and Snow by Urban and Industrial Air Pollution.* Science (New York, N.Y.), 2000. **287**: p. 1793-6.
61.Arimoto, R., *Eolian dust and climate: Relationship to sources, tropospheric chemistry, transport and deposition.* Ž . Earth-Science Reviews, 2001. **54**: p. 29-42.
62.Ramanathan, V., et al., *Aerosols, Climate, and the Hydrological Cycle.* Science (New York, N.Y.), 2002. **294**: p. 2119-24.
63.Sun, J. and P.A. Ariya, *Atmospheric organic and bio-aerosols as cloud condensation nuclei (CCN): A review.* Atmospheric Environment, 2006. **40**(5): p. 795-820.
64.Ortiz, A. and C. Guerreiro, *Air Quality in Europe - 2020 report*. 2020.
65.Ito, K. and G.D. Thurston, *Daily PM_{10}/mortality associations: an investigations of at-risk subpopulations.* J Expo Anal Environ Epidemiol, 1996. **6**(1): p. 79-95.
66.Thurston, G.D., *A critical review of PM10-mortality time-series studies.* J Expo Anal Environ Epidemiol, 1996. **6**(1): p. 3-21.
67.World Health Organization. Regional Office for Europe. (2000). Air quality guidelines for Europe, 2nd ed. World Health Organization. Regional Office for Europe. https://apps.who.int/iris/handle/10665/107335
68.World Health Organization. Occupational and Environmental Health Team. (2006). WHO Air quality guidelines for particulate matter, ozone, nitrogen dioxide and sulfur dioxide: global update 2005: summary of risk assessment. World Health Organization. https://apps.who.int/iris/handle/10665/69477

69.World Health Organization. (2021). WHO global air quality guidelines: particulate matter (PM2.5 and PM10), ozone, nitrogen dioxide, sulfur dioxide and carbon monoxide. World Health Organization. https://apps.who.int/iris/handle/10665/345329. License: CC BY-NC-SA 3.0 IGO
70.https://www.eea.europa.eu/policy-documents/a-clean-air-programme-for-europe
71.https://www.breeze-technologies.de/blog/european-eu-regulation-and-limits-on-air-pollution/ Pollutants covered by EU National Emission Ceiling legislation and 2030 targets. Source: European Commission.
72.Directive 2008/50/EC of the European Parliament and of the Council of 21 May 2008 on ambient air quality and cleaner air for Europe.
73.National Emissions reduction Commitments (NEC) Directive (2016/2284/EU)
74.https://treaties.un.org/Pages/ViewDetails.aspx?src=IND&mtdsg_no=XXVII-1-h&chapter=27&clang=_en
75.https://www.eea.europa.eu/policy-documents/directive-2010-75-ec-on
76.http://data.europa.eu/eli/dir/2015/2193/oj
77.http://data.europa.eu/eli/dir/2009/125/oj
78.U.S. Congress. (1970) *United States Code: Air Pollution Control, 42 U.S.C. §§ c6-h5 Suppl. 1 1970*. [Periodical] Retrieved from the Library of Congress, https://www.loc.gov/item/uscode1970-016042015b/.
79.U.S. EPA. Air Quality Criteria for Lead (Final Report, 1986). U.S. Environmental Protection Agency, Washington, D.C., EPA/600/8-83/028AF (NTIS PB87142386), 1986.
80.U.S. EPA. Exposure Factors Handbook (1997, Final Report). U.S. Environmental Protection Agency, Washington, DC, EPA/600/P-95/002F a-c, 1997.
81.https://www.epa.gov/sites/default/files/2021-03/documents/20060929_factsheet.pdf (U.S. EPA, 2006).
82.Govil, I.M., *Proton Induced X-ray Emission – A tool for non-destructive trace element analysis.* Current Science, 2001. **80**(12): p. 1542-1549.
83.Massey, H. and N. Feather, *James Chadwick. 20 October 1891 -- 24 July 1974.* Biographical Memoirs of Fellows of the Royal Society, 1976. **22**: p. 11-70.
84.Castaing, R. *Application des sondes electroniques a une méthode d'analyse ponctuelle chimique et cristallographique*. 1952.
85.Khan, J.M., D.L. Potter, and R.D. Worley, *Proposed Method for Microgram Surface Density Measurements by Observation of Proton-Produced X Rays.* Journal of Applied Physics, 1966. **37**(2): p. 564-567.
86.Johansson, S.A.E. and T.B. Johansson, *Analytical application of particle induced X-ray emission.* Nuclear Instruments and Methods, 1976. **137**(3): p. 473-516.
87.https://www.ge.infn.it/geant4/physics/pixe/
88.https://www.jeol.co.jp/en/science/am.html
89.Terzano, R., et al., *Recent advances in analysis of trace elements in environmental samples by X-ray based techniques (IUPAC Technical Report).* Pure and Applied Chemistry, 2019. **91**(6): p. 1029-1063.
90.Kabir, M.H. *Particle induced X-ray emission (PIXE) setup and quantitative elemental analysis*. 2007.
91.Borbely-Kiss, I., et al., *Experimental and theoretical calibration of a PIXE set-up for K and L-x-rays*. 1985: Hungary. p. 30.
92.Ryan, C.G., et al., *Quantitative analysis of PIXE spectra in geoscience applications.* Nuclear Instruments and Methods in Physics Research Section B: Beam Interactions with Materials and Atoms, 1990. **49**(1): p. 271-276.
93.Campbell, J.L. and W.J. Teesdale, *Micro-PIXE analysis of major elements in mineral specimens.* Nuclear Instruments and Methods in Physics Research Section B: Beam Interactions with Materials and Atoms, 1993. **74**(4): p. 503-510.
94.Vekemans, B., et al., *Analysis of X-ray spectra by iterative least squares (AXIL): New developments.* X-Ray Spectrometry, 1994. **23**: p. 278-285.

95.Szabo, G. and I. Borbely-Kiss, *PIXYKLM computer package for PIXE analyses.* Nuclear Instruments and Methods in Physics Research Section B, 1993. **75**(1-4): p. 123-126.
96.Doyle, B.L., D.S. Walsh, and S.R. Lee, *External micro-ion-beam analysis (X-MIBA).* Nuclear Instruments and Methods in Physics Research Section B: Beam Interactions with Materials and Atoms, 1991. **54**(1): p. 244-257.
97.Grime, G.W., *The " Q factor" method: quantitative microPIXE analysis using RBS normalisation.* Nuclear Instruments and Methods in Physics Research Section B: Beam Interactions with Materials and Atoms, 1996. **109-110**: p. 170-174.
98.Grime, G.W., M.H. Abraham, and M.A. Marsh, *The new external beam facility of the Oxford scanning proton microprobe.* Nuclear Instruments and Methods in Physics Research Section B: Beam Interactions with Materials and Atoms, 2001. **181**(1): p. 66-70.
99.Massi, M., et al., *The external beam microprobe facility in Florence: Set-up and performance.* Nuclear Instruments and Methods in Physics Research Section B: Beam Interactions with Materials and Atoms, 2002. **190**(1): p. 276-282.
100.Walter, P., et al., *A new high quality X-ray source for Cultural Heritage.* Comptes Rendus Physique, 2009. **10**(7): p. 676-690.
101.Pásztor, L., et al., *Compilation of a national soil-type map for Hungary by sequential classification methods.* Geoderma, 2017.
102.Major, I., et al., *Source identification of PM2.5 carbonaceous aerosol using combined carbon fraction, radiocarbon and stable carbon isotope analyses in Debrecen, Hungary.* Science of The Total Environment, 2021: p. 146520.
103.Hopke, P.K., et al., *Characterization of the Gent Stacked Filter Unit PM10 Sampler.* Aerosol Science and Technology, 1997. **27**(6): p. 726-735.
104.Putaud, J.-P., et al., *European aerosol phenomenology - 3: physical and chemical characteristics of particulate matter from 60 rural, urban, and kerbside sites across Europe.* Atmos. Environ., 2009: p. 1-13.
105.Manohar, M., et al., *MABI - A multi-wavelength absorption black carbon instrument for the measurement of fine light absorbing carbon particles.* Atmospheric Pollution Research, 2021. **12**(4): p. 133-140.
106.Mousavi, A., et al., *Source apportionment of black carbon (BC) from fossil fuel and biomass burning in metropolitan Milan, Italy.* Atmospheric Environment, 2019. **203**: p. 252-261.
107.Rajta, I., et al., *The new ATOMKI scanning proton microprobe.* Nuclear Instruments and Methods in Physics Research Section B: Beam Interactions with Materials and Atoms, 1996. **109-110**: p. 148-153.
108.Török, Z., et al., *Development of a new in-air micro-PIXE set-up with in-vacuum charge measurements in Atomki.* Nuclear Instruments and Methods in Physics Research Section B: Beam Interactions with Materials and Atoms, 2015. **362**: p. 167-171.
109.Biri, S., et al., *The Atomki Accelerator Centre.* The European Physical Journal Plus, 2021.
110.Campbell, J.L. The GUPIXWIN Manual and User-Guide Fig (vo1.3). University of Guelph, Guelph, Ontario, Canada. (2005)
111.Norris, G., R. Duvall, S. Brown, AND S. Bai. EPA Positive Matrix Factorization (PMF) 5.0 Fundamentals and User Guide. U.S. Environmental Protection Agency, Washington, DC, EPA/600/R-14/108 (NTIS PB2015-105147), 2014. Eddie Lee, Chak K. Chan, Pentti Paatero,
112.Lee, E., C. Chan, and P. Paatero, *Application of Positive Matrix Factorization in Source Apportionment of Particulate Pollutants in Hong Kong.* Atmospheric Environment, 1999. **33**: p. 3201-3212.
113.Paatero, P., et al., *Methods for estimating uncertainty in factor analytic solutions.* Atmos. Meas. Tech., 2014. **7**(3): p. 781-797.
114.Brown, S., et al., *Methods for estimating uncertainty in PMF solutions: Examples with ambient air and water quality data and guidance on reporting PMF results.* The Science of the total environment, 2015. **41**.

115.Paatero, P. and P. Hopke, *Discarding or Downweighting High-Noise Variables in Factor Analytic Models.* Analytica Chimica Acta, 2003. **490**: p. 277-289.
116.Masiol, M., et al., *Hybrid multiple-site mass closure and source apportionment of PM2.5 and aerosol acidity at major cities in the Po Valley.* Science of The Total Environment, 2020. **704**: p. 135287.
117.Dutton, John A. *The ceaseless wind: An introduction to the theory of atmospheric motion*. Courier Corporation, 2002.
118.Carslaw, D. and K. Ropkins, *openair --- An R package for air quality data analysis.* Environmental Modelling & Software, 2012. **27--28**: p. 52-61.
119.Ashbaugh, L.L., W.C. Malm, and W.Z. Sadeh, *A residence time probability analysis of sulfur concentrations at grand canyon national park arizona usa.* Atmospheric Environment, 1985. **19**(8): p. 1263-1270.
120.Hsu, Y.-K., Holsen, T., Hopke, P., 2003. Comparison of hybrid receptor models to locate PCB sources in Chicago. Atmospheric Environment 37, 545e562.
121.Li, D., et al., *Identification of long-range transport pathways and potential sources of PM(2.5) and PM(10) in Beijing from 2014 to 2015.* J Environ Sci (China), 2017. **56**: p. 214-229.
122.Hongye, Z., et al., *Forecasting PM2.5 using hybrid graph convolution-based model considering dynamic wind-field to offer the benefit of spatial interpretability.* Environmental Pollution, 2021. **273**: p. 116473.
123.Santos, O. and L. Hoinaski, *Incorporating gridded concentration data in air pollution back trajectories analysis for source identification.* Atmospheric Research, 2021. **263**: p. 105820.
124.Wang, H., et al., *Seasonal characteristics, formation mechanisms and geographical origins of PM2.5 in two megacities in Sichuan Basin, China.* Atmospheric Chemistry and Physics, 2017. **17**.
125.Liu, Y., et al., *Characterization and source identification of PM(2.5)-bound polycyclic aromatic hydrocarbons (PAHs) in different seasons from Shanghai, China.* Sci Total Environ, 2018. **644**: p. 725-735.
126.Li, H., Q. He, and X. Liu, *Identification of Long-Range Transport Pathways and Potential Source Regions of PM2.5 and PM10 at Akedala Station, Central Asia.* Atmosphere, 2020. **11**: p. 1183.
127.Stein, A., et al., *NOAA's HYSPLIT atmospheric transport and dispersion modeling system.* Bulletin of the American Meteorological Society, 2016. **96**: p. 150504130527006.
128.Rajta, I., et al., *Accelerator characterization of the new ion beam facility at MTA Atomki in Debrecen, Hungary*. Nuclear Instruments and Methods in Physics Research Section A: Accelerators, Spectrometers, Detectors and Associated Equipment, 2018. **880**: p. 125-130.
129.Dias, J.F., A. Bulla, and M.-L. Yoneama, *Charging effects in thick insulating samples.* Nuclear Instruments and Methods in Physics Research B, 2002. **189**: p. 72-76.
130.Ziegler, J.F., M.D. Ziegler, and J.P. Biersack, *SRIM - The stopping and range of ions in matter (2010).* Nuclear Instruments and Methods in Physics Research B, 2010. **268**: p. 1818-1823.
131.Campbell, J.L., et al., *The Guelph PIXE software package IV.* Nuclear Instruments and Methods in Physics Research Section B: Beam Interactions with Materials and Atoms, 2010. **268**(20): p. 3356-3363.
132.Zaluzec, N.J., *Calculating the Detector Solid Angle in X-ray Energy Dispersive Spectroscopy.* Microscopy and Microanalysis, 2009. **15**(S2): p. 520-521.
133.http://www.pt-nsil.com/Public/FinalReports/PTXRFIAEA14.pdf
134.*Instrumentation for PIXE and RBS*. 2000, Vienna: INTERNATIONAL ATOMIC ENERGY AGENCY.
135.Lucarelli, F., et al., *The upgraded external-beam PIXE/PIGE set-up at LABEC for very fast measurements on aerosol samples.* Nuclear Instruments and Methods in Physics Research Section B: Beam Interactions with Materials and Atoms, 2014. **318**: p. 55–59.
136.Li, X.F., et al., *Charge integration in external PIXE–PIGE for the analysis of aerosol samples.* Nuclear Instruments and Methods in Physics Research Section B: Beam Interactions with Materials and Atoms, 2012. **289**: p. 1-4.

137.Adlington, L., *The Corning Archaeological Reference Glasses: New Values for "Old" Compositions.* Papers from the Institute of Archaeology, 2017. **27**.
138.Signorelli, C., et al., *High seroprevalence of SARS_COV-2 in Bergamo: evidence for herd immunity or reason to be cautious?* Int J Public Health, 2020. **65**(9): p. 1815-1817.
139.Bao, R. and A. Zhang, *Does lockdown reduce air pollution? Evidence from 44 cities in northern China.* Sci Total Environ, 2020. **731**: p. 139052.
140.Menut, L., et al., *Impact of lockdown measures to combat Covid-19 on air quality over western Europe.* Science of The Total Environment, 2020. **741**: p. 140426.
141.Berman, J.D. and K. Ebisu, *Changes in U.S. air pollution during the COVID-19 pandemic.* Sci Total Environ, 2020. **739**: p. 139864.
142.Nakada, L.Y.K. and R.C. Urban, *COVID-19 pandemic: Impacts on the air quality during the partial lockdown in São Paulo state, Brazil.* Sci Total Environ, 2020. **730**: p. 139087.
143.Varga-Balogh, A., A. Leelossy, and R. Mészáros, *Effects of COVID-Induced Mobility Restrictions and Weather Conditions on Air Quality in Hungary.* Atmosphere, 2021. **12**: p. 561.
144.Salma, I., W. Thén, and T. Weidinger, *What can we learn about urban air quality with regard to the first outbreak of the COVID-19 pandemic? A case study from central Europe.* ATMOSPHERIC CHEMISTRY AND PHYSICS, 2020. **20**: p. 15725–15742.
145.Clemente María, Á., et al., *Changes in the concentration and composition of urban aerosols during the COVID-19 lockdown.* Environmental Research, 2021. **203**: p. 111788.
146.Gamelas, C., et al., *Source apportionment of PM2.5 before and after COVID-19 lockdown in an urban-industrial area of the Lisbon metropolitan area, Portugal.* Urban climate, 2023. **49**: p. 101446.
147.Giardi, F., et al., *PM 10 variation, composition, and source analysis in Tuscany (Italy) following the COVID-19 lockdown restrictions.* Atmospheric Chemistry and Physics, 2022. **22**: p. 9987-10005.
148.Jeong, C.-H., M. Yousif, and G. Evans, *Impact of the COVID-19 lockdown on the chemical composition and sources of urban PM2.5.* Environmental Pollution, 2021. **292**: p. 118417.
149.Manchanda, C., et al., *Variation in chemical composition and sources of PM(2.5) during the COVID-19 lockdown in Delhi.* Environ Int, 2021. **153**: p. 106541.
150.Ivanovski, M., et al., *Improvement of Air Quality during the COVID-19 Lockdowns in the Republic of Slovenia and its Connection with Meteorology.* Aerosol and Air Quality Research, 2022. **22**: p. 210262.
151.Rys, A., et al., *Comparison of concentrations of chemical species and emission sources PM2.5 before pandemic and during pandemic in Krakow, Poland.* Scientific Reports, 2022. **12**.
152.Massimi, L., et al., *Effects of COVID-19 lockdown on PM10 composition and sources in the Rome Area (Italy) by elements' chemical fractionation-based source apportionment.* Atmospheric Research, 2022. **266**: p. 105970.
153.Hale, T. and N. Angrist, *A global panel database of pandemic policies (Oxford COVID-19 Government Response Tracker).* 2021. **5**(4): p. 529-538.
154.Edouard Mathieu, Hannah Ritchie, Lucas Rodés-Guirao, Cameron Appel, Charlie Giattino, Joe Hasell, Bobbie Macdonald, Saloni Dattani, Diana Beltekian, Esteban Ortiz-Ospina and Max Roser (2020) - "Coronavirus Pandemic (COVID-19)". Published online at OurWorldInData.org. Retrieved from: 'https://ourworldindata.org/coronavirus' [Online Resource].
155.Borkowski, P., M. Jażdżewska-Gutta, and A. Szmelter-Jarosz, *Lockdowned: Everyday mobility changes in response to COVID-19.* Journal of Transport Geography, 2021. **90**: p. 102906.
156.Bucsky, P., *Modal share changes due to COVID-19: The case of Budapest.* Transportation Research Interdisciplinary Perspectives, 2020. **8**: p. 100141.
157.https://www.google.com/covid19/mobility.
158.https://www.met.hu/omsz/tevekenysegek/adattar/
159.https://cds.climate.copernicus.eu/cdsapp#!/home

160. Hersbach, H., et al., *The ERA5 global reanalysis.* Quarterly Journal of the Royal Meteorological Society, 2020. **146**(730): p. 1999-2049.
161. Kalogridis, C., et al., *Assessment of wood burning versus fossil fuel contribution to wintertime black carbon and carbon monoxide concentrations in Athens, Greece.* Atmospheric Chemistry and Physics, 2018. **18**: p. 10219-10236.
162. https://environment.ec.europa.eu/topics/air/air-quality/eu-air-quality-standards_en.
163. Angyal, A., et al., *Source identification of fine and coarse aerosol during smog episodes in Debrecen, Hungary.* Air Quality, Atmosphere & Health, 2021. **14**.
164. Furu, E., et al., *Characterization of Aerosol Pollution in Two Hungarian Cities in Winter 2009–2010.* Atmosphere, 2022. **13**: p. 554.
165. Kertész, Z., et al., *Identification and characterization of fine and coarse particulate matter sources in a middle-European urban environment.* Nuclear Instruments and Methods in Physics Research Section B: Beam Interactions with Materials and Atoms, 2010. **268**: p. 1924-1928.
166. Cohen, D., et al., *Ion beam techniques for source fingerprinting fine particle air pollution in major Asian-Pacific cities.* Nuclear Instruments and Methods in Physics Research Section B: Beam Interactions with Materials and Atoms, 2019. **477**.
167. Almeida, S.M., et al., *Ambient particulate matter source apportionment using receptor modelling in European and Central Asia urban areas.* Environmental Pollution, 2020. **266**: p. 115199.
168. Angyal, A., et al., *Study of Cl-containing urban aerosol particles by ion beam analytical methods.* Nuclear Instruments & Methods in Physics Research Section B-beam Interactions With Materials and Atoms - NUCL INSTRUM METH PHYS RES B, 2010. **268**: p. 2211-2215.
169. Rajesh, T.A. and S. Ramachandran, *Characteristics and source apportionment of black carbon aerosols over an urban site.* Environmental Science and Pollution Research, 2017. **24**(9): p. 8411-8424.
170. Salma, I., et al., *Fossil fuel combustion, biomass burning and biogenic sources of fine carbonaceous aerosol in the Carpathian Basin.* Atmospheric Chemistry and Physics, 2020. **20**: p. 4295-4312.
171. Urban, R.C., et al., *Use of levoglucosan, potassium, and water-soluble organic carbon to characterize the origins of biomass-burning aerosols.* Atmospheric Environment, 2012. **61**: p. 562–569.
172. Hudda, N., et al., *Reductions in traffic-related black carbon and ultrafine particle number concentrations in an urban neighborhood during the COVID-19 pandemic.* Sci Total Environ, 2020. **742**: p. 140931.
173. Kar, S., et al., *Metallic components of traffic-induced urban aerosol, their spatial variation, and source apportionment.* Environmental Monitoring and Assessment, 2010. **168**: p. 561-574.
174. Chow, J. and J. Watson, *Review of PM2.5 and PM10 Apportionment for Fossil Fuel Combustion and Other Sources by the Chemical Mass Balance Receptor Model.* Energy & Fuels, 2002. **16**: p. 222-260.
175. Bondietti, E.A. and C. Papastefanou, *Estimates of residence times of sulfate aerosols in ambient air.* Science of The Total Environment, 1993. **136**(1): p. 25-31.